Dissertation zur Erlangung des Doktorgrades
der Fakultät für Chemie und Pharmazie
der Ludwig-Maximilians-Universität München

The potential to identify and explore innovative anticancer targets by using the natural products Vioprolide A and Lagunamide A

Christina Orgler

geb. Besl

aus Eggenfelden, Deutschland

2019

Erklärung

Diese Dissertation wurde im Sinne von §7 der Promotionsordnung vom

28. November 2011 von Frau Prof. Dr. Angelika M. Vollmar betreut.

Eidesstattliche Versicherung

Diese Dissertation wurde eigenständig und ohne unerlaubte Hilfe erarbeitet.

München, den 08.11.2019

Christina Orgler (geb. Besl)

Dissertation eingereicht am:	05.09.2019
1. Gutachterin:	Prof. Dr. Angelika M. Vollmar
2. Gutachterin:	Prof. Dr. Olivia Merkel
Mündliche Prüfung am:	24.10.2019

Meinen Eltern

Contents

Abstract

Natural products display a rich source of bioactive molecules and have traditionally contributed to the identification and investigation of potential targets for drug development. Especially in devastating diseases such as cancer novel targets are urgently needed in order to exploit disease related pathways and to develop respective targeted therapies. Inspired by the promising anticancer activities of the myxobacterial compound Vioprolide A (VioA) and the marine cyanobacterial product Lagunamide A (LagA), we performed in depth studies on their modes of action.

The Vioprolides represent a unique class of natural products with potent bioactivity towards cancer cells in the nanomolar range. By applying thermal proteome profiling (TPP) in cooperation with the group of Prof. Dr. Stephan Sieber (TU Munich, Germany), we could identify the nucleolar protein 14 (NOP14), as direct interaction partner of VioA, the most potent growth inhibitory Vioprolide derivative. NOP14 is involved in ribosome biogenesis and plays a key role in the assembly of the ribosomal subunit. In fact, VioA represents the first small molecule addressing this crucial pathway. Peripheral blood mononuclear cells (PBMCs) of healthy donors showed a low response to VioA in contrast to acute lymphoblastic leukemia (ALL) cells, highlighting VioA as promising lead structure for cancer cell targeting. Furthermore, closer mechanistic studies revealed that VioA impairs the interaction between NOP14 and the essential ribosome assembly factor ribosomal RNA small subunit methyltransferase Nep1 (EMG1). Concluding, our results indicate that targeting ribosome biosynthesis is a promising anticancer strategy and underscores the great potential of VioA as chemical tool to study ribosome assembly processes as well as starting point for future drug development.

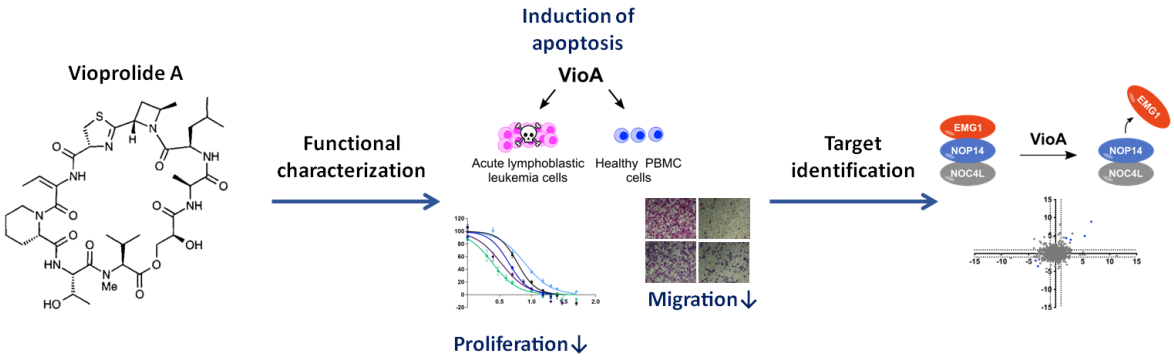

Fig. 1 The Vioprolide A project at a glance.

Besides the ribosome biogenesis machinery, mitochondria have emerged as potential anticancer targets in recent years, as cancer cell mitochondria are structurally and functionally different from their non-cancerous counterparts. Detailed functional characterization of the marine natural compound LagA suggests a mitochondria-perturbing mode of action, comprising changes in mitochondrial dynamics and resulting in mitochondrial apoptotic cell death. These findings emphasize the need to elucidate the molecular targets addressed by this interesting molecule, which is not known yet. LagA represents a promising new compound with potentially important applications as both anticancer drug lead structure and molecular probe to explore cancer-related mitochondrial pathways.

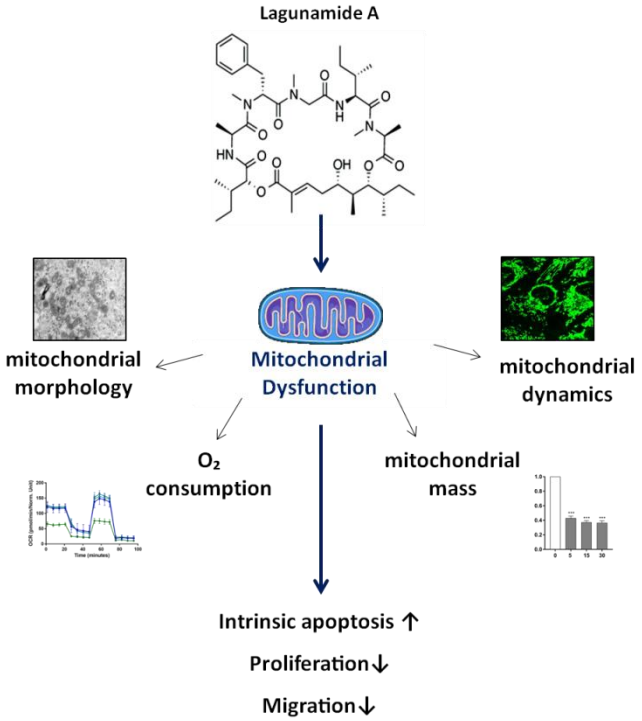

Fig. 2 The Lagunamide A project at a glance.

1. Introduction

1.1 Natural compounds- a source for innovation in cancer research

1.1.1 Natural products - model molecules for the discovery of new drug targets

Naturally occurring compounds display an exceptional diversity of bioactive molecules with interesting biological activities, making them an essential source of both drug leads and cell biology tools. Their importance is further illustrated by the fact that approximately 50% of all FDA approved anticancer drugs since the 1940s are natural products or derivatives of them (*1*). But, particularly cancer therapy still suffers from a restricted spectrum of molecular targets that can be addressed by small molecules, albeit the introduction of targeted chemotherapy significantly improved treatment results and revolutionized cancer therapy in the recent decades (*2*). However, drug resistance, therapeutic failure or relapse are still widespread and require identification and validation of novel and innovative drug targets optimized for specific cancer relevant proteins and pathways. In this context, natural products are particularly valuable as research tools, because they are often coevolved with protein targets and, therefore, are prone to exhibit high selectivity for a wide variety of biological targets for specific purposes (*3*). Identification of the molecular targets of newly discovered natural compounds has had insightful effects on studies of complex cellular machineries, demonstrating the role of specific targets and pathways. Consequently, despite the technical hitches implicated in isolating and synthesizing natural products, successful identification of their targets stimulates research in basic cell biology and biomedicine (*4*).

1.1.2 Myxobacteria and marine cyanobacteria- prolific sources for lead structures

One example of a fruitful source for new natural compounds with high chemical diversity, biochemical specifity and unusual modes of actions are myxobacteria (*5*). The gram-negative myxobacteria are unicellular rod shaped bacteria that occur in soil, dung of herbivorous animals or decaying plant material (*6*). They are characterized by an unusual way of life, as they move by gliding on surfaces and have the ability to form ‘social’ multicellular fruiting bodies when nutrients become limited (*7*). Myxobacteria have one of the largest bacterial genomes and one more remarkable characteristic is that they are amongst the top producers of a wide range of secondary metabolites with unique structural properties (*5, 8*). Interestingly, these products often have unusual target structures, which are rarely or not targeted by other metabolites, making them excellent

tools for the identification of novel targets and cellular pathways (*9*). In 2007, Ixabepilone, an analogue of the myxobacterial molecule Epothilone B, was FDA approved for the treatment of metastatic breast cancer (*10*), signifying that myxobacterial compounds also display a considerable resource for the development of new lead structures in drug discovery processes.

Besides natural compounds from terrestrial plants or microbes that have long been the traditional source of lead structures, the isolation of marine natural products from various organisms led to great success in anticancer drug discovery in recent years (*11, 12*). Their significance is highlighted by the fact that four marine organism-derived compounds are currently in clinical use for the treatment of cancer: cytarabine (Cytosar®), Trabectidin (Yondelis®), Eribulin (Halaven®) and the conjugated antibody Brentuximab vedotin (Adcetris®) (*11*). The small molecule part of Brentuximab vedotin, monomethyl auristatin E is designed based on the marine cyanobacterial molecule Dolastatin 10 (*13*). Amongst other marine microbes, cyanobacteria represent an exceptionally rich source of structurally diverse molecules with promising pharmacological activities. The prokaryotic cyanobacteria, also known as blue-green algae, exist as unicellular species or in colonies and are able to obtain energy through photosynthesis (*14*). As cyanobacteria are an ancient group of organisms, they produce compounds that are optimized by evolution over billions of years to efficiently target relevant pathways, highlighting the perception that marine cyanobacteria-derived molecules hold great promise in developing biochemical study tools and agents for cancer (*15*).

1.1.3 Vioprolides

From the myxobacterial strain *Cystobacter violaceus*, Schummer et al. reported the isolation of the four novel metabolites Vioprolide A-D (*16*). The cyclic structure of this natural compound family is composed of eight amino acids and one glyceric acid (Figure 1). In this initial publication from 1996, the vioprolides were described to exert striking antifungal and anticancer activities, encouraging further biological analyses of this interesting class of compounds. Recently, Vioprolide A has been described to be a potent activator of IL-1ß maturation and to induce intrinsic apoptosis in primary murine macrophages (*17*). Moreover, detailed studies on the biosynthesis of vioprolides have been performed lately (*18, 19*). But, despite their promising biological activity, no molecular target and mode of action elucidation was reported up to date.

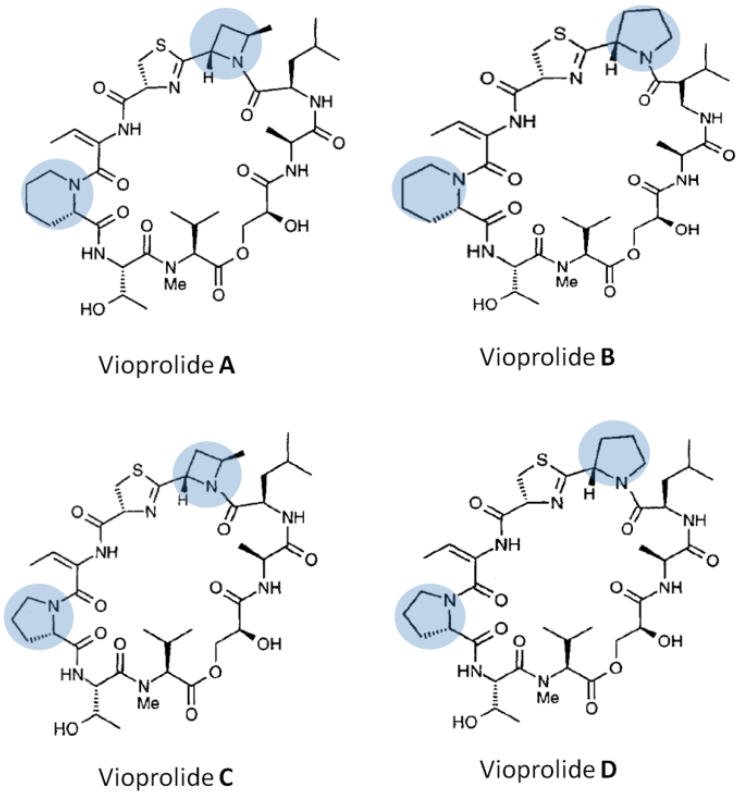

Fig.3 Chemical structures of Vioprolides A-D. Structural differences in N-heterocycles are highlighted.

1.1.4 Lagunamides

Lagunamide A and its analogues Lagunamides B and C are potent cyclic depsipeptides obtained from the marine cyanobacterium, *Lyngbya majuscula*. These molecules are structurally related to a series of other cytotoxic marine cyanobacterial compounds like the Aurilides or Kulokekahilide-2, which are already known to exhibit striking anticancer effects (*20*). Previous studies also described potent growth inhibitory activities in the low nanomolar range against a panel of cancer cell lines (*21*). Furthermore, first biochemical studies of Lagunamide A revealed that the cytotoxic effect of the natural compound is triggered via mitochondria-mediated apoptosis (*22*). Still, in depth studies concerning the mechanism of action upstream intrinsic apoptosis induction are not available.

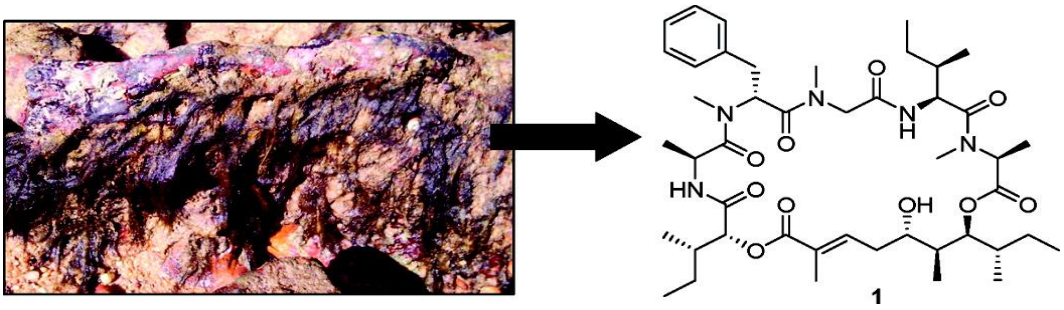

Fig. 4 Chemical structure of Lagunamide A. Lagunamide A was first isolated from the marine cyanobacterium *Lyngbya majuscula* obtained from Pulau Hantu Besar, Singapore. Figure adapted from Tripathi *et al. (21),* permission to reuse figure was obtained.

1.2 The nucleolus- an emerging target for cancer therapy

1.2.1 The nucleolus as the main site for ribosome biogenesis

The nucleolus is a dynamic, sub-nuclear and membrane-less organelle, first described in the 1830s by the German physiologists Rudolph Wagner and Gabriel Valentin (*23, 24*). In the early 1960s the discovery was made that the nucleolus is the site of ribosomal RNA (rRNA) synthesis and nascent ribosome assembly (*25*). It is now apparent that arrangement of nucleoli depends on ongoing transcription of ribosomal DNA (rDNA), where 18S, 28S, and 5.8S rRNAs are encoded. Perturbations that lead to inhibition of rRNA synthesis rapidly result in disassembly of nucleoli (*26*). Consistently, the nucleolus disassembles during the onset of mitosis, when rDNA transcription is halted and reassembles during the early G1 phase (*27*). Genes that encode for rRNA are arranged in the nucleoli as arrays of head-to-tail tandem repeats, termed nucleolar organizer regions (NOR). In detail, the 47S rRNA precursor that is transcribed by RNA polymerase I (Pol I) in the nucleolus, is further processed in order to generate the mature 18S, 5.8S and 28S

rRNA. The 5S rRNA transcribed by RNA polymerase III (Pol III) in the nucleoplasm, is imported to the nucleolus (*28*). The mature rRNAs represent the nucleic acid backbone of the ribosome and finally assemble with the numerous ribosomal proteins, whose mRNA is transcribed by RNA polymerase II (Pol II) to form the small pre-40S and the large pre-60S ribosomal subunits. Subsequently the mature ribosomal subunits interact with the export machinery and migrate to the cytoplasm, where they finally make up the mature 80S ribosome particle (*26*). In summary, ribosome biogenesis is one of the most complex and energy consuming processes of a cell that needs the coordinated activity of all three RNA polymerases and many transiently associated ribosome assembly factors. Biogenesis of ribosomes is furthermore tightly regulated and linked to other fundamental cellular processes, like cell growth and division (*29*).

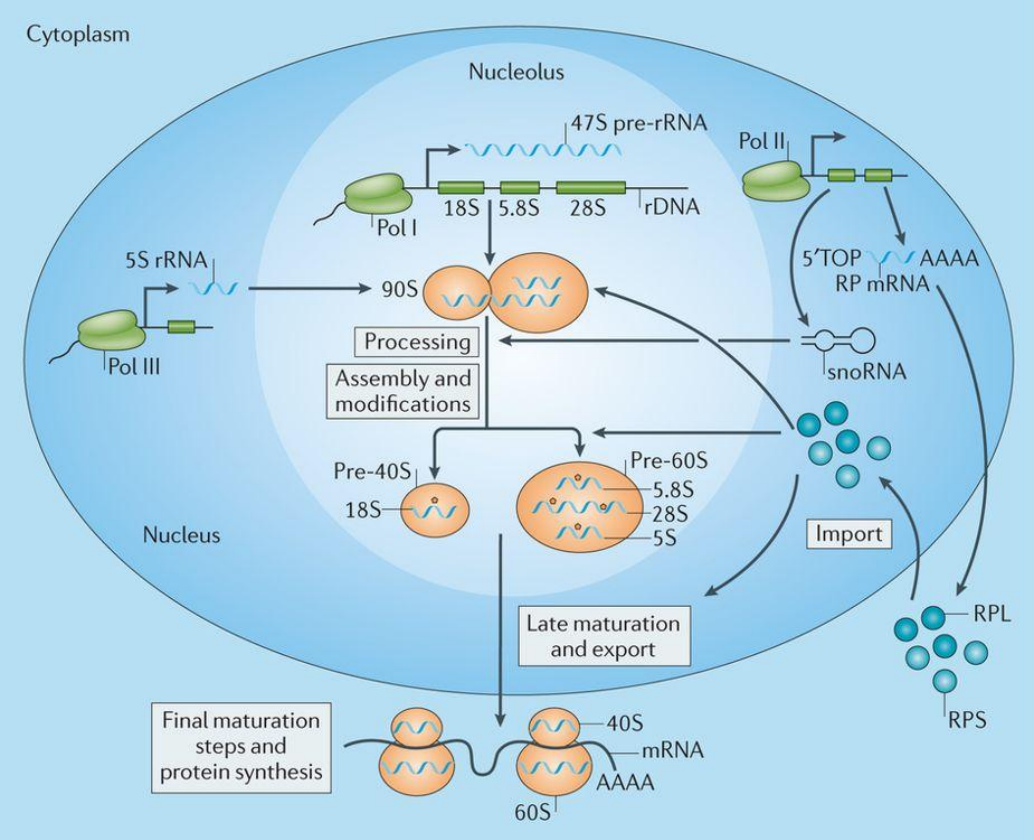

Fig. 5 Overview of ribosome biogenesis. Ribosome biogenesis mainly takes place in the nucleoli, where RNA polymerase I (Pol I) transcribes 47S pre-rRNAs from ribosomal DNA (rDNA) genes. The 47S precursor rRNA is further processed to 18S, 5.8S and 28S rRNAs. Together with the 5S rRNA transcribed by RNA polymerase III (Pol III) and ribosomal proteins (RPs) the rRNAs are assembled to the 90S processome. During the maturation of the 90S processome into pre-40S and pre-60S ribosomal subunits, pre-rRNA is modified and processed through mechanisms that involve small nucleolar RNAs (snoRNAs). The 40S subunit contains 18S ribosomal RNA (rRNA) and 33 RPs, the 60S subunit contains 5S, 5.8S and 28S rRNAs and 47 RPs. The subunits get transported to the cytoplasm, where they finally assemble to mature 80S ribosomes. Adapted from Pelletier *et al. (30),* permission to reuse figure was obtained.

1.2.2 Ribosome biogenesis in cancer

Cancer cells exhibit a number of abnormal properties in order to maintain their uncontrolled growth and proliferation. In this context ribosome biogenesis and protein synthesis are essential cellular processes necessary for persistent cancer cell growth (*31*). The transient nucleolus thereby plays a fundamental role in the up-regulated synthesis of rRNA to maintain ribosome biogenesis, which is considered a hallmark of cancer. Obviously, cell growth depends on protein production and is therefore coupled to the synthesis of rRNA by Pol I and Pol III. Thus, an activated Pol-I-specific oncogenic transcription factor can be enough to accelerate proliferation (*32*). Hypertrophy of the nucleolus, which can be visualized by analysis of silver- stained nucleolar organizer regions (AgNOR) is one of the most characteristic cytological features of cancer cells and the earliest link between the nucleolus and malignant transformation (*26, 33*). In detail, it is the dense concentration of macromolecules at the sites of rRNA synthesis that is responsible for the strong visibility of nucleoli that withdraw if transcription is deficient. Conversely, nucleoli expand when Pol I transcription is elevated. The inflated nucleoli of cancer cells are therefore an obvious indication that rRNA synthesis is unusually high (*32*). Ribosome biogenesis is carefully controlled by multiple cell signaling pathways that converge on the Pol I complex. Because rRNA synthesis is the rate-limiting step of ribosome biogenesis, many Pol I regulators play critical roles in cancer (*34*). Oncogenic signaling, for example activation of MYC or ERK signalling pathways can up-regulate Pol I to accelerate ribosome biogenesis, whereas tumor suppressor proteins like p53 can inhibit rRNA synthesis (*32, 35*).

Concluding, there is an obvious contribution of the nucleolus to malignant transformation, highlighting its potential as a target for cancer therapy and the necessity to develop respective targeted therapies.

1.2.3 The nucleolus as a drug target

The great potential of targeting the nucleolus and thereby ribosome biogenesis in cancer is gaining more and more interest, not least because many drugs currently used for cancer therapy have been shown to exert their cytotoxic activity at least in part by inhibition of rRNA synthesis (*36*). More precisely, drugs that either damage DNA or hinder DNA synthesis, like Cisplatin, Oxaliplatin, Doxorubicin or Mitoxantrone inhibit ribosome biogenesis at the level of Pol I transcription, resulting in nucleolar disruption (*26*). Moreover, drugs like 5-Fluorouracil and the translation inhibitor Homoharringtonine impair late rRNA processing (*37*). However, none of these examples is selective enough for Pol I

transcriptional inhibition to allow precise conclusions how ribosome biogenesis inhibition contributes to therapeutic success. Conversely, a new generation of drugs that selectively inhibit Pol I transcription is currently in development (*35*). A major advantage thereby is that Pol I specific inhibitors, in contrast to DNA damaging agents, only hinder ribosome biogenesis without being genotoxic (*36*). The first agent targeting Pol I transcription is CX-3543, which binds G-quadruplex DNA structures in rDNA repeats and prevents nucleolin/ G-quadruplex complex formation (*38*). In that way, it acts quite similar to Actinomycin D, which intercalates into GC- rich duplex DNA that is common in rDNA repeats (*37*). The small molecule CX-5461 presents the next generation of Pol I inhibitors that impair transcription by disrupting the binding of the transcription initiation factor SL-1 to the rDNA promoter. With a remarkable selectivity towards Pol I that is 300-400 fold higher than to Pol II or Pol III, CX-5461 has shown to be effective in a wide range of human cancer cell lines at low nanomolar concentrations and currently in phase I/ II clinical trials (*39, 40*).

Summarizing, the introduction of these novel specific rRNA synthesis inhibitors may stimulate more studies aiming to identify compounds that selectively target the nucleolus and the ribosome biogenesis machinery in cancer cells.

1.3 Mitochondria as anticancer drug target

1.3.1 Mitochondrial processes in cancer

Mitochondria are double membrane-enclosed organelles that have been integrated into modern eukaryotes via symbiosis of a proteobacterium 1.5-2 billion years ago (*41*). Due to their versatile roles in ATP production, generation of reactive oxygen species (ROS) and regulation of apoptosis; mitochondria are involved in various pathological processes, like neurodegenerative diseases, aging, diabetes and cancer. Furthermore these multifaceted functions of mitochondria make them important cellular stress sensors in normal physiology. But on the other hand mitochondria also provide flexibility for tumor cell growth and survival in harsh conditions, such as starvation, hypoxia and anti-cancer treatments, signifying that mitochondria are key players in tumorigenesis (*42*). Non-malignant cells mainly rely on oxidative phosphorylation for ATP production, whereas cancer cells exhibit enhanced glycolysis, despite the presence of oxygen (*43*). This phenomenon is known as the Warburg effect. Importantly, ATP production by aerobic glycolysis, which directly results in increased generation of lactate, is advantageous to cancer cells because it allows them to better survive under conditions of varying oxygen levels (*44*).

1.3.2 The mitochondrial cell death machinery

In addition to their essential role in energy metabolism, mitochondria are the central mediators of intrinsic apoptosis. Thereby, the pro-apoptotic Bcl-2 family members BAX and BAK are recruited to the outer mitochondrial membrane (OMM) and oligomerize to mediate mitochondrial outer membrane permeabilization (MOMP), resulting in cytochrome C release from the mitochondrial intermembrane space. Released to the cytosol, cytochrome C activates downstream caspases to execute programmed cell death. Under normal physiological conditions, anti-apoptotic family members such as Bcl-2 and Bcl-xL bind and inhibit BAX/BAK. A hallmark of cancer is resistance to apoptosis by downregulating pro-apoptotic and upregulating anti-apoptotic proteins, which is also contributing to chemoresistance (*45*). Besides the permeabilization of mitochondria that is mediated by Bcl-2 family members, mitochondrial apoptosis is also accompanied by morphological changes, the so called cristae remodeling. These ultrastructural changes are required to enable the complete release of cytochrome C from the cristae space to the intermembrane space, where it can be released across the outer mitochondrial membrane (*46*). A key player in mitochondrial cristae remodeling is the dynamin-like GTPase optic atrophy 1 (OPA1) that functions as glue holding the cristae together (*47*). Ongoing apoptosis leads to reduction of mitochondrial membrane potential, activating the protease OMA1, which in turn can cleave OPA1. Cleavage of OPA1 results

in disassembly of cristae junctions and allows complete release of cytochrome C. Remarkably, enforced expression or oligomerization of OPA1 can delay apoptosis, substantiating that cristae remodeling plays a crucial role in the control of cell death (*48*). Taken together, the mitochondrial apoptotic machinery provides multiple target structures that can be potentially used for chemotherapeutic intervention.

1.3.3 Mitochondrial dynamics in cancer

There are more aspects of mitochondrial biology beyond bioenergetics and regulation of cell death that support malignant transformation and therefore provide a basis for anticancer therapy: the mitochondrial fission and fusion dynamics. Mitochondria are extremely dynamic organelles that either exist as fused tubular networks or fragmented granules (*49*). This balance of fission and fusion is regulated by multiple parameters like mitochondrial metabolism, respiration, oxidative stress or cellular state (*50*). Altered mitochondrial dynamics is a key feature of cancer. Multiple studies revealed an imbalance of fission and fusion in cancer with elevated fission activity and/ or decreased fusion resulting in a fragmented mitochondrial phenotype (*51*). This observation is particularly striking in KRAS dependent tumours, where oncogenic KRAS signaling stimulates mitochondrial division via ERK-mediated phosphorylation of DRP1- a key player in mitochondrial membrane fission (*52*). Importantly, restoration of mitochondrial fusion by DRP1 inhibition or overexpression of the mitochondrial fusion regulator Mfn-2 impaired cancer cell growth, signifying that mitochondrial network remodeling plays a crucial role in tumorigenesis (*51, 52*). However, the oncogenic transcription factor c-MYC also influences mitochondrial dynamics mainly resulting in mitochondrial fusion (*53*). These findings demonstrate that there are diverging effects of oncogenic signaling on mitochondrial dynamics and further investigations are needed to understand these correlations in the context of cancer.

1.4 Aim of the study

With Lagunamide A from marine cyanobacteria and the myxobacterial Vioprolide A we have two interesting natural products in hands that already have been shown to exert striking activity against cancer cells. First biological data leave no doubt that both natural products are promising candidates for new anticancer drug leads. However, detailed characterization of the respective modes of action of these potent molecules is still missing. For that reason, we aimed to explore the anticancer properties of Vioprolide A and Lagunamide A in depth and to elucidate their mechanisms of action in order to reveal their potential as future anticancer drug leads as well as molecular probes.

Part I: Vioprolide A

Direct target and mode of action elucidation

1. Functional characterization in tumor cells concerning proliferation, migration and apoptosis
2. Target identification via thermal protein profiling (TPP) performed by Volker Kirsch (Group of Prof. Sieber, TU Munich)
3. Target verification and revelation of its role in cancer cells
4. Mechanistic studies on drug - target interactions

Part II: Lagunamide A

Mode of action studies with focus on mitochondrial pathways

1. Functional characterization in tumor cells concerning proliferation, migration and apoptosis
2. Analysis of mitochondrial dynamics and morphology
3. Studies on mitochondrial function (oxygen consumption, ATP production)

2. Materials and Methods

2.1 Materials

2.1.1 Cells

2.1.1.1 Cell lines

Table 1 List of cell lines

Cell line	Supplier
BxPC3	ATCC, Manassas, VA, USA
CCRF-CEM	M. Kavallaris, Sydney, Australia
Hela	DSMZ, Braunschweig, Germany
HL-60	ATCC, Manassas, VA, USA
S-Jurkat	P.H. Krammer, Heidelberg, Germany
Jurkat *neo*	P.H. Krammer, Heidelberg, Germany
Jurkat *Bcl-2*	P.H. Krammer, Heidelberg, Germany
Jurkat *Bcl-xL*	P.H. Krammer, Heidelberg, Germany
Jurkat *CASP8 -/-*	P.H. Krammer, Heidelberg, Germany
Panc 03.27	ATCC, Manassas, VA, USA
Panc 10.05	ATCC, Manassas, VA, USA
T24	DSMZ, Braunschweig, Germany

2.1.1.2 Patient derived xenograft cells

Patient derived xenograft (PDX) cells were kindly provided by the group of Prof. Dr. Irmela Jeremias (Helmholtz Center, Munich, Germany) after isolation from the bone marrow or spleen of NOD.Cg-*Prkdc*^{scid} *Il2rg*^{tm1Wjl}/SzJ (NSG) mice. PDX cells were cultured in RPMI 1640 containing 20% FCS, 1mM pyruvate and P/S. The technique of growing patient leukemia cells in mice has been described previously (*54, 55*). Patients' clinical characteristics are summarized in Table 2. Written informed consent was obtained from all patients. The study was performed in accordance with the ethical standards of the responsible committee on human experimentation (written approval by the Research Ethics Boards of the medical faculty of Ludwig-Maximilians-University, Munich, numbers 068-08 and 222-10) and with the Helsinki Declaration of 1975, as revised in 2000.

Table 2 Clinical characteristics of patient derived xenograft (PDX) cells. ALL: Acute lymphoblastic leukemia.

Sample	Disease stage	Age	Sex	Subtype	Karyotype
ALL-50	initial diagnosis	7	female	pre-B	t(1;19)
ALL-199	relapse 2	8	female	pre-B	somatic trisomy 21
ALL-707	initial diagnosis	2	male	pro-B	t(4;11)

2.1.1.3 Peripheral blood mononuclear cells

Peripheral blood mononuclear cells (PBMC) were isolated from blood of healthy donors by gradient centrifugation. Isolation was performed by Fabian Koczian in the laboratory of Prof. Dr. Angelika Vollmar as described previously (*56*).

2.1.2 Compounds

Vioprolides A-D were kindly provided by Prof. Dr. Rolf Müller (Helmholtz Centre for Infection Research, Saarbrücken, Germany). Lagunamide A was kindly provided by Prof. Dr. Uli Kazmaier (Institute for Organic Chemistry, Saarland University, Saarbrücken, Germany). The study compounds were dissolved in sterile DMSO for cell culture and aliquoted for long-term storage at -20°C.

Actinomycin D (ActD) was dissolved in DMSO and purchased from Sigma Aldrich (St Louis, MO, USA).

2.1.3 Antibodies

Table 3 List of primary antibodies

Primary Antibody	Source	Supplier
Actin	Mouse	Millipore, Darmstadt, Germany
Bcl-2	Rabbit	Cell Signaling, Danvers, MA, USA
Bcl-xL	Rabbit	Cell Signaling, Danvers, MA, USA
BrdU	Mouse	Sigma Aldrich, St. Louis, MO, USA
Caspase-3	Rabbit	Santa Cruz, Dallas, TX, USA
Caspase-8	Mouse	Cell Signaling, Danvers, MA, USA
Cytochrome c	Rabbit	Cell Signaling, Danvers, MA, USA
DRP1	Rabbit	Cell Signaling, Danvers, MA, USA
Phospho-DRP1 (Ser616)	Rabbit	Cell Signaling, Danvers, MA, USA
Phospho-DRP1 (Ser637)	Rabbit	Cell Signaling, Danvers, MA, USA
EMG1	Mouse	Sigma Aldrich, St. Louis, MO, USA
Mcl-1	Rabbit	Cell Signaling, Danvers, MA, USA
NOP14	Rabbit	Sigma Aldrich, St. Louis, MO, USA

NOC4L	Rabbit	Sigma Aldrich, St. Louis, MO, USA
PARP	Rabbit	Cell Signaling, Danvers, MA, USA
PGC1α	Rabbit	Abcam, Cambridge, UK
PHB1	Rabbit	Cell Signaling, Danvers, MA, USA

Table 4 List of secondary antibodies

Secondary antibody	Source	Supplier
Anti-rabbit IgG, HRP	Goat	Dianova, Hamburg, Germany
Anti-mouse IgG1, HRP	Goat	Abcam, Cambridge, UK
Alexa Fluor 488, anti-mouse IgG (H+L)	Goat	Thermo Fisher, Waltham, MA, USA
Alexa Fluor 488, anti-rabbit IgG (H+L)	Goat	Thermo Fisher, Waltham, MA, USA
Alexa Fluor 647, anti-rabbit IgG (H+L)	Chicken	Thermo Fisher, Waltham, MA, USA

2.1.4 Small interfering RNA

For gene silencing, ON-TARGETplus SMARTpool small interfering RNA (siRNA) reagent from GE Dharmacon (Lafayette, CO, USA) against human NOP14 was used. ON-TARGETplus non-targeting control siRNA served as control for RNA interference experiments. SiRNAs were resuspended in 1x siRNA buffer (diluted from Dharmacon 5x siRNA buffer in RNAse-free water) according to Dharmacon siRNA resuspension protocol to a final concentration of 20µM, aliquoted and stored at -20°C.

2.1.5 Chemicals and reagents

Table 5 List of biochemicals, kits, dyes and cell culture reagents

Reagent	Supplier
5x siRNA buffer	Dharmacon, Lafayette, CO, USA
2,2,2-Trichloroethanol (TCE)	Sigma Aldrich, St. Louis, MO, USA
µMACS™ Protein G Micro Beads	Miltenyi Biotech, Bergisch Gladbach, Germany
Active Ras Detection Kit	Cell Signaling, Danvers, MA, USA
Ammonium persulfate (APS)	Sigma Aldrich, St. Louis, MO, USA
Bovine serum albumin (BSA)	Sigma Aldrich, St. Louis, MO, USA
Bradford reagent Roti®Quant	Bio-Rad, Munich, Germany
Cell-Titer Blue® (CTB)	Promega, Madison, WI, USA
Collagen G	Biochrom AG, Berlin, Germany
Complete®	Roche Diagnostics, Basel, Switzerland
Coumaric acid	Fluka, Buchs, Switzerland

CyQuant® Cell Proliferation Assay Kit	Life Technologies, Eugene, USA
Dharmafect 1 Reagent	Dharmacon, Lafayette, CO, USA
DMEM cell culture medium	PAN Biotech, Aidenbach, Germany
Dimethylsulfoxide (DMSO)	AppliChem, Darmstadt, Germany
Fetal calf serum (FCS)	PAN Biotech, Aidenbach, Germany
FluorSave® Reagent	Merck, Darmstadt, Germany
FuGene HD	Promega, Madison, WI, USA
Glutaraldehyde 2,5% in 0.1M Sodium Cacodylate Buffer, pH 7.4	EMS Science Services, Hatfield, PA, USA
Glycerol	Applichem, Darmstadt, Germany
High-Capacity cDNA Reverse Transcription Kit	Applied Biosystems, Foster City, CA, USA
Hoechst 33342	Sigma Aldrich, St. Louis, MO, USA
Human recombinant insulin	Sigma Aldrich, St. Louis, MO, USA
IMDM	Thermo Fisher, Waltham, MA, USA
JC-1	Enzo, Farmingdale, NY, USA
Luminol	AppliChem, Darmstadt, Germany
Matrigel™	Corning Incorporated, New York, NY, USA
MicroAmp® Fast Optical 96-Well Reaction Plate	Applied Biosystems, Waltham, USA
MitoTracker Green FM	Molecular Probes, Darmstadt, Germany
MitoTracker Deep Red FM	Molecular Probes, Darmstadt, Germany
$Na_2EDTA \times 2H_2O$	Sigma Aldrich, St. Louis, MO, USA
Na_3VO_4	ICN Biomedicals, Aurora, OH, USA
Nonfat powdered milk (Blotto)	Carl Roth, Karlsruhe, Germany
Page-Ruler™ Prestained Protein Ladder	Thermo Fisher, Waltham, MA, USA
Penicillin/Streptomycin	PAN Biotech, Aidenbach, Germany
PMSF	Sigma Aldrich, St. Louis, MO, USA
Rotiphorese Gel 30	Carl Roth, Karlsruhe, Germany
PowerUp™ SYBR® Green Master Mix	Applied Biosystems, Waltham, MA, USA
Propidium iodide	Sigma Aldrich, St. Louis, MO, USA
Pyronin Y	Sigma Aldrich, St. Louis, MO, USA
Pyruvate	Merck, Darmstadt, Germany
Qiagen RNeasy Mini Kit	Qiagen, Hilden, Germany
RPMI 1640 cell culture medium	PAN Biotech, Aidenbach, Germany
Seahorse XF Base Medium	Agilent Technologies, Santa Clara, CA, USA
Seahorse XF MitoStress Test Kit	Agilent Technologies, Santa Clara, CA, USA
Seahorse XFe96 FluxPaks	Agilent Technologies, Santa Clara, CA, USA
Sodium dodecyl sulfate (SDS)	AppliChem, Darmstadt, Germany
TEMED	VWR, Radnor, PA, USA

Tris Base	Sigma Aldrich, St. Louis, MO, USA
Triton X-100	Merck, Darmstadt, Germany
Trypsin	PAN Biotech, Aidenbach, Germany
Tween 20	VWR, Radnor, PA, USA

All commonly used acids, bases, buffer salts and organic solvents were either purchased from Merck (Darmstadt, Germany) or Sigma Aldrich (St Louis, MO, USA).

2.1.6 Technical equipment

Table 6 Technical equipment

Device	Producer
µMACS™ separator	Miltenyi Biotech, Bergisch Gladbach, Germany
µColumns	Miltenyi Biotech, Bergisch Gladbach, Germany
Axiovert 25/200 microscope	Zeiss, Oberkochen, Germany
BEEM® capsule G360.1	Plano GmbH, Wetzlar, Germany
Bold Line incubation system	Okolab, Pozzuoli, Italy
ChemiDoc Touch Imaging System	Bio-Rad, Hercules, CA, USA
Cell culture flasks, tubes and plates	VWR, Bruchsal, Germany
CIM plate 16	ACEA Biosciences, San Diego, CA, USA
E plate 16	ACEA Biosciences, San Diego, CA, USA
EOS 450C camera	Canon, Tokyo, Japan
FACS Canto II	BD, Franklin Lakes, NJ, USA
HeraCell incubator	Heraeus, Hanau, Germany
ibiTreat µ-slide 8-well	ibidi GmbH, Munich, Germany
Leica DMi1 microscope	Leica Microsystems, Wetzlar, Germany
Leica-SP8 confocal microscope	Leica Microsystems, Wetzlar, Germany
Mini PROTEAN 3 chamber	Bio-Rad, Hercules, CA, USA
NanoDrop® ND-100 Spectrophotometer	Peqlab Biotechnology, Erlangen, Germany
Nitrocellulose membrane	Amersham Bioscience, Freiburg, Germany
Olympus Ck30 microscope	Olympus, Tokyo, Japan
Pipettes (5ml, 10ml, 25ml)	Greiner Bio, Frickenhausen, Germany
Pipette tips (10µl, 100µl, 1000µl)	Sarstedt, Numbrecht, Germany
PowerPac HC, Tank Blotting System	Bio-Rad, Hercules, CA, USA
PVDF (0.2µm, 0.45µm) membrane	Amersham Bioscience, Freiburg, Germany
SpectraFluor Plus™	Tecan, Männedorf, Switzerland
Tecan Sunrise	Tecan, Männedorf, Switzerland
Transwell Permeable Supports 8 µm pore polycarbonate inserts	Corning Incorporated, New York, NY, USA
Vi-Cell™ XR	Beckman Coulter, Krefeld, Germany

xCELLigence system	Roche Diagnostics, Mannheim, Germany

2.1.7 Software

Software	Supplier
FlowJo 7.6.5	Tree Star, Ashland, OR, USA
GraphPad Prism 7	GraphPad Software, San Diego, CA, USA
ImageJ	NIH, Bethesda, MD, USA
Image Lab 5.2	Bio-Rad, Hercules, CA, USA
Leica LAS X	Leica, Wetzlar, Germany
Microsoft Office 2010	Microsoft, Redmont, WA, USA
RTCA software 2.0	ACEA Biosciences, San Diego, CA, USA
Wave 2.3.0	Agilent Technologies, Santa Clara, CA, USA

2.2 Cell Culture

For the cultivation of CCRF-CEM cells and BxPC3 cells RPMI 1640 supplemented with 10% fetal calf serum (FCS) and a combination of 100 U/ml penicillin and 100µg/ml streptomycin (P/S) was used, while all Jurkat cell lines were cultivated in the same medium with additional 1mM pyruvate. HL-60 cells were maintained in IMDM medium supplemented with 20% FCS and P/S. Panc 03.27 and Panc 10.05 cells were cultivated in RPMI 1640 supplemented with 15% FCS and 10 Units/ ml human recombinant insulin and P/S. HeLa and T24 cells were maintained in DMEM supplemented with 10% FCS and P/S. All cells were cultured at 37°C with 5% CO_2 at constant humidity in an incubator.

2.2.1 Passaging

Suspension cells lines were maintained at a cell density between 0.1-1.0 x 10^6 cells/ml and typically passaged three times per week. Adherent cells were cultured as monolayer in 75cm² culture flasks until they reached 80-90% confluence. For detachment of cells, they were washed twice with pre-warmed PBS and subsequently incubated with trypsin/ EDTA (Table 6) for 2-3 min at 37°C. The enzymatic reaction was stopped by adding complete growth medium. The cell density was determined using the ViCell XR cell viability analyzer prior to seeding in multiwell-plates or dishes for further experiments or culture flaks for further cultivation.

Table 7 Solutions and reagents for cell culture

PBS (pH 7.4)	
NaCl	132.2mM
Na_2HPO_4	10.4mM
KH_2PO_4	3.2mM
H_2O	

Trypsin/EDTA	
Trypsin	0.05% /w/v)
Na_2EDTA	0.02% (w/v)
PBS	

2.2.2 Freezing and thawing of cells

For freezing, the cell density was adjusted to 2 x 10^6 cells/ ml in growth medium supplemented with 20% FCS, Pen/ Strep and 10% DMSO. Aliquots of 1.5 ml in cryo vials were prepared and immediately frozen at -20°C for 1-2 hours, transferred to -80°C overnight and finally stored in liquid nitrogen. For recultivation, cells were thawed in a water bath at 37°C, transferred into a tube containing 20 ml of growth medium and centrifuged. The supernatant was discarded and cells were resuspended in 5ml of fresh growth medium and seeded into a 25 cm^2 flask for further expansion.

2.2.3 Stimulation with compounds

Adherent cell lines were seeded the day before treatment to ensure complete attachment. Suspension cells were treated after 4h incubation. DMSO stock solutions of test compounds were thawed and pre-diluted in complete growth medium. DMSO concentration did not exceed 0.1% (v/v) in all experiments.

2.2.4 Transfection with siRNA

For gene silencing, cells were transfected according to the DharmaFECT™ Transfection Reagents- siRNA transfection protocol. Cells were seeded in antibiotic free medium at a density of 0.15 x 10^6 cells / ml the day before transfection. For one 6-well, 10µl siRNA (c=5µM] was diluted in 190µl serum-free medium and 4µl DharmaFECT I reagent was diluted in 196µl serum-free medium and incubated for 5 min at RT. The content of the two tubes was gently mixed by carefully pipetting up and down, incubated for 20 min at RT and subsequently transferred to the culture plate.

2.3 Proliferation assay

2.3.1 Crystal violet assay

To determine the proliferative capacity of adherent cells, respective cell types were seeded into 96-well plates (2500 cells/ well) and treated with the indicated test compounds on the subsequent day for 72h. Afterwards the media was discarded, cells were washed with PBS and then stained and fixed with crystal violet solution (Table 8) for

10 min. Stained cells were washed with distilled water and dried, before crystal violet was re-dissolved in sodium citrate solution for 10 min. Absorbance was measured at 540 nm using the Tecan Sunrise microplate reader. As a reference for the cell number at day 0, three wells were seeded on a separate plate and crystal violet staining was performed at the time point of treatment (day 0 Ctrl.). Day 0 Ctrl value was subtracted from the measured values and proliferation [%] was determined relative to DMSO control.

Table 8 Solutions for crystal violet assay

Crystal violet solution	
Crystal violet	0.5% (w/ v)
Methanol	20% (v/ v)
H_2O	

Sodium citrate solution	
Sodium citrate	0.1 M
Ethanol	50% (v/ v)
H_2O	

2.3.2 Cell titer blue (CTB) assay

To analyze the proliferation rate of suspension cells, respective cell lines were seeded at a density of 5000 cells/ well in a 96-well plate. Subsequently, cells were stimulated with the indicated test compounds for 72h. Next, cell titer blue (CTB) reagent was added to each well (volume ratio 2:5) and incubated for 4h at 37°C. Viable cells are able to reduce the dye resazurin into the highly fluorescent resofurin, which fluorescence was recorded at 595 nm using the Tecan SpectraFluor Plus microplate reader. As a reference for the cell number at day 0, three wells were seeded on a separate plate and CTB was added at the time point of stimulation (day 0 Ctrl.). The day 0 Ctrl. value was subtracted from the measured values and viable cells [%] were determined relative to DMSO control.

2.3.3 xCELLigence proliferation assay

For real-time monitoring of proliferation, adherent cells were seeded at a density of 5000 cells/ well in equilibrated E-plates 16 an allowed to adhere for 24h. Next, cells were challenged with cytotoxic agents as indicated and their response was continuously monitored for the subsequent 72h at 37°C using the RTCA xCELLigence device. Through impedance measurement, the xCELLigence system evaluates the cell index, a dimensionless parameter that is proportional to the cell number. The cell index was normalized at the time-point of treatment and The RTCA software was used for further data analysis.

2.4 Migration and invasion assays

2.4.1 Transwell migration assay

Migration of cells was evaluated by using the Boyden chamber technique, where cells are placed inside a transwell and allowed to migrate through restricted pores towards a chemoattractant. In detail, T24 cells were detached and counted and 7 x 10^4 cells in 100µl medium without FCS were stimulated with the test compound and seeded into the top of a Boyden chamber insert with 8µm pore size. The lower compartment was filled with medium containing 10% FCS, which served as chemoattractant. T24 cells were allowed to migrate through the pores for 16h. Subsequently, migrated cells were fixed and stained with crystal violet solution as described in 2.3.1 and cells that remained in the upper compartment were carefully removed with a q-tip. Cells that reached the bottom of the insert were imaged using an Axiovert 25 microscope and an EOS 450C camera. For each condition 4 images were taken and cells were counted using ImageJ software. Number of migrated cells was normalized towards DMSO control.

2.4.2 xCELLigence migration assay

For real time monitoring of cell migration, a CIM plate 16 was assembled and equilibrated according to manufacturer's protocol. Normal growth medium containing 10% FCS was added to the lower chambers of the plate and served as a chemoattractant. Cells were detached, counted and the cell number was adjusted to 40.000 cells/ 100µl medium without FCS per well. Subsequently, cells were transferred into the upper chamber of the plate and allowed to settle onto the bottom for 30 min at RT. Afterwards, the CIM plate was placed into the xCELLigence instrument and migration was recorded at 37°C for at least 16h. By impedance measurement, the xCELLigence device evaluates the cell index, a dimensionless parameter that is proportional to the number of migrated cells. Further data evaluation was performed with the RTCA xCELLigence software.

2.4.3 Three-dimensional spheroid invasion assay

To evaluate the ability of tumour cells to invade surrounding tissues, a spheroid-based invasion assay as described by Vinci et al. was performed (*57*). T24 cells were detached and counted before dilution of the cell suspension for obtaining a concentration of 1 x 10^4 cells/ ml. Next, the cell suspension was dispensed into an ultra-low attachment (ULA) 96-well round bottom plate (200µl/ well). Spheroids were allowed to grow for 72h at 37°C. Subsequently the ULA 96-well plate was placed on ice and 100µl growth medium was removed from each well. Matrigel™, thawed on ice and mixed with 2x the final concentration of test substance or vehicle, was added to each well (100µl/ well). After centrifugation (300xg, 4°C, 3 min) to ensure that spheroids are centrally located in each

well, the Matrigel™ was allowed to polymerize at 37°C for 1h. Afterwards 100µl/ well complete growth medium was added containing the test substance or vehicle. Spheroid invasion was monitored after 24, 48 and 72h with a Leica DMi1 microscope and spheroid size was calculated with ImageJ.

2.5 Flow cytometry

2.5.1 Apoptosis and cell cycle analysis

Apoptosis rate was determined by propidium iodide (PI) staining and flow cytometry as described by Nicoletti et al. (*58, 59*) Cells were seeded into 24-well plates at a density of 100.000 cells/ well and treated with test compounds as indicated the day after seeding for 24 or 48h. Subsequently, cells were detached (if applicable), washed with ice cold PBS and permeabilized and stained by adding fluorochrome solution (Table 9). After 30 min incubation at 4°C in the dark, cells were analysed by flow cytometry on a BD FACSCanto II. Per sample 10.000 events were recorded at Ex488 nm/ Em585 nm. The fluorescence intensity indicates the DNA content. In apoptotic cells, DNA is fragmented, which leads to a relatively low fluorescence (subG1 population). Cell cycle analysis and apoptotic cells were determined with FlowJo software.

Table 9 Fluorochrome solution

Fluorochrome solution	
Propidium iodide	50µg/ ml
Sodium citrate	0.1% (w/ v)
Triton X-100	0.1% (v/ v)
PBS	

2.5.2 Apoptosis of PDX cells and PBMCs

PDX cells and PBMCs were stimulated with test compounds for 24h and subsequently transferred to FACS tubes, washed with PBS and resuspended in 250µl PBS. Next, cells were analyzed on a FACSCanto II and the percentage of viable and apoptotic cells was determined by forward/ side scatter (FSC/ SSC) gating as described previously (*56*). In Figure 6, FSC/ SSC dot plots of DMSO control versus Vioprolide A (VioA) treated ALL-707 PDX cells are exemplarily shown. Specific apoptosis rate was calculated according to the following formula:

$$Specific\ apoptosis\ [\%] = \frac{apoptotic\ cells\ VioA\ [\%] - \ apoptotic\ cells\ DMSO\ [\%]}{100\% - apoptotic\ cells\ DMSO\ [\%]}$$

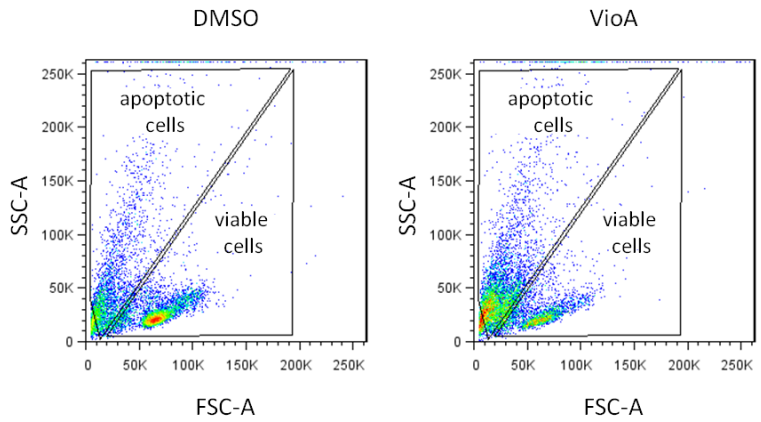

Fig.6 Gating of viable and apoptotic cells in PDX samples. Representative FSC-SSC dot plots of PDX cells treated with VioA versus DMSO control are shown.

2.5.3 Mitochondrial membrane potential

JC-1 staining was used to determine the mitochondrial membrane potential (ΔΨm). Tetraethylbenzimidazolylcarbocyanine iodide (JC-1) is a cationic dye that accumulates in mitochondria. When mitochondrial membrane potential is high, JC-1 aggregates in mitochondria, yielding a red to orange coloured fluorescence. Upon loss of mitochondrial membrane potential, the dye predominantly exists as a monomer in the cytosol emitting green fluorescence. In detail, treated cells were detached (if applicable) and transferred into FACS tubes. Subsequently cells were stained with 1µg/ ml JC-1 dye and incubated at 37°C for 30 min, washed with PBS and resuspended in PBS. In parallel, compensation samples were prepared using the BD CompBeads Anti-mouse Ig, κ particles set and Alexa Fluor and PE-conjugated antibodies. Prior to analysis of JC-1 stained cells, compensation of spectral overlap was performed at the FACSCanto II. Relative amount of populations exposing red or green fluorescence was determined with FlowJo software. Alexa 488 was plotted against PE fluorescence.

2.5.4 Mitochondrial mass

Mitochondrial mass was determined by MitoTracker Green FM staining and flow cytometry. Cells were seeded into 24 well plates at a density of 100.000 cells/ well and treated with test compounds as indicated the day after seeding. Afterwards cells were detached (if applicable), washed with ice cold PBS and permeabilized and stained by adding 400nM MitoTracker Green FM. After 30 min incubation at 37°C, cells were centrifuged and resuspended in PBS before analysis by flow cytometry on a BD FACSCanto II. Per sample 10.000 events were recorded at Ex 488 nm/ Em 516 nm. Median of intensity was determined with FlowJo software and mitochondrial mass was calculated relative to DMSO control.

2.6 Western blot analysis

2.6.1 Cell lysis

Cellular protein levels were analysed by Western Blot. For lysis of adherent cell types, medium was removed and cells were washed with ice cold PBS before adding lysis buffer (Table 10) and freezing at -80°C overnight. Subsequently, cells were scraped off with a cell scraper and transferred into Eppendorf tubes before centrifugation (14.000 rpm, 10 min, and 4°C) in order to remove debris. Suspension cells were centrifuged, washed with ice cold PBS and resuspended in lysis buffer before freezing at -80°C overnight and centrifugation (14.000 rpm, 10 min, 4°C). After the centrifugation step, the whole cell lysate was stored at -20°C, if not immediately processed further.

Table 10 Buffers for cell lysis

Lysis buffer stock	
EDTA	2mM
NaCl	137mM
Glycerol	10% (v/ v)
$Na_4P_2O_7$ x 10 H_2O	2mM
Tris- Base	20mM
Triton-X 100	1% (v/ v)
$C_3H_7Na_2O_6P$ x 5 H_2O	20mM
NaF	10mM
H_2O	

Lysis buffer final composition	
lysis buffer stock	920µl
Na_3VO_4 100mM	20µl
PMSF 50mM	20µl
Complete® 25x	40µl

2.6.2 Protein quantification and sample preparation

To ensure equal protein loading, protein concentration was determined by Bradford assay. In detail, 5µl of whole cell lysate was diluted in water 1:5 (v/ v) and 10µl of the prepared dilution was transferred to a 96-well plate in triplicates. In parallel, bovine serum albumin (BSA) standards (0-500µg/ ml) were transferred to the 96-well plate. Bradford reagent, diluted 1:5 (v/ v) in water was added to the samples (190µl/ well) and incubated for 5 min at RT. Bradford assay is addition of coomassie brilliant blue G-250 to protein solution. The coomassie blue dye associates with basic and aromatic amino acids, thereby causing a shift in absorbance during protein determination. The resulting absorbance was measured at a Tecan Sunrise microplate reader and protein concentrations of the samples were calculated by linear regression. Subsequently 5x SDS sample buffer (Table 11) was added to the samples and protein concentration was adjusted by adding 1x SDS sample

buffer. Afterwards the samples were heated at 95°C for 5 min and stored at -20°C before gel electrophoresis.

Table 11 Sample buffers for Western Blot

5x SDS sample buffer	
Tris-HCl (pH 6.8)	3.125M
Glycerol	50% (v/ v)
SDS	5% (w/ v)
DTT	2% (w/ v)
Pyronin Y	0.025% (w/ v)
H_2O	

1x SDS sample buffer	
5x SDS sample buffer	20% (v/ v)
H_2O	

2.6.3 SDS PAGE and tankblotting

For separation of proteins, discontinuous SDS- polyacrylamide gel electrophoresis (SDS PAGE) was performed. Equal amounts of protein samples were loaded on polyacrylamide (PAA) gels consisting of a separation and a stacking gel. The PAA concentration used was typically 12%, but was adjusted depending on the molecular weight of the analysed proteins. The Mini Protean 3 system chamber from Bio-Rad was filled with electrophoresis buffer (Epho buffer) and gels were loaded with samples. Electrophoresis was performed at a current of 100 V for 21 min and at 200 V for 45 min for protein stacking and separation, respectively. To determine the molecular weight of the proteins detected, a pre-stained protein ladder PageRuler™ or PageRuler Plus™ was subjected to gel electrophoresis in parallel.

Table 12 Buffers and gel mixtures for gel electrophoresis

Stacking Gel	
Rotiphorese Gel 30	17% (v/ v)
Tris-HCl (pH 6.8)	125 mM
SDS	0.1% (w/ v)
TEMED	0.2% (v/ v)
APS	0.1% (w/ v)
H_2O	

Separation Gel 12%	
Rotiphorese Gel 30	40% (v/ v)
Tris-HCl (pH 8.8)	375 mM
SDS	0.1% (w/ v)
TEMED	0.1% (v/ v)
APS	0.05% (w/ v)
TCE	0.5% (w/ v)
H_2O	

Epho buffer	
Tris	4.9mM
Glycine	38mM
SDS	0.1% (w/ v)
H_2O	

Prior to tank blotting, protein load was determined by stainfree detection of trichloroethanol (TCE) supplemented gels using the ChemiDoc Touch Imaging System. Subsequently, proteins were transferred onto a PVDF membrane by tank blotting. PVDF membranes were activated in methanol for 1 min before a blotting sandwich (fiber pad-blotting paper – separation gel – PVDF membrane – blotting paper – fiber pad) was prepared and put into the Mini Trans-Blot® system that was subsequently filled with 1x tank buffer (Table 13). The proteins were transferred at 4°C utilizing a constant current of 100V for 90 min.

Table 13 Buffers for tank blotting

5x tank buffer	
Tris base	240 mM
Glycine	195 mM
H_2O	

1x tank buffer	
5x tank buffer	20% (v/ v)
Methanol	20% (v/ v)
H_2O	

2.6.4 Protein detection

Membranes were blocked with a 5% (w/ v) solution of milk powder in TBS-T buffer for 2h at RT to avoid unspecific binding of primary antibodies. Subsequently, membranes were incubated with primary antibody solution at 4°C under gentle agitation overnight. Primary antibodies were usually diluted 1:000 (v/ v) in 1% (w/ v) milk powder solution in TBS-T. On the next day, membranes were washed three times with TBS-T and incubated with an appropriate HRP-linked secondary antibody for 2h at RT. After additional three washing steps with TBS-T, enhanced chemiluminescence (ECL) imaging was used to detect antibody signals on membranes. In detail, proteins were detected by HRP-linked oxidation of luminol and chemiluminescence detection by incubating membranes for 1 min in ECL solution and developing membranes directly on the ChemiDoc Touch imaging system from Bio-Rad. Further data evaluation was performed with Image Lab software.

2.7 Co- immunoprecipitation

2.7.1 MS based co-immunoprecipitation

VioA target interactome analysis was performed by Volker Kirsch in the laboratory of Prof. Dr. Stephan Sieber (TU Munich, Germany) using MS-based co-immunoprecipitation of the target protein NOP14.

For MS-based co-Immunoprecipitation experiments $4x10^6$ cells were plated out on 6 cm dishes (Sarstedt) in 8 mL media supplemented with VioA (10 nM, 10 µM stock solution in DMSO, 0.1% final concentration of DMSO) or DMSO respectively. After incubation (37°C, 5% CO_2, 24 h) 37°C, 5% CO_2, cells were counted and readjusted to a number of $4x10^6$ cells per dish. Cells were subsequently, pelleted (800 x g, 6 min, RT), supernatant discarded, and cells washed in PBS twice. For *in situ* cellular cross-linking cells were resuspended in PBS and supplemented with 2mM DSSO crosslinker. After incubation (37°C, 5% CO_2, 1 h) cells were pelleted (600 g, 5 min, 4°C), supernatant discarded, and remaining DSSO crosslinker quenched by resuspending cells in cold tris buffer (1 mL, 50 mM Tris-HCl, pH = 8.0). Cells were pelleted (600 g, 5 min, 4°C), resuspended in cold PBS, pelleted and supernatant discarded. For cell lysis, cells were taken up in IP lysis buffer (500 µL, 50 mM Tris-HCl, 150 mM NaCl, 1 mM $MgCl_2$, 5% (v/v) glycerol, 1% (v/v) NP-40, pH = 7.4) and incubated for 30 min on ice. Cell lysate was cleared from debris (21,000 g, 20 min, 4°C), protein concentrations determined using Bradford assay and samples normalized to a total protein amount of 500 µg per sample (protein concentration 1 µg/ µL). 30 µL Protein A/G Agarose beads were equilibrated with cold IP wash buffer (1 mL, 50 mM Tris-HCl, pH = 7.4, 150 mM NaCl, 1 mM $MgCl_2$, 5% (v/v) glycerol, 0.05% NP-40), centrifuged (1,000 g, 1 min, 4°C), supernatant discarded and 500 µL of sample

added directly to the beads. Additionally, 10 µl of NOP14 antibody (Cat. No. HPA039596, Sigma Aldrich) was added. For determination of unspecific background binding to the beads and antibody constant regions, 0.4 µl isotype control rabbit mAb IgG (Cat. No. 2729, Cell Signaling) was added to control samples, and all samples incubated at 4°C under constant rotation overnight. Subsequently, samples were centrifuged (1,000 g, 1 min, 4°C) and supernatant discarded. For removal of unspecific bound proteins, pelleted beads were resuspended in IP wash buffer, centrifuged (500 g, 30 sec, 4°C), and supernatant discarded. The procedure was carried out twice, and twice again with IP basic buffer (50 mM Tris-HCl, pH = 7.4, 150 mM NaCl, 5% (v/v) glycerol) for detergent removal. Samples were reduced and digested by the addition of IP elution buffer I (25 µL, 50 mM Tris-HCl, pH = 8.0; 5 ng/µL Trypsin (500 ng/µL stock solution, sequencing grade, modified, Promega), 2 M Urea, 1 mM DTT (500 mM stock solution in H_2O). Samples were incubated (30 min, 600 rpm, rt) prior to addition of IP elution buffer II (100 µL; 50 mM Tris-HCl; pH = 8.0; 2 M Urea; 5 mM IAA (500 mM stock solution in H_2O), followed by incubation at 37°C and 600 rpm overnight. Tryptic digest was stopped by the addition of FA (1% final concentration). Samples were desalted using C18-stage tips (double layer; Empore disk-C18; 47 mm; Agilent Technologies) using the following procedure: Equilibration with MeOH (70 µL), followed by washing with 0.5% FA (3x 70 µL), sample load and a washing step (3x 70 µL, 0.5% FA). Finally, peptides were eluted with elution buffer (3x 30 µL; 80% MeCN, 0.5% FA). Samples were dried using a centrifugal vacuum concentrator (Eppendorf). Prior to LC-MS/MS analysis dried peptide samples were reconstituted in 1% FA in ddH_2O (26 µL), sonicated for 10 min and filtered using 0.22 µm Ultrafree-MC® centrifugal filters (Merck, UFC30GVNB), pre-equilibrated with 300 µL 1% FA in ddH_2O and transferred into LC-MS vials. The experiment was carried out in quadruplicates.

2.7.2 Western blot based co-immunoprecipitation

For investigation of protein- protein interactions co-immunoprecipitation (co-IP) experiments were performed. Jurkat cells were seeded at a density of 1 x 10^5 cells/ ml and treated as indicated. Subsequently, cells were pelleted, washed with ice-cold PBS and cell lysis was performed by incubating cells with Triton-X 100 lysis buffer (Table 14) for 30 min on ice. After removal of cell debris by centrifugation (10.000 rpm, 10 min., 4°C) protein concentration was determined by Bradford assay as described in 2.6.2. Next 500µg protein per sample was adjusted to 500µl final volume with Triton-X 100 lysis buffer and mixed with 10µl NOP14 antibody (Cat. No. HPA039596, Sigma Aldrich) and 50µl µMACS Protein G magnetic beads and was incubated under gentle agitation at 4°C for 4h. In parallel 500µg protein, mixed with 5µl normal rabbit IgG1 control antibody (Cat. No.

2729, Cell Signaling) and 50µl magnetic beads was prepared as negative control. For co-IP the magnetic labelled NOP14 and its interacting proteins were retained on Miltenyi µColumns. In detail, µColumns were placed into the µMACS separator magnetic field and equilibrated with Triton-X 100 buffer before loading with the samples. After four washing steps with Triton-X 100 buffer the columns were finally rinsed with low salt wash buffer (Table 14). Proteins were eluted with 1x SDS sample buffer pre-heated to 95°C and subjected to Western Blot as described in 2.6.3 and 2.6.4.

Table 14 Buffers for Co-IP

Triton-X 100 buffer (pH 8.0)	
NaCl	150mM
Tris HCl	50mM
Triton-X 100	1% (v/ v)
Complete 25x	4% (v/ v)
H_2O	

Low salt wash buffer (pH 7.5)	
Tris HCl	20mM
H_2O	

2.8 Confocal microscopy

2.8.1 Immunostaining

For immunostaining cells were seeded in ibidiTreat 8- well slides and allowed to adhere overnight. Cells were stimulated and subsequently washed with PBS and fixed with 4% paraformaldehyde (PFA) in PBS for 10 min. After permeabilization with 0.1% Triton X-100 in PBS at RT for 15 min, cells were washed with PBS and incubated with 1% BSA in PBS for 2h under gentle agitation. Subsequently, primary antibody, diluted 1:400 (v/ v) in 1% BSA in PBS was added and cells were incubated overnight at 4°C. On the next day, cells were washed three times with PBS+ 0.2% TX-100 and the appropriate Alexa 488 or Alexa 647 secondary antibody; diluted 1:500 in PBS was added for 2h at RT in the dark. For nuclei staining, Hoechst 33342 was added (final c= 5µg/ ml) for 30 min and cells were finally washed three times for 10min with PBS. One drop of FluorSave reagent mounting medium was added to each well before sealing with a cover slip. After 30 min incubation at RT, Confocal microscopy was performed on a Leica SP8 LSM system and images were analyzed with Leica LAS X or ImageJ software.

2.8.2 Nuclear run on assay

Cells were seeded as described in 2.8.1 and treated with the indicated substances and 5mM 5-Fluorouracil (5-FU) was added for the last 60 min. Fixation and permeabilization was performed as described in 2.8.1. Subsequently cells were stained with anti-BrdU antibody as primary antibody and Alexa Fluor 488 as secondary antibody. Percentages of positive cells were calculated. Treatment with actinomycin D (7.5g/ml) served as positive control for transcriptional inhibition.

2.8.3 Live cell imaging

For imaging of mitochondrial dynamics in living cells a stage top cell chamber was installed on a Leica SP8 microscope to maintain the required culturing conditions (37°C, 5% CO2, 95% humidity). Cells were seeded into an ibidiTreat 8- well slide and allowed to adhere overnight before treatment with the test compound and staining with 400nM MitoTracker Green FM in normal growth medium for 30 min. After incubation, cells were immediately imaged live.

2.9 Transmission electron microscopy

For Transmission electron microscopy (TEM) cells were detached, counted and washed with PBS before 4 x 10^5 cells per sample were transferred to a BEEM® capsule. Cells were pelleted, and supernatant was removed before 600µl 2.5% glutaraldehyde was added to the sample. Embedding and further preparation of the samples was performed by Carola Eberhagen and electron microscopy was performed by Dr. Sabine Schmitt in the laboratory of Prof. Dr. Hans Zischka (Institute of Molecular Toxicology and Pharmacology, Helmholtz Centre, Munich).

2.10 Seahorse mito stress test

HeLa cells were seeded into an XFe 96 microplate at a density of 1.2 x 10^4 cells/ 80µl growth medium/ well and were allowed to adhere for 24h. Subsequently cells were stimulated with test compounds as indicated for 24h. The Seahorse Mito Stress Test was performed by using the provided kit and the Seahorse XFe96 Analyzer according to manufacturer's protocol. An overview of the injected substances and the analyzed parameters is given in Figure 7. The measured oxygen consumption rate (OCR) results were normalized to the cell number, determined by CyQuant® GR dye DNA content measurement. Further data analysis was performed with the Wave 2.3.0 software and the Seahorse XF Mito Stress Test Report Generator, both provided by the manufacturer.

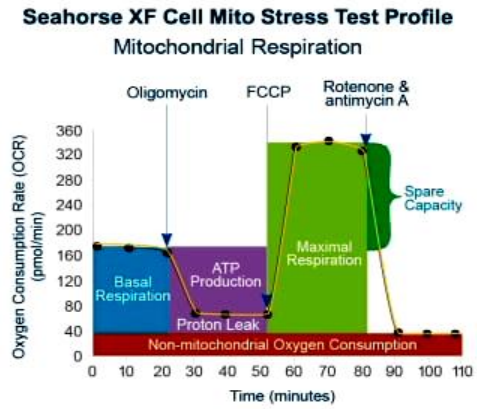

Fig. 7 Agilent Seahorse Mito Stress Test prolife. Sequential addition of different inhibitors and measured parameters are shown.

2.11 Thermal proteome profiling

VioA target identification was performed by Volker Kirsch in the laboratory of Prof. Dr. Stephan Sieber (TU Munich, Germany) using thermal proteome profiling (TPP).

In situ thermal proteome profiling experiments were carried out as reported (*60*) previously with minor modifications. $6x10^7$ Jurkat cells were washed with PBS, resuspended in medium w/o FCS and supplemented with VioA (1µM) or DMSO respectively and transferred into T75-flasks. After incubation (37°C, 5% CO_2, 1 h) cells were pelleted (800 g, 6 min, rt), supernatant discarded, cells resuspended in PBS and centrifuged again. Cell pellets were resuspended in PBS and cell suspension distributed into 0.2-mL PCR tubes (*Kisker Biotech*, $6x10^6$ Mio cells per tube) and kept at room temperature prior to heat treatment. VioA and DMSO treated samples were heated in parallel for 3 min. to the respective temperature (37°C, 41.2°C, 44°C, 48°C, 53.1°C, 56.3°C, 59.3°C, 62.5°C and 67.1°C) in a PCR cycler (*Techne*), incubated for 3 min. at room temperature, and subsequently snap-frozen in liquid nitrogen and stored at -80°C. Cell lysis was accomplished using four freeze-thaw cycles (incubation for 30 seconds at 25°C, followed by snap-freezing in liquid nitrogen). Subsequently, 50µl PBS was added and the samples subjected to ultracentrifugation (100,000 g, 20 min, and 4°C). 100 µL of the resulting supernatant was transferred into new 1.5 mL tubes. For protein amount normalization, protein concentration of the two lowest temperature point samples (37°C and 41°C) were determined with a sample aliquot (10 µL) using Bradford assay. Proteins were precipitated by adding acetone (400 µL) and incubated overnight (-20°C). Next, precipitated proteins were pelleted (21,000 g, 20 min., 4°C), supernatant discarded and protein pellet resuspended by sonication (10% intensity, 10 sec, Sonopuls HD 2070 ultrasonic rod, *BANDELIN electronic GmbH & Co. KG*) in pre-chilled methanol (500 µL). Protein pellet

washing step was carried out twice. Subsequently, proteins were resuspended in X-buffer (300 µL, 7 M urea, 2 M thiourea in 20 mM Hepes buffer pH 7.5) by sonication (procedure as described above). Proteins were reduced with DTT (1 mM, 1 M stock in ddH_20) and incubated under gentle mixing (25°C, 45 min, 450 rpm). Alkylation of proteins was achieved by the addition of iodoacetamide (5.5 mM, 550 mM stock in ddH_20) and incubated under gentle mixing (25°C, 30 min, 450 rpm). Alkylation reaction was stopped by the addition of DTT (4 mM, 1 M stock in ddH_20) and incubated under gentle mixing (25°C, 30 min, 450 rpm). Proteins were predigested with LysC (3.33 µg/mL, 0.5 mg/mL stock in ddH_20; *Wacko*) under gentle mixing (25°C, 2 h, 450 rpm). TEAB buffer (900 µL, 50mM) was added, and samples further digested with trypsin (4 µL, 0.5 mg/mL stock, sequencing grade, modified; *Promega*) overnight under mixing (37°C, 800 rpm). Digest was stopped the following day by the addition of formic acid (0.1% final concentration; *Sigma-Aldrich*) and peptides desalted using Sep-Pak C18 1 cc Vac cartridges (*Waters*) and the following procedure: Resin was washed with MeCN (1 mL) and elution buffer (80% MeCN, 0.5% FA) prior to equilibration with 0.1% TFA (3 mL). Peptide solutions were loaded to the cartridges and bound peptides washed with 0.1% TFA (3 mL) and 0.5% FA (0.5 mL) and finally eluted with elution buffer (0.75 mL). Peptides were dried using a centrifugal vacuum concentrator (*Eppendorf*) and stored at -80°C. Peptides were reconstituted in elution buffer and a volume of each sample corresponding to 25 µg protein in the two lowest temperature points transferred into new 1.5 mL LoBind tubes. Samples were dried and taken up in TMT buffer 1 (10 µL, 10% MeCN 90% 200 mM TEAB buffer) and incubated under gentle mixing (25°C, 15 min, 400 rpm)**.** Additional TMT buffer 1 (25 µL) was added to each sample. TMT labels were allowed to gain room temperature and taken up in MeCN (41 µL). 10 µL of each label solution was added to a sample according to applied temperature point (see Table S6) and incubated under gentle mixing (25°C, 1 h, 400 rpm). Reaction was stopped by the addition of 5% (v/v) hydroxylamine solution (5 µL, *Sigma Aldrich*) and incubated under gentle mixing (25°C, 15 min, 400 rpm). Labeled peptides were combined into a single sample per experiment, TMT solution 2 (100 µL, 60% (v/v) 200 mM TEAB buffer 40% (v/v) MeCN) added and samples dried using a centrifugal vacuum concentrator. Dried labeled peptides were reconstituted in 0.5% formic acid (200 µL) and desalted using C18 StageTips (eight layers; Empore disk-C18; 47 mm; *Agilent Technologies*) and the following procedure: layers were washed with MeOH (90 µL), elution buffer (200 µL) and 0.5% FA (600 µL). Samples were loaded on stage tips (500g, 2 min) and bound peptides washed with 0.5% formic acid (600 µL) and eluted with elution buffer (300 µL). Eluted peptides were dried in a centrifugal vacuum concentrator. For HILIC fractionation, samples were reconstituted in HILIC buffer A (110 µL, 95% MeCN 5% H_2O and 0.1% TFA), sonicated, vortexed and centrifuged

(21,000 x g, 10 min, 4°C). Peptide fractionation was carried out using an UltiMate 3000 HPLC system (*Dionex*) equipped with an YMC-Pack PVA-Sil column (5 µm, 150 x 2.1 mm, 120 Å, *YMC Europe GmbH*). Gradient elution was carried out with 95% MeCN 5% H_2O and 0.1% TFA (A) and 95% H_2O 5% MeCN and 0.1% TFA (B). 100 µL sample were injected and separated using a 62.5 min gradient (7.5 min 0% B, 50 min to 30% B, 3.5 min to 50% B and 2.5 min to 100% B) at a flow rate of 0.2 mL/min, followed by a washing and column re-equilibration step (12.5 min 100% B, 0.5 min to 0% B and 22.5 min 0% B). During separation, an on-line UV detector set at 215 nm was utilized to monitor peptide mixture elution. Fractions were collected into a 96-well plate (*Eppendorf*) and resulting fractions were pooled into 10 greater fractions. Fractions were dried in a centrifugal vacuum concentrator and fractions 2-9 subjected to LC-MS/MS analysis. Prior to LC-MS/MS analysis dried peptide samples were reconstituted in 1% FA in ddH_2O (10 µL), sonicated for 10 min and filtered using 0.22 µm Ultrafree-MC® centrifugal filters (*Merck*, UFC30GVNB), preequilibrated with 300 µL 1% FA in ddH_2O and transferred into LC-MS vials. The experiment was carried out in duplicates.

2.12 Data collection and statistical analysis

All experiments were performed at least three times (biological replicates) in technical triplicates unless indicated otherwise. Statistical analysis, as well as calculation of IC_{50} and EC_{50} values was conducted with GraphPad Prism software. Bar graphs are shown as mean ± SEM. A two-tailed unpaired Student's t-test or one-way ANOVA, Dunnett's test was performed (* P<0.033, ** P<0.002, *** P<0.001, **** P<0.0001). For western blot and confocal microscopy experiments, representative images of at least three biological replicates are shown. For xCELLigence and Seahorse experiments, representative curves of three independent data sets are depicted.

3. Results Part I - Vioprolide A

3.1 Functional characterization

3.1.1 Vioprolides inhibit cancer cell proliferation

In 1996, the isolation of Vioprolides A-D and their potent antifungal and anticancer activities were reported by Schummer *et al. (16)*. However, no further investigations concerning their antitumor activity have been described up to date. Furthermore, the initial publication indicated a diverse specificity of the family members towards fungi, yeast and mammalian cells (*16*). Hence, in order to select the most potent growth inhibitory compound in human cancer cells for subsequent mode of action analyses, this study initiated with a comparative analysis of Vioprolide A, B, C and D (VioA-D), performed in the human acute lymphoblastic leukemia (ALL) cell line Jurkat. Of note, VioA exhibited the highest antiproliferative activity with a half maximal inhibitory concentration (IC_{50}) of 4.4nM, determined by cell titer blue assay after 72h (Figure 8B). In line with previous data (*16*), the Vioprolide derivatives showed significant differences in bioactivity, demonstrating that the structural composition of their N-heterocycles (Figure 8A) is crucial for their potency.

A

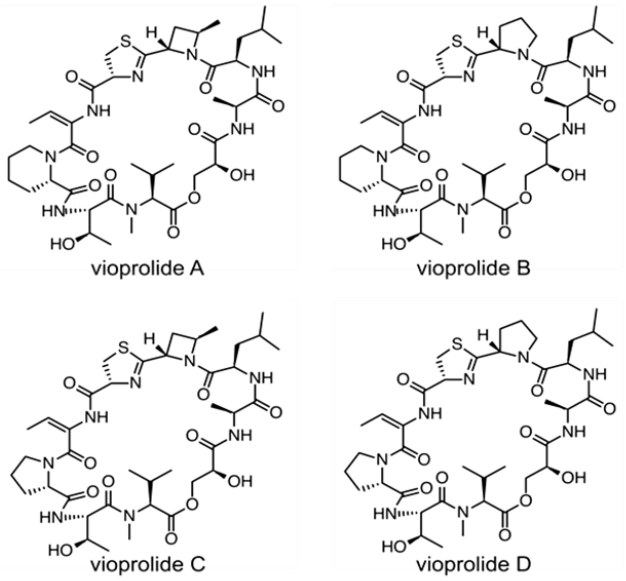

B

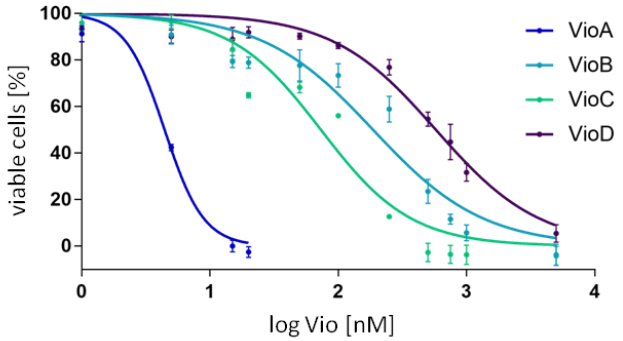

Derivative	VioA	VioB	VioC	VioD
IC_{50} [nM]	4.4 ± 0.3	187 ± 24	73 ± 8	577 ± 49

Fig. 8 Dose-dependent inhibition of leukemic cell proliferation by Vioprolide derivatives. (**A**) Chemical structures of Vioprolide A, B, C and D. (**B**) Dose response curves and corresponding IC_{50} values of Jurkat cells incubated with Vioprolide A, B, C and D determined by cell titer blue assay after 72h. Data points always represent the mean ± SEM of three independent experiments performed in triplicates.

Subsequently, VioA was tested against a panel of cancer cell lines, including leukemia cell lines (CEM, Jurkat, HL-60) and solid cancer cell lines (T24, HeLa). Thereby, VioA displayed low nanomolar IC_{50} values in all tested cell lines, illustrating its potency in various cancer types (Figure 9).

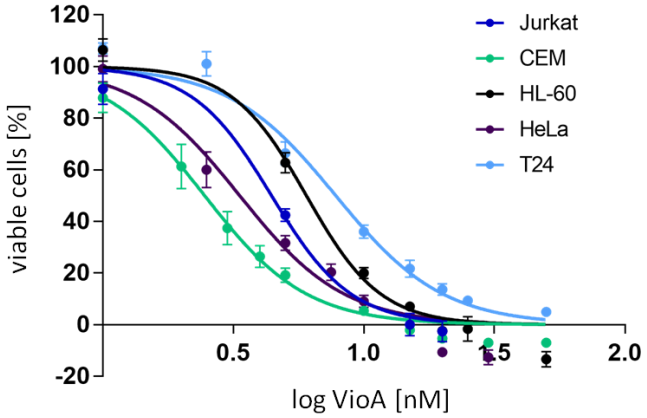

Cell line	Cell type	IC_{50} [nM]
Jurkat	ALL	4.4 ± 0.3
CEM	ALL	2.5 ± 0.1
HL-60	AML	6.0 ± 0.3
HeLa	Cervical carcinoma	3.3 ± 0.3
T24	Bladder carcinoma	7.8 ± 0.4

Fig. 9 VioA inhibits proliferation in various cancer cell lines. Proliferative capacity of different cancer cell lines and corresponding IC_{50} values were determined by cell titer blue assay (suspension cell lines) or crystal violet staining (adherent cell lines) after 72h. Data points always represent the mean ± SEM of three independent experiments performed in triplicates.

3.1.2 Impact of Vioprolide A on apoptosis and cell cycle progression

To analyze whether enhanced cell death rates contribute to diminished proliferative capacity of VioA treated cancer cells, apoptosis assays were performed. Propidium iodide (PI) staining followed by flow cytometry was conducted according to Nicoletti *et al.* VioA exhibited an EC_{50} of 17.3 and 23.5 nM in CEM and Jurkat cells, respectively, signifying a relatively high apoptotic rate in acute lymphoblastic leukemia (ALL) cells (Figure 10A, C), compared to the AML cell line HL-60 and the solid cancer cell lines HeLa and T24 (Figure 10B, C). The induction of apoptotic cell death was furthermore verified by caspase-3 (CASP3) and caspase-8 (CASP8) activation and the cleavage of the enzyme poly ADP ribose polymerase (PARP), analyzed by western blot (Figure 8D).

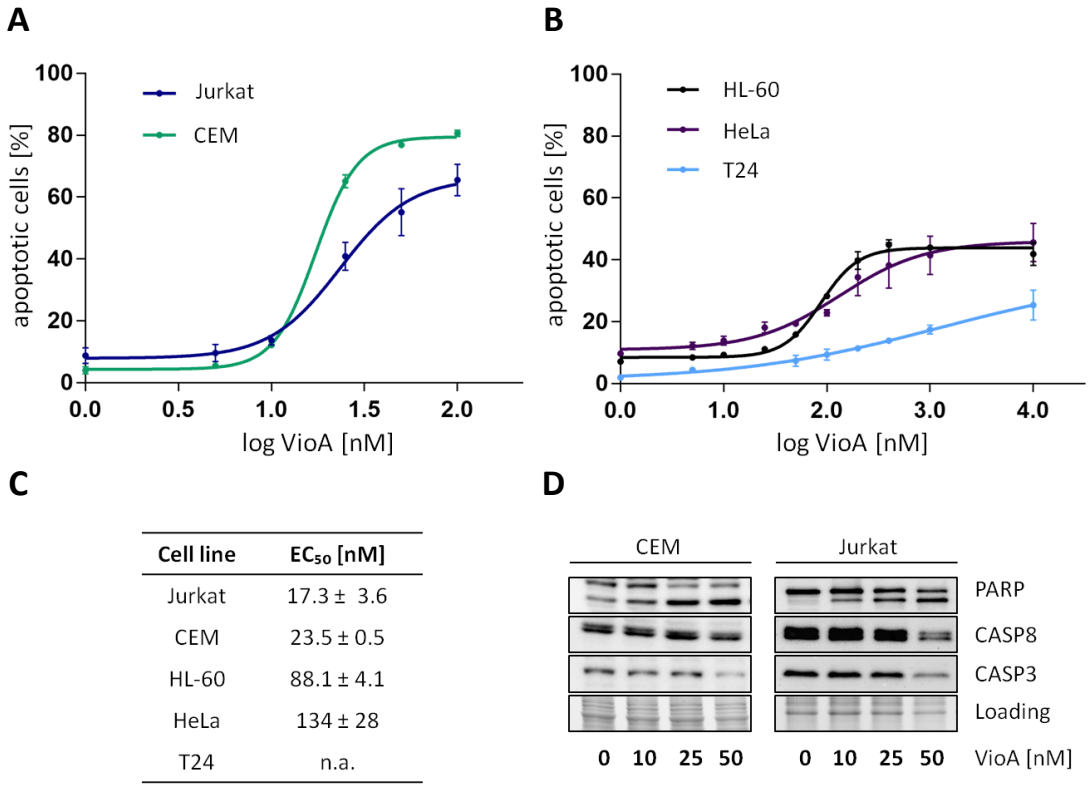

Cell line	EC_{50} [nM]
Jurkat	17.3 ± 3.6
CEM	23.5 ± 0.5
HL-60	88.1 ± 4.1
HeLa	134 ± 28
T24	n.a.

Fig. 10 Apoptosis induction in various cancer cell lines. Apoptosis of (**A**) Jurkat and CEM cells as well as (**B**) HL-60, T24 and HeLa cells treated with VioA for 24h. Percentage of apoptotic cells was determined by propidium iodide staining and flow cytometry. Data points always represent the mean ± SEM of three independent experiments performed in triplicates. (**C**) Corresponding EC_{50} values. (**D**) Confirmation of VioA induced apoptotic cell death by western blot analysis of caspase activation and poly ADP ribose polymerase (PARP) cleavage. Jurkat and CEM cells were treated with VioA for 24h and protein levels of procaspase-3 (CASP3), procaspase-8 (CASP8) and cleavage of PARP were determined. Representative blots out of three independent experiments are shown.

To confirm the potency of VioA in ALL and to analyze its putative therapeutic relevance, the compound was subsequently tested in ALL patient derived xenograft (PDX) cells. In accordance with previous cell culture experiments, VioA treated ALL samples of diverse background (see section 2.1.1.2) generally showed an increased apoptosis rate after 24h treatment compared to DMSO control as shown by flow cytometry. Notably, peripheral blood mononuclear cells (PBMCs) of healthy donors barely responded to VioA compared to PDX samples (Figure 11).

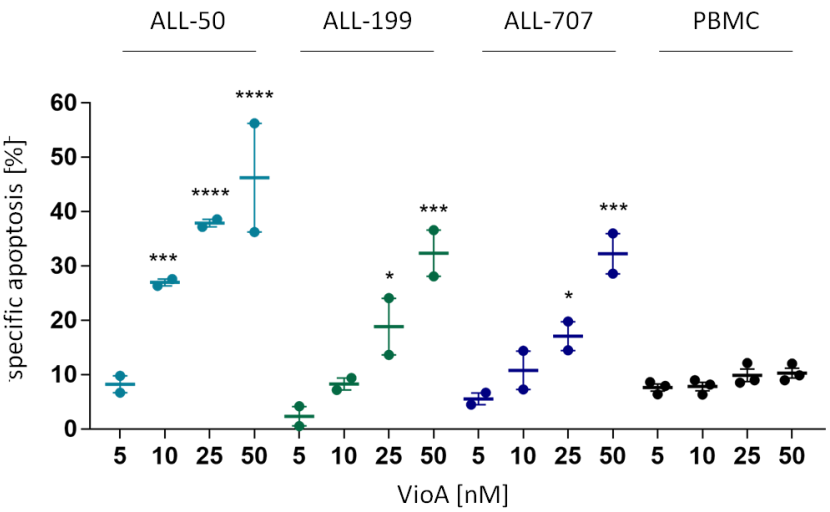

Fig. 11 VioA induces apoptosis in PDX cells. ALL PDX cells of diverse background and PBMCs treated with VioA for 24h. Percentage of apoptotic cells was determined by flow cytometry and specific apoptosis was calculated towards DMSO control. Data points represent independent experiments (PDX cells: n=2, PBMC: n=3) performed in triplicates, one-way ANOVA, Dunnett's test, * P<0.033, *** P<0.001, **** P<0.0001.

Of a wide range of stimuli and conditions that can trigger apoptosis in cells, there are two main pathways to distinguish: the intrinsic (mitochondria mediated) and the extrinsic (death receptor mediated) pathway. To decipher which pathway is addressed by VioA treatment, characteristics of mitochondria mediated apoptosis were examined in VioA treated Jurkat cells. Mitochondrial membrane permeabilization is considered to be a general attribute of mitochondria mediated cell death and represented as a "point of no return" event resulting in apoptosis. Under physiological conditions, mitochondria display a high mitochondrial membrane potential (ΔΨm) while in cells undergoing apoptosis ΔΨm is dissipating (*61*). Thereby, the pro-apoptotic Bcl-2 family members BAX and BAK are recruited to the outer mitochondrial membrane (OMM) and oligomerize to mediate mitochondrial outer membrane permeabilization (MOMP), resulting in cytochrome C release and caspase activation (*42*).

Here, we used the lipophilic cationic molecular probe JC-1 to measure the alterations of ΔΨm in VioA treated cells as the dye exhibits ΔΨm dependent aggregation. Of note, loss of ΔΨm could be demonstrated by decreased red/ green fluorescence ratio in VioA treated Jurkat cells after 24h (Figure 12A). Moreover, VioA strikingly downregulated the expression levels of antiapoptotic Bcl-2 family proteins Bcl-2, Bcl-xL and Mcl-1 after 24h treatment (Figure 12B). To further test the role of anti-apoptotic Bcl-2 family members on VioA- induced apoptosis, Bcl-2 and Bcl-xL overexpressing Jurkat cells (Figure 12C) were challenged with VioA. Additionally, a Jurkat cell line deficient for caspase-8 (Figure 12C) was tested. Caspase-8 plays a role in the extrinsic apoptotic pathway execution that is,

independently from the intrinsic pathway, activated upon death ligand (e.g. FasL) binding to death receptors and receptor ligation (*62*). Jurkat cells overexpressing Bcl-2 or Bcl-xL were significantly less sensitive towards VioA treatment than the empty vector control cell line Jurkat neo, whereas Jurkat Casp8 -/- exposed a sensitivity towards VioA equally to Jurkat neo (Figure 12D-E). These results indicate that apoptosis induction by VioA can only be effectively executed upon functional mitochondrial apoptosis signalling and that the extrinsic pathway does not contribute to VioA induced apoptosis.

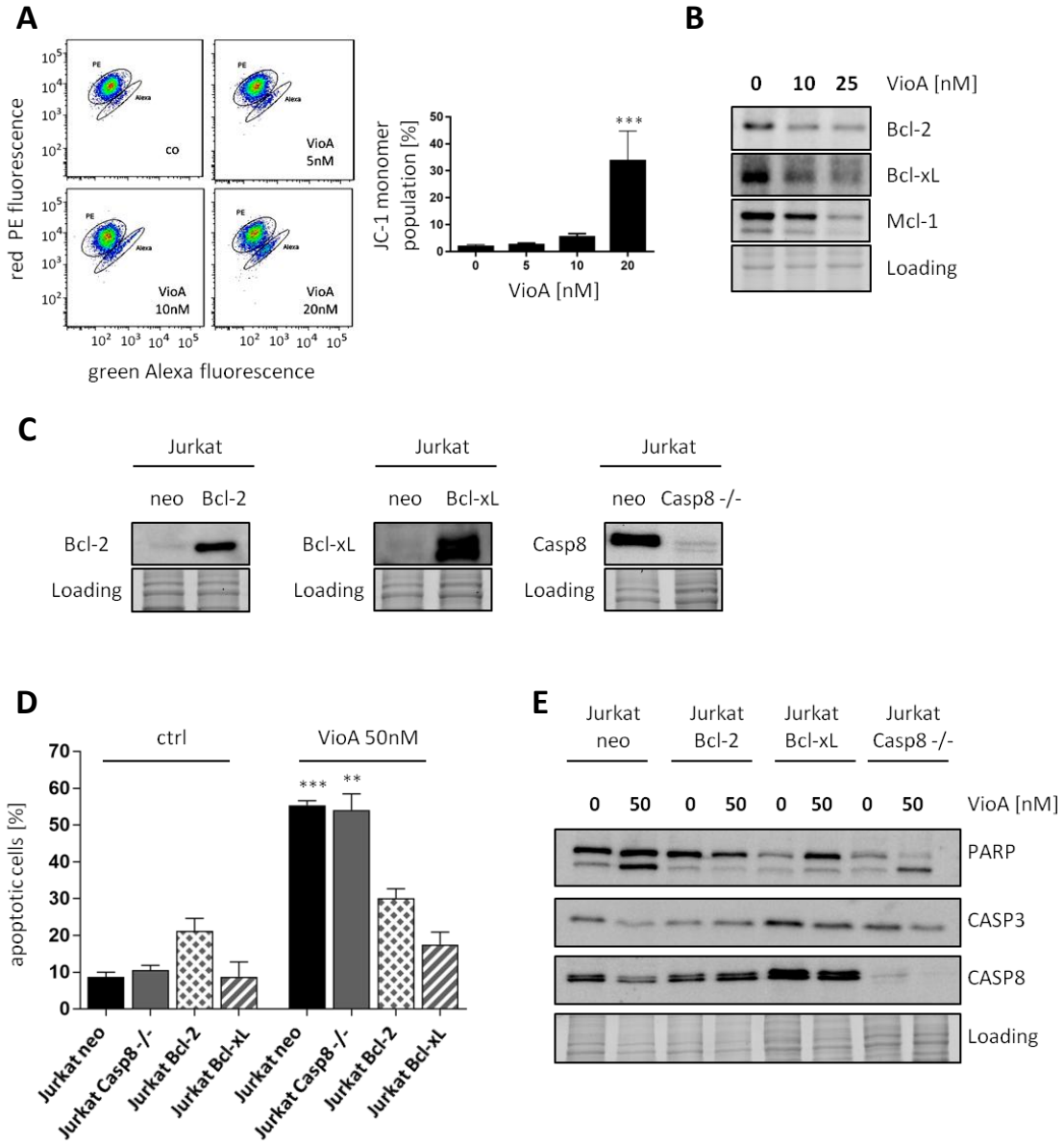

Fig. 12 Vioprolide A causes mitochondria mediated apoptosis. (**A**) JC-1 was used as fluorescent probe for cytometric determination of mitochondrial membrane potential (Δϕm) in Jurkat cells treated with VioA as indicated for 24h. The green fluorescent JC-1 monomer population represents cells with loss of Δϕm and was quantitatively measured by flow cytometry. Bars represent the mean ± SEM of three independent experiments performed in triplicates, one-way ANOVA, Dunnett's multiple comparisons test, *** P<0.001. (**B**) Expression levels of the anti-apoptotic mitochondrial proteins Bcl-2, Bcl-xL and Mcl-1 decline upon VioA treatment as indicated for 24h. (**C**) Verification of Bcl-2 and Bcl-xL overexpression as well as caspase-8 deficiency by western blot. (**D**) Apoptosis induction is suppressed in Bcl-2 and Bcl-xL overexpressing Jurkat cells respectively (Jurkat Bcl-2, Jurkat-Bcl-xL) compared to the empty vector control cell line (Jurkat neo). Caspase-8 deficiency (CASP8 -/-) does not rescue Jurkat cells from apoptosis induction by VioA. Percentage of apoptotic cells was determined by propidium iodide staining and flow cytometry after 24 h. Bars always show the mean ± SEM of three independent experiments performed in triplicates, two-tailed unpaired Student's t-test, ** P<0.002, *** P<0.001. (**E**) Induction of apoptosis analyzed by immunoblotting. Jurkat cells were treated with VioA as indicated for 24h and protein levels of caspase-3 (CASP3), caspase-8 (CASP8) and poly ADP ribose polymerase (PARP) were determined. (B, C, E) Representative blots out of three independent experiments are shown.

Analysis of cell cycle progression in Jurkat cells treated with VioA for 24h furthermore revealed a significant decrease of cells in S-phase and an increased proportion of cells in G1, which was measured by propidium iodide staining followed by flow cytometry (Figure 13).

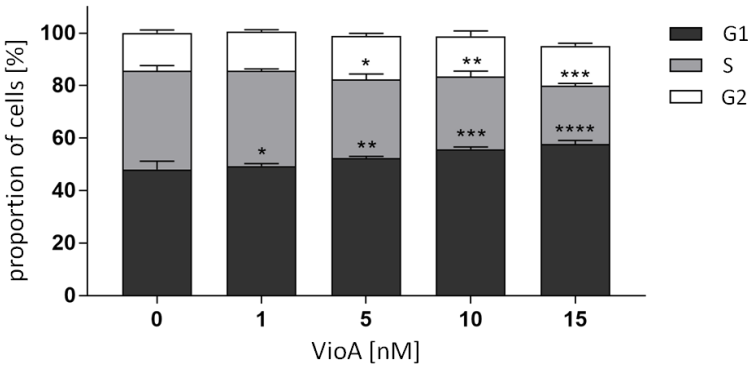

Fig. 13 Influence of VioA on cell cycle progression of Jurkat cells. Cell cycle analysis of Jurkat cells treated with VioA as indicated for 24h. Cellular DNA content was determined by propidium iodide (PI) staining and flow cytometry. Proportion of cells in different stages of the cell cycle was calculated with the cell cycle tool provided by FlowJo software. Bars always represent the mean ± SEM of three independent experiments performed in triplicates, one-way ANOVA, Dunnett's multiple comparisons test, * P<0.033, ** P<0.002, *** P<0.001, **** P<0.0001.

3.1.3 Vioprolide A reduces cancer cell migration and invasion

Besides extensive cell growth, metastasis of primary cancer cells to distant organs is a major challenge in the management of tumors. For this reason, the ability of VioA to inhibit the migratory and invasive potential of the metastatic cancer cell line T24 was investigated using a transwell migration assay and a spheroid based invasion assay, respectively.

In a Boyden chamber assay, cells were allowed to migrate through transwell 8µm pores towards a chemoattractant and migratory cells were stained and counted after 16h (Figure 14). At subtoxic concentrations, VioA significantly reduced the migration capacity of the highly invasive bladder carcinoma cell line T24.

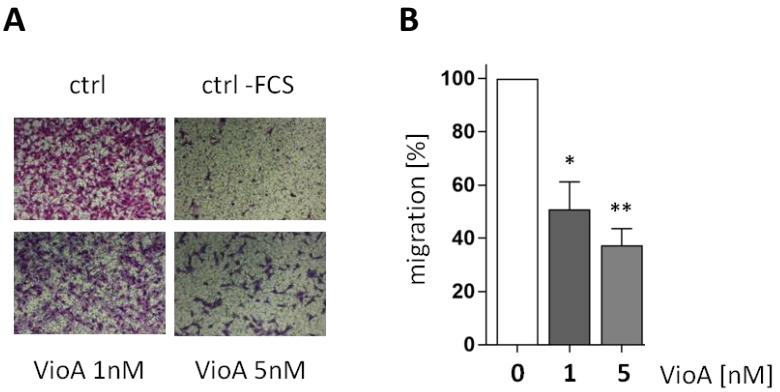

Fig. 14 Anti-migratory effects of Vioprolide A. (**A**) Representative images of Boyden chamber inserts. (**B**) Quantification of migrated cells was performed with ImageJ software. Bar diagram showing the number of migrated cells as mean ± SEM of three independent experiments after normalisation to DMSO control (ctrl), one-way ANOVA, Dunnett's test, * P<0.033, ** P<0.002.

Invasion into healthy surrounding tissues is generally considered as a hallmark of cancer (*45*). To determine the invasiveness of VioA treated cells, a three-dimensional (3D) spheroid assay was performed. The major advantage provided by 3D spheroid assays is that tumor cells are organized in a 3D structure, mimicking a solid tumor microenvironment. Hence, cells within a spheroid are challenged with tumor-like harsh conditions like hypoxia or nutrient deprivation, changing gene expression that can promote migration and invasion (*57*). As shown in Figure 15, VioA dose-dependently decreased T24 spheroid cell invasion into surrounding matrix (Matrigel™), which was monitored over a time-period of 72h.

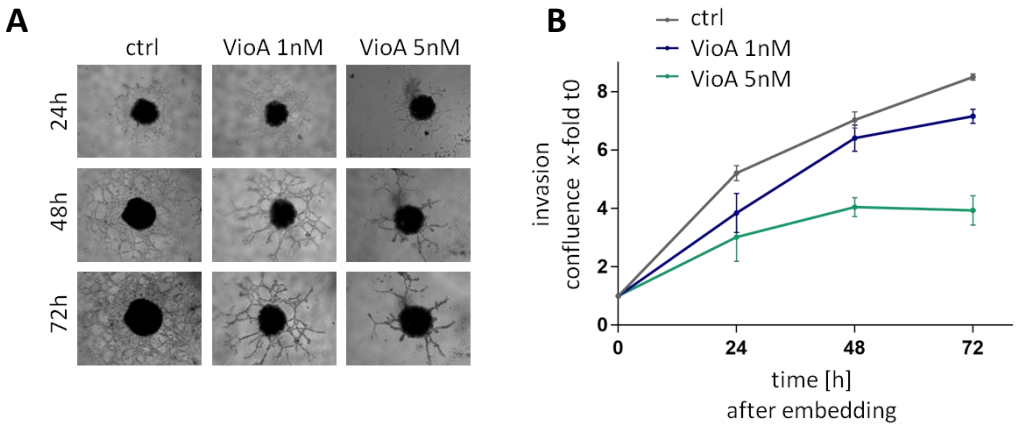

Fig. 15 Reduction of T24 spheroid invasion. Spheroids were generated by seeding T24 cell suspension into ultra-low attachment plates and were allowed to grow for 48h before embedding into Matrigel™ and treatment with VioA as indicated. Pictures were taken 24h, 48h and 72h after embedding. (**A**) Representative pictures out of three independent experiments performed in triplicates are shown. (**B**) Quantification of invasion with the ImageJ confluence application normalized to day 0. Data points represent the mean ± SEM of three independent experiments performed in triplicates.

3.2 Target identification via thermal proteome profiling

To elucidate the molecular mechanism underlying the potent biological activity of the natural compound VioA, target identification was performed. Thermal proteome profiling (TPP) was thereby chosen as modification-independent strategy of the complex natural product. TPP works in living cells by determining stabilizing effects on proteins upon compound binding at elevated temperatures (*63-65*). Sample preparation, MS analysis as well as data processing were performed as described in section 2.11 by Volker Kirsch (group of Prof. Stefan Sieber, TU Munich, Germany).

In detail, Jurkat cells were incubated with VioA (1µM) or DMSO and were subsequently exposed to a range of temperature points between 37°C and 67°C. Cells were lysed, soluble proteins isolated by ultracentrifugation; tryptically digested and labelled using isobaric tandem mass tag labels (TMT). Respective labelled samples were combined, subjected to hydrophilic-interaction chromatography (HILIC) fractionation and finally analyzed by LC-MS/MS (Figure). After filtering, T_m shifts that were calculated from two replicates of VioA versus DMSO treatment were visualized (Figure S1). All hits (proteins with a temperature shift of minimum 1°C in both biological replicates) were manually inspected and 67 proteins exhibited proper melting curves.
U2 snRNP-associated SURP motif-containing protein (U2SURP) and nucleolar protein 14 (NOP14) pertained as highly stabilized upon VioA treatment (Figure 16). NOP14, which is showing the highest stabilization, is crucial for ribosome biosynthesis. Ribosome biogenesis displays an essential process for cancer cell growth and could therefore be considered as plausible target of a cytotoxic compound like VioA. Consequently, NOP14 was selected for in-depth validation.

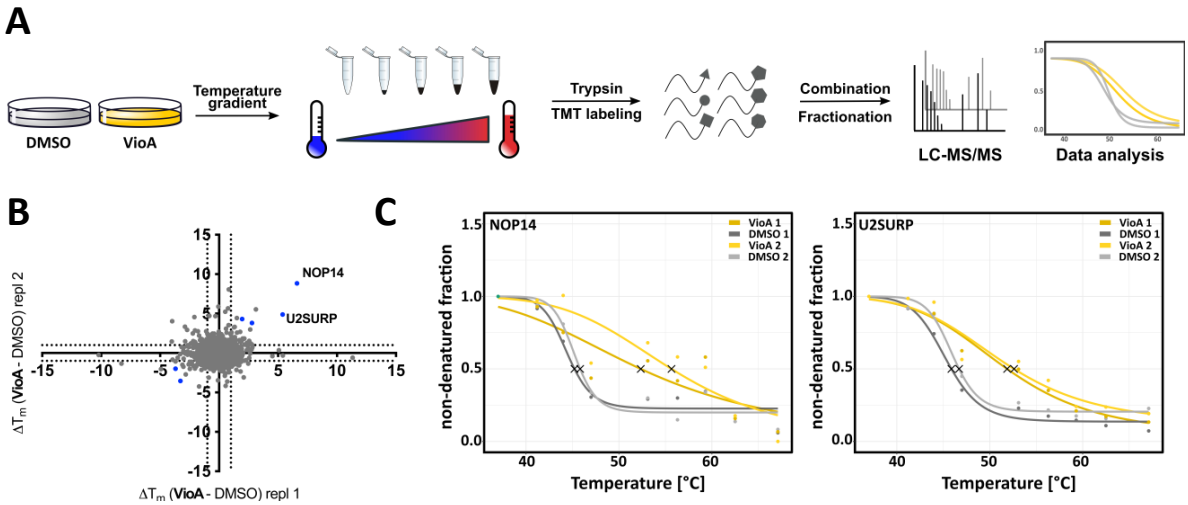

Fig. 16 Target identification of VioA in Jurkat cells using thermal proteome profiling. (**A**) Schematic workflow of thermal proteome profiling experiment. Intact Jurkat cells were treated with 1µM VioA or DMSO respectively for 1h to ensure compound-target engagement. Subsequently, aliquots were incubated at 9 different temperature points (37°C – 67°C), centrifuged, proteins in supernatant digested, TMT-labelled, HILIC fractionated and analyzed by mass spectrometry. (**B**) Scatter plot of Tm shifts calculated from two biological replicates of VioA vs. DMSO treatment. Melting point shifts passing all significance criteria (Table S1) are shown in blue. Data were processed using MaxQuant and thermal response curve fitting as well as melting point calculation was carried out using the TPP TR R package. (**C**) Thermal response curves for NOP14 and U2SURP proteins of VioA treated (orange) and DMSO (grey) treated cells. TPP experiment was carried out in two independent replicates. Experiment was performed by Volker Kirsch in the laboratory of Prof. Dr. Stephan Sieber (TU Munich, Germany).

3.3 Target verification

3.3.1 Inhibition of rRNA production without nucleolar disassembly

The nucleolar protein 14 (NOP14) is crucial for the biosynthesis of new ribosomes, playing a significant role in 40S ribosome subunit formation as well as maturation of 18S rRNA (*66*). In eukaryotes the first step of ribosome biogenesis takes place in the nucleoli, where ribosomal DNA transcription by DNA polymerase I (Pol I) occurs. Ribosomal DNA encodes for ribosomal RNA (rRNA), which in turn builds the nucleic acid backbone of the ribosome (*29*). In NOP14 siRNA knockdown cells, rRNA levels in nucleoli as visualized by 5-Fluorouracil (5-FU) incorporation, immunostaining and confocal microscopy were significantly lower compared to non targeted (nt) control cells (Figure 17A). Interestingly, VioA treated cells as well exhibited decreased rRNA levels compared to DMSO-treated control cells, suggesting an equivalent effect (Figure 17B). Actinomycin D (ActD), which intercalates into GC-rich duplex-DNA, thereby inhibiting Pol I transcription served as a positive control for blocked rRNA production (Figure 17B).

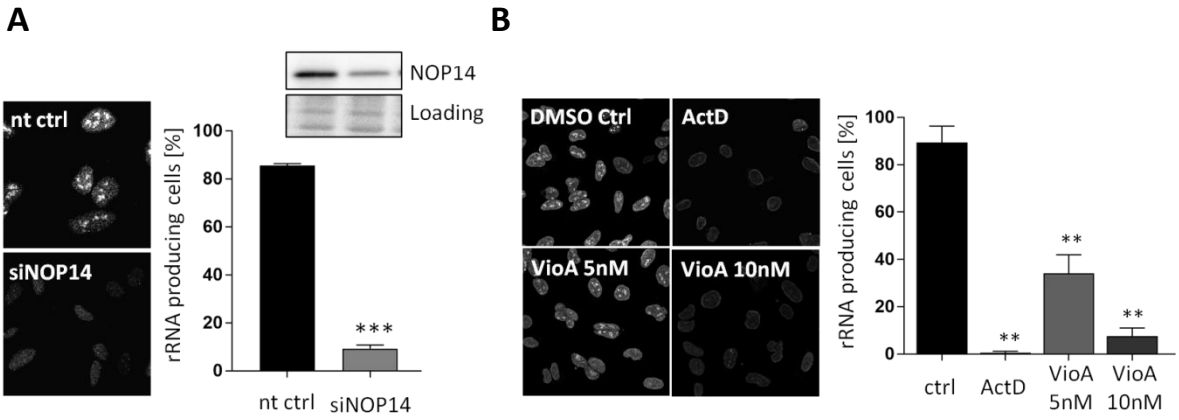

Fig. 17 Inhibition of rRNA production by NOP14 silencing and VioA treatment. (**A**) Nuclear run on assay with HeLa cells transfected with non targeting (nt) or NOP14 siRNA for 48h. Cells with nucleolar rRNA foci were counted as rRNA producing cells and values were normalized towards control. (**B**) Nuclear run on assay with HeLa cells treated either with VioA for 24h or with 6µM Actinomycin D (ActD) for 2h, which served as positive control. Cells with nucleolar rRNA foci were counted as rRNA producing cells. Bars represent the proportion of cells with rRNA foci as mean ± SEM of three independent experiments, two-tailed unpaired Student's t-test, *** P<0.001 (A), one-way ANOVA, Dunnett's multiple comparisons test, ** P<0.002 (B).

Moreover, ongoing rDNA transcription is necessary for the formation of nucleoli, whereas perturbations of the transcriptional machinery lead to their rapid disassembly (*26*). Consistently, ActD treatment led to distribution of the nucleolar protein NOP14 in the whole nucleus due to nucleolar disruption, subsequently to Pol I transcription inhibition. VioA treatment however, revealed no alterations in nucleolar morphology and localization as visualized by NOP14 immunostaining (Figure 18). These results indicate that VioA does not interfere with ribosome biogenesis at the level of transcription.

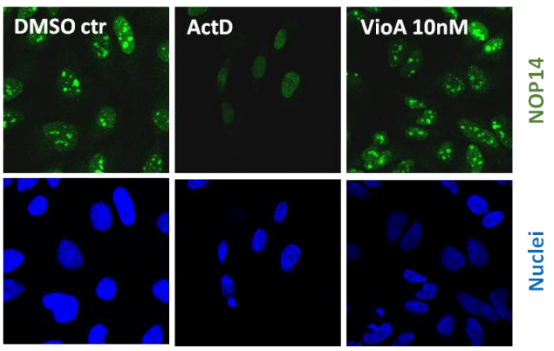

Fig. 18 Nucleoli remain intact upon VioA treatment. HeLa cells treated with 10nM VioA for 24h or 6µM ActD for 2h and immunostained for NOP14. Nuclei were visualized by Hoechst 33342 staining. Representative images out of three independent experiments are shown.

3.3.2 Expression of NOP14 in different cell types

Ribosome biogenesis is enhanced in cancer cells due to their high demand of continuous ribosome production for extensive cell growth (*26, 28*). A comparison of NOP14 expression levels in various cancer cell lines, an ALL PDX cell sample and PBMCs of healthy donors revealed that ALL cell lines Jurkat and CEM, as well as the tested PDX cells feature high endogenous NOP14 levels in contrast to HL-60 cells (Figure 19). Of note, also PBMCs revealed lower NOP14 protein levels, suggesting a possible correlation between sensitivity of cells towards VioA induced apoptosis and NOP14 expression.

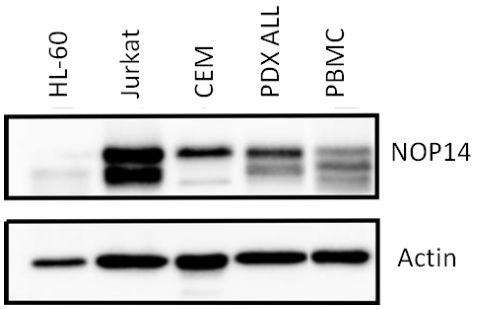

Fig. 19 NOP14 protein expression in various cancer cell lines. Basal expression of NOP14 in different leukemia and solid cancer cell lines and PBMCs of healthy donors was investigated by immunoblotting. Actin served as loading control. Representative blot out of three independent experiments is shown.

3.3.3 NOP14 plays a role in cancer cell growth

To elucidate if there is a functional link between the vast growth inhibitory and apoptosis inducing effects of VioA and its potential target NOP14, proliferation and apoptosis assays were conducted after successfully knocking down NOP14 in HeLa cells using siRNA (Figure 20E). Proliferation was clearly diminished in NOP14 siRNA treated HeLa cells compared to non-targeted (nt) control cells, as displayed by increased doubling time values (nt ctrl: 33h, siNOP14 62h) (Figure 20A). These results provide evidence that the growth inhibitory effect of VioA is mainly mediated by NOP14. Conversely, silencing of NOP14 did not induce apoptotic cell death in HeLa cells (Figure 20B-C). Additional VioA treatment of siRNA transfected HeLa cells displayed a slightly increased apoptosis rate in NOP14 silenced cells compared to nt control cells (Figure 20D).

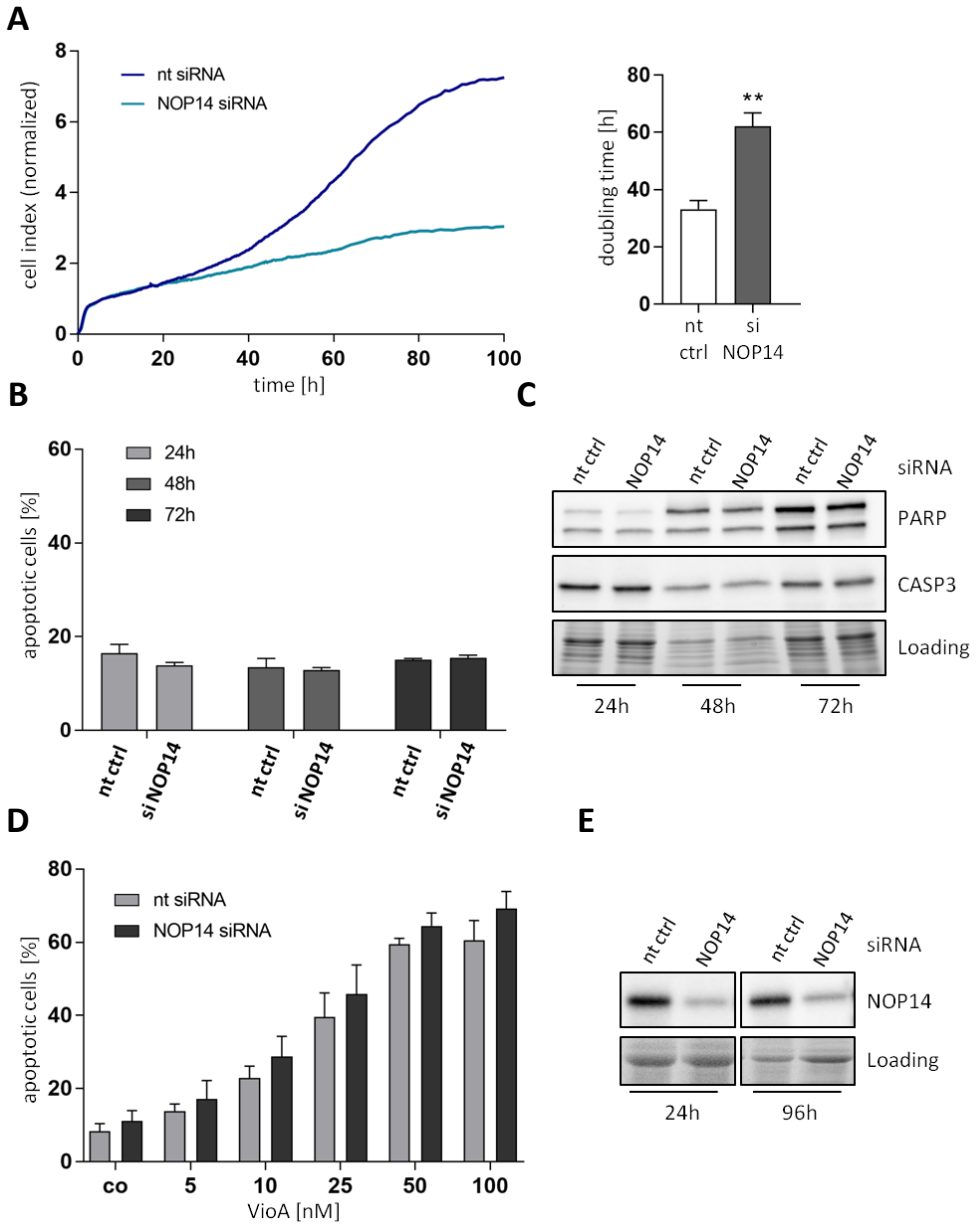

Fig. 20 Functional link between NOP14 and anticancer effects of VioA. (**A**) xCELLigence real-time proliferation measurement of HeLa cells either transfected with nt or NOP14 siRNA for 24h before seeding into E-plates. Proliferation was monitored for the subsequent 72h. Representative curve out of three independent experiments is shown. Respective doubling time values were calculated using xCELLigence RTCA software. Bars represent the mean ± SEM of three independent experiments, two-tailed unpaired Student's t-test, ** P<0.002. (**B**) Nicoletti apoptosis assay of HeLa cells either transfected with nt or NOP14 siRNA for the indicated time points. Bars represent the mean ± SEM of three independent experiments performed in triplicates. (**C**) Induction of apoptosis analyzed by immunoblotting. Jurkat cells were treated with VioA as indicated for 24h and protein levels of caspase-3 (CASP3) and poly ADP ribose polymerase (PARP) were determined. (**D**) Nicoletti apoptosis assay of HeLa cells either transfected with nt or NOP14 siRNA for 24h before stimulation with VioA for further 24h. Bars represent the mean ± SEM of three independent experiments performed in triplicates. (**E**) Verification of NOP14 siRNA knockdown by western blot analysis.

3.4 Target interactome analysis

3.4.1 Pulldown of NOP14 interactome

Previous studies in yeast showed that various protein-protein interactions with NOP14 are essential for a proper working ribosome biogenesis machinery (*67*). Thus, we further focused on unravelling the interactome of NOP14 in the human cell line Jurkat via MS-based co-immunoprecipitation (co-IP) experiments. MS-based co-IP was conducted via an immobilized anti-NOP14 antibody in presence of DSSO as crosslinker to enable also temporal binding partners being trapped as applied previously (Figure 21) (*68*). MS-based co-IP experiments were conducted by Volker Kirsch in the laboratory of Prof. Dr. Stephan Sieber (TU Munich, Germany).

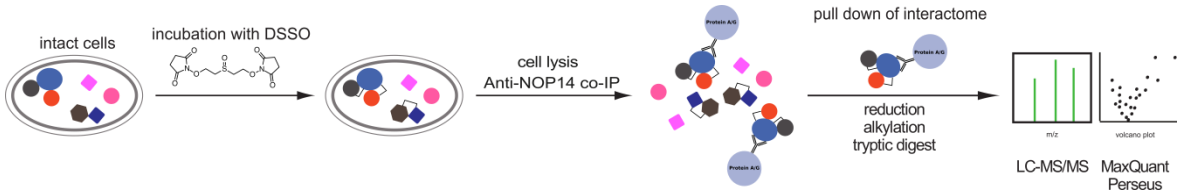

Fig. 21 Schematic workflow of MS-based co-immunoprecipitation. Living cells were either treated with 10 nM VioA or DMSO, respectively, for 24 hours. Subsequently, DSSO linker was added to ensure covalent linkage of protein complexes within cells. NOP14 and linked interacting proteins were enriched using an anti-NOP14 antibody immobilized on protein A/G beads. Tryptic peptides were analyzed via LC-MS/MS. Experiments were performed by Volker Kirsch in the laboratory of Prof. Dr. Stephan Sieber (TU Munich, Germany).

Analysis of pulled-down proteins via LC-MS/MS identified several highly enriched proteins compared to normal rabbit isotype control co-IP in Jurkat cells (Table S2), amongst others: the nucleolar complex protein 4 homolog (NOC4L) and the ribosomal RNA small subunit methyltransferase NEP1 (EMG1) (Figure 22). By now, detailed studies on the interactions between the yeast homologues of NOP14 and EMG1 (*66*) as well as NOC4L (*69*) revealed that physical interplay with both proteins is essential for proper maturation of 18S rRNA and 40S assembly and export.

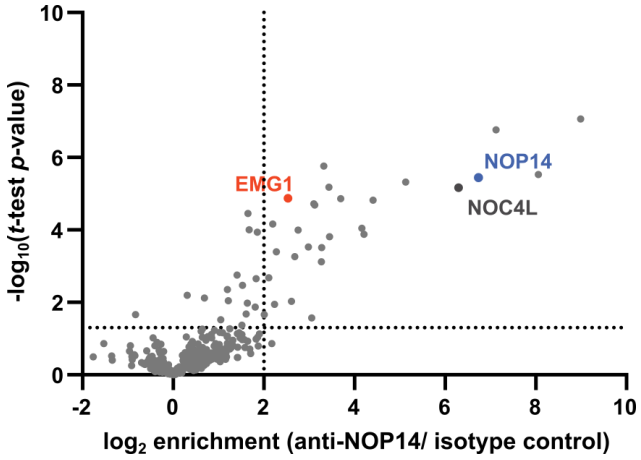

Fig. 22 MS-based co-IP with NOP14 antibody. Volcano plot represents two-sample *t*-test results of anti-NOP14 co-IP compared to isotype control co-IP (n=4). Cutoff criteria were defined as $\log_2$ = 2 (4-fold enrichment) enrichment factor and $-\log_{10}$ (*t*-test *p*-value) = 1.3 (dotted lines). NOP14 is colored in blue, NOC4L in dark grey and EMG1 in red. Experiments were performed by Volker Kirsch in the laboratory of Prof. Dr. Stephan Sieber (TU Munich, Germany).

3.4.2 Selective inhibition of NOP14-EMG1 interaction

In order to identify VioA susceptible interactions, a western blot based co-IP without crosslinking was performed with compound vs. vehicle treatment for 24h prior to NOP14 pulldown. Stimulation with VioA led to a significant depletion of the NOP14-EMG1 interaction (Figure 23A). Remarkably, the interaction between NOP14 and NOC4L remained unperturbed upon VioA treatment, indicating a selective inhibition of the NOP14-EMG1 interface (Figure 23A). Of note, the endogenous expression levels of NOP14, NOC4L and EMG1 remained unaffected (Figure 23B), further signifying that reduced EMG1 levels in western blot based co-IP are result of reduced physical interplay between NOP14 and EMG1.

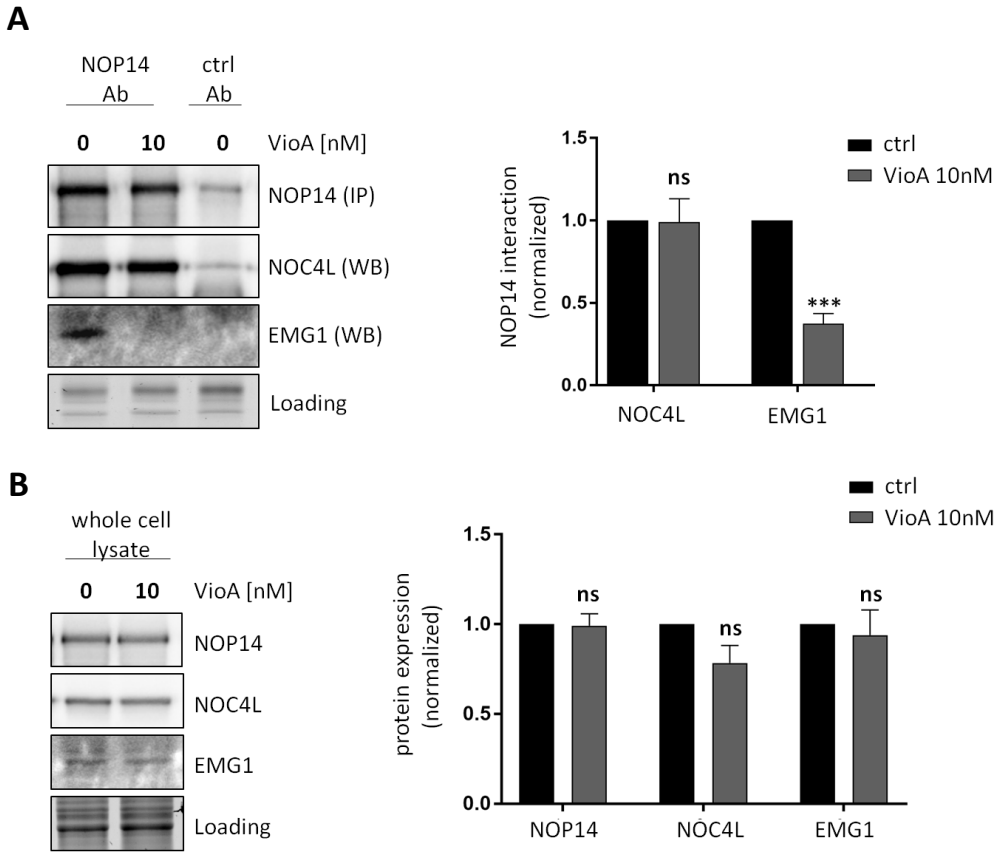

Fig. 23 VioA disrupts NOP14-EMG1 interaction without influencing respective endogenous protein levels. (**A**) Co-IP of NOP14 in Jurkat cells and detection of NOP14 and interaction partners NOC4L/ EMG1 by western blot analysis. A representative experiment out of three independent experiments is shown. Bars represent the mean ± SEM of three independent experiments, two-tailed unpaired Student's t test, *** P<0.001. (**B**) Western blot analysis of NOP14, NOC4L and EMG1 expression levels of Jurkat cells either treated with DMSO or 10nM VioA, respectively for 24h. Bars represent the mean ± SEM of three independent experiments, two-tailed unpaired Student's t test, ns P>0.05.

According to literature, the NOP14-NOC4L complex is required for the nucleolar localization of NOP14 (*69*). Immunostaining of HeLa cells treated with VioA revealed that NOP14 maintains its nucleolar localization also upon VioA stimulation (Figure 24), further substantiating that the heterocomplex NOP14-NOC4L pertains upon treatment. By contrast, treatment of VioA led to an increased amount of EMG1 in the cytoplasm, whereas in DMSO treated cells EMG1 is mainly located in the nucleus. This observation is in line with previous studies, stating that NOP14 is required for nuclear localization of EMG1 (*66*). To furthermore check if the EMG1 delocalization is a possible general effect upon ribosome biogenesis inhibition, HeLa cells were stimulated with Doxorubicin (Doxo), inhibiting ribosome biogenesis by interfering with Pol I transcription. As it was to be expected, NOP14 lost its nucleolar localization because of nucleolar disintegration upon Doxo stimulation (Figure 24). Conversely, also in Doxo treated cells, EMG1 was mainly

localized in the nucleus, excluding a general effect of ribosome biogenesis inhibition on EMG1 delocalization.

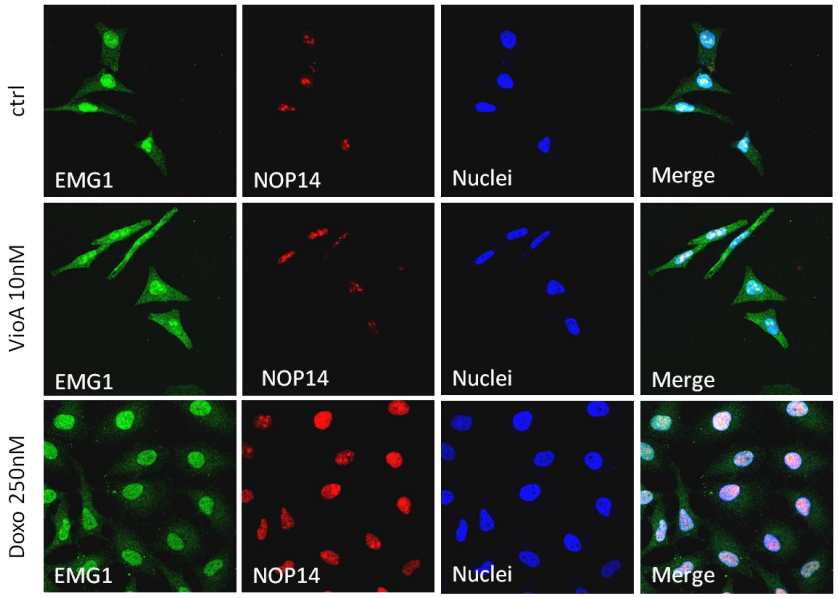

Fig. 24 VioA causes delocalization of EMG1. HeLa cells treated with 10nM VioA for 24h or 250nM Doxorubicin (Doxo) for 2h were co-stained for NOP14 (red) and EMG1 (green). Nuclei were stained with Hoechst 33342. Representative images out of three independent experiments performed in duplicates are shown.

3.5 Summary

In summary, vioprolides represent a unique class of natural compounds with potent bioactivity towards cancer cells in the nanomolar range. ALL cancer cells showed high sensitivity towards VioA apoptosis induction, in contrast to PBMCs, introducing VioA as promising lead structure for cancer cell targeting. By applying TPP as target identification approach in cooperation with the group of Prof. Sieber (TU Munich, Germany), we were able to identify nucleolar protein 14 (NOP14), as interaction partner of VioA. NOP14 plays a key role in ribosome biogenesis, more precisely, the assembly and export of the small ribosomal subunit. Remarkably, VioA represents the first small molecule addressing this pathway. Of note, NOP14 was found highly expressed in ALL in contrast to PBMCs, offering a prospective for a selective therapeutic approach. Closer mechanistic studies furthermore revealed that VioA alters the interaction of NOP14 with EMG1. Our study highlights the potential of targeting the NOP14-EMG1 interface, and thereby ribosome biogenesis, as a promising anticancer strategy and underlines the great capability of VioA as biochemical tool in cancer research, as well as for future drug development.

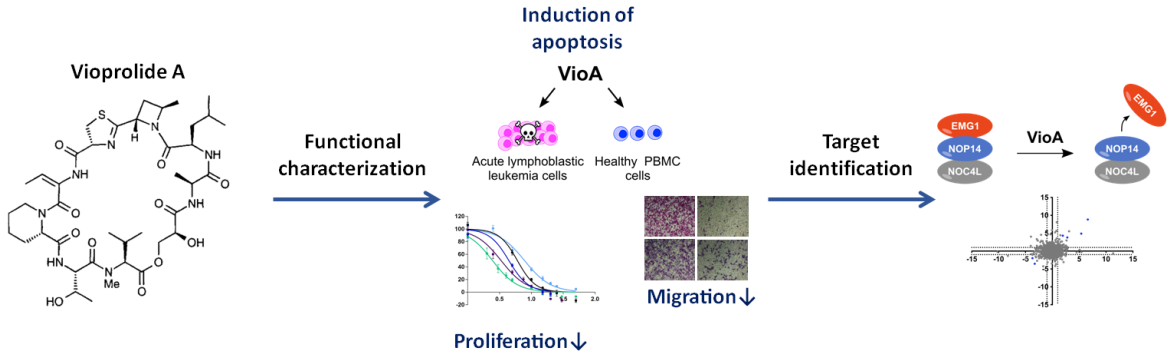

Fig. 25 Vioprolide A project summary.

4. Results Part II - Lagunamide A

4.1 Anticancer effects of Lagunamide A

4.1.1 Antiproliferative and apoptosis inducing effects of LagA

LagA exhibited strong growth inhibitory effects in the human pancreatic cell lines (BxPC3, Panc 03.27 and Panc 10.05) and the human cervical carcinoma cell line HeLa, with IC_{50} values in the nanomolar range (Figure 26A). As all tested cell types visibly showed cytotoxic phenotypes at higher concentrations, induction of apoptotic cell death was subsequently quantified. Incubation with LagA for 48h resulted in strong apoptosis induction in pancreatic and cervical carcinoma cells with EC_{50} values between 27.2 and 40.9nM (Figure 26B).

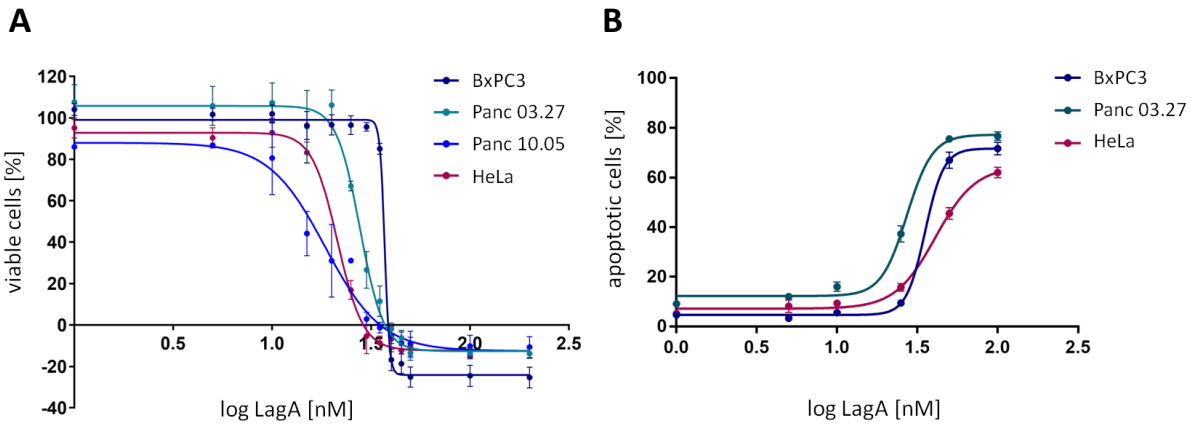

LagA	BxPC3	Panc 03.27	Panc 10.05	HeLa
IC50 [nM]	37.1 ± 0.5	27.8 ± 0.9	18.5 ± 1.4	21.4 ± 4.0

LagA	BxPC3	Panc 03.27	HeLa
EC50 [nM]	35.3 ± 1.9	27.2 ± 1.1	40.9 ± 2.2

Fig. 26 Evaluation of cytostatic and apoptosis inducing effects of LagA in pancreatic and cervical carcinoma cells. (**A**) Proliferative capacity of different cancer cell lines and corresponding IC_{50} values were determined by crystal violet staining after 72h. (**B**) Apoptotic effect of LagA on different cancer cell types. Percentage of apoptotic cells and respective EC_{50} values were determined by propidium iodide staining and flow cytometry after 48h. Results are presented as mean ± SEM of three independent experiments performed in triplicates.

4.1.2 Inhibition of migration

By using the RTCA xCELLigence system, the effect of LagA on tumor cell migration was investigated in BxPC3 and HeLa cells, respectively. This impedance-based method allows real-time monitoring of cells migrating through an 8µm porous membrane towards a chemoattractant. Representative curves are shown in Figure 27. The cell index, which is proportional to the number of migrating cells, is decreasing dose-dependently upon LagA treatment applied in subtoxic doses. Migration inhibition in both cell types was additionally quantified over a time-period of 16h as shown in corresponding bar diagrams.

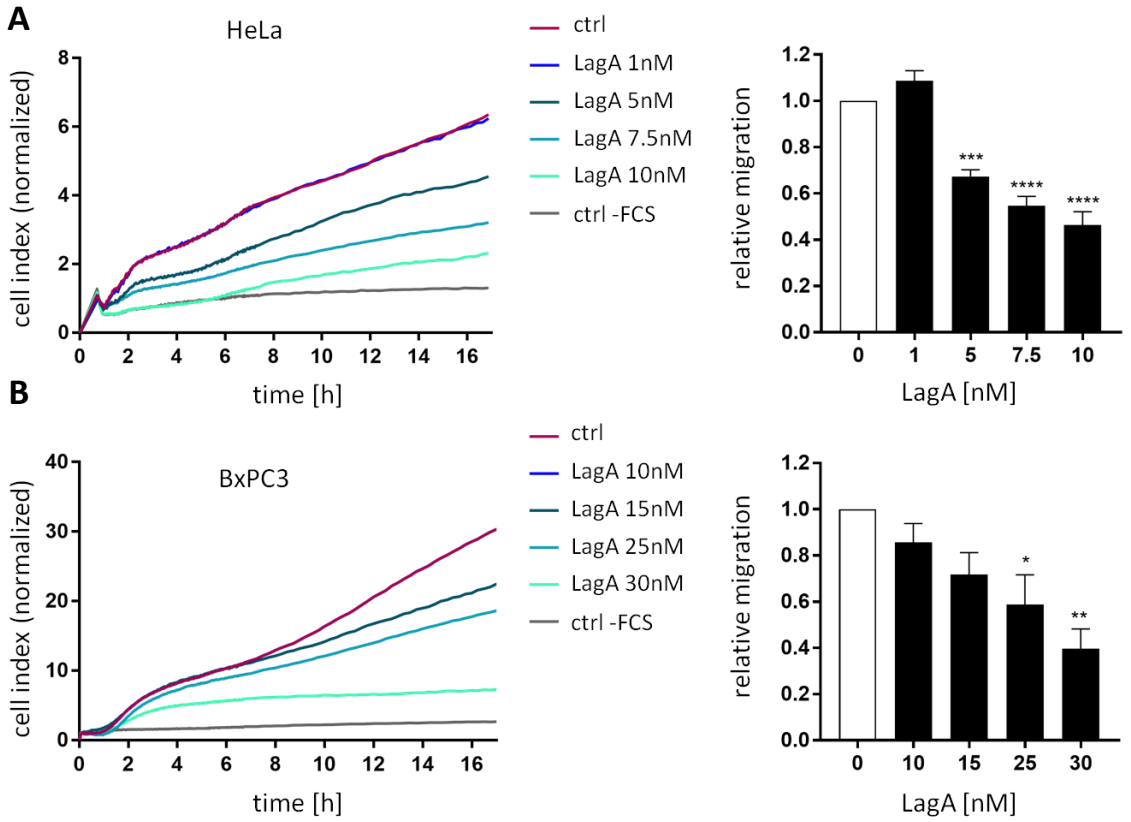

Fig. 27 Inhibitory effect of LagA on cancer cell migration. Real time monitoring of migration of (**A**) HeLa cells and (**B**) BxPC3 cells over 16h using the xCELLigence migration assay. Relative migration was calculated using RTCA software; representative curves out of three independent experiments are shown. Bars represent the mean ± SEM of three independent experiments performed in duplicates, one-way ANOVA, Dunnett's multiple comparisons test, * P<0.033, ** P<0.002, *** P<0.001, **** P<0.0001.

4.2 Effects of Lagunamide A on mitochondria

4.2.1 Lagunamide A alters mitochondrial morphology and dynamics

Based on the fact that LagA is structurally related to Aurilide, shown to target mitochondrial pathways (*70*), we focused on mitochondria for further functional characterization of LagA. To analyze mitochondrial morphology in response to LagA treatment, transmission electron microscopy (TEM) was performed by Dr. Sabine Schmitt and Carola Eberhagen in the laboratory of Prof. Dr. Hans Zischka (Helmholtz Centre Munich, Germany). As shown in Figure 28A, mitochondria of control cells are structurally intact and reveal a clearly recognizable cristae structure. In HeLa cells treated with 150nM LagA for 30 min, mitochondria show the same characteristics like control cells, but are in total slightly smaller. By contrast, 10nM LagA treatment for 24h resulted in significantly smaller mitochondria with an extremely condensed matrix. Of note, mitochondria are still undamaged, meaning that there is no swelling or rupture of the outer membrane detectable. Furthermore, mitochondrial cristae are still apparent, but extremely enlarged.

To further investigate mitochondrial fission and fusion dynamics in LagA treated cells, live cell imaging of HeLa cells was performed subsequently to MitoTracker® Green FM staining. As it is shown in Figure 28B, stimulation with LagA led to a significant impairment of mitochondrial dynamics accompanied by increased fission. To ensure that the applied conditions are subtoxic, cell death rates were measured in parallel by PI staining and flow cytometry (Figure 28C).

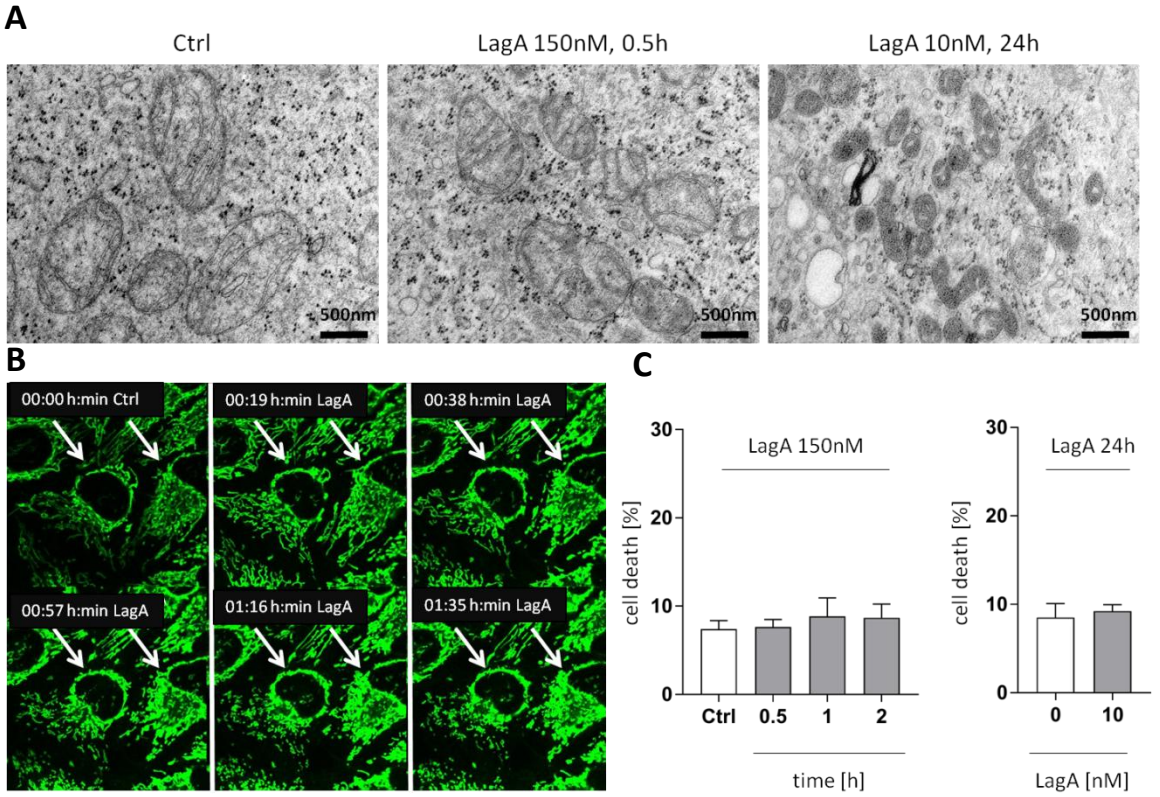

Fig. 28 Effects of LagA on mitochondrial morphology and dynamics in HeLa cells. (**A**) Transmission electron microscopy of HeLa cells treated with LagA as indicated. Electron microscopy was performed by Dr. Sabine Schmitt and Carola Eberhagen in the laboratory of Prof. Dr. Hans Zischka (Helmholtz Centre Munich, Germany). (**B**) Live cell imaging of HeLa cells subjected to 150nM LagA. Cells were stimulated with LagA at t = 18 min. Mitochondrial structures were visualized with MitoTracker® Green FM dye. (**C**) Applied concentrations are subtoxic. HeLa cells were treated with LagA as indicated and cell death quantification was conducted by propidium iodide staining and flow cytometry. (A, B) Representative images out of three independent experiments are shown. (C) Bars represent the mean ± SEM of three independent experiments performed in triplicates.

4.2.2 Mitochondrial mass decreases upon LagA treatment

As a further parameter of mitochondrial health, changes in mitochondrial mass of LagA treated cells were determined by MitoTracker® Green FM staining followed by flow cytometry. MitoTracker® Green FM is able to stain mitochondria in a manner that is independent of their membrane potential, consequently providing a readout relating solely to mitochondrial mass (*71*). As shown in Figure 29A, treatment with low doses of LagA for 24h led to reductions of mitochondrial mass levels. Interestingly, LagA 150nM treatment for 5-30 min resulted in noticeably decreased MitoTracker® Green fluorescence, indicating that LagA triggers a rapid and direct effect on mitochondria. Subsequently, expression levels of a key regulator of mitochondrial biogenesis, peroxisome proliferator-activated receptor-γ coactivator (PGC)-1α (*72*), in response to LagA treatment was investigated. PGC1α acts as a transcription factor coactivator, influencing a majority of cellular metabolic pathways and serving as a stress sensor in cancer cells in order to maintain metabolic homeostasis (*73*). However, LagA treatment did not alter expression levels of PGC1α, suggesting that this regulatory pathway is not addressed (Figure 29B).

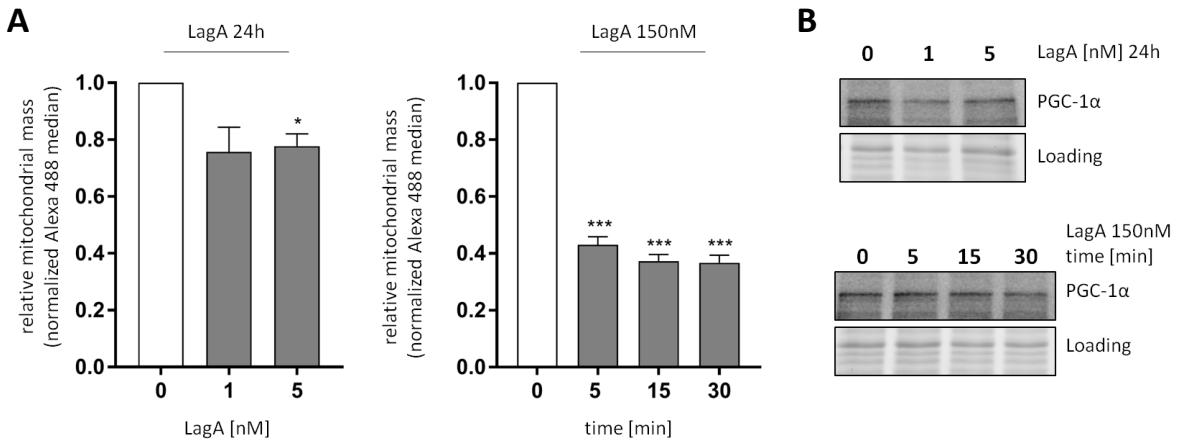

Fig. 29 Decrease of mitochondrial mass upon LagA treatment. (**A**) HeLa cells treated with LagA and subjected to MitoTracker® Green FM staining followed by flow cytometry. Bars represent the mean ± SEM of three independent experiments performed in triplicates, one-way ANOVA, Dunnett's test, * P<0.033, *** P<0.001. (**B**) Western blot analysis of HeLa cells treated with LagA and probed with anti-PGC1α antibody. Representative blots of three independent experiments are shown.

4.2.3 Effects on mitochondrial function and bioenergetics

Altered mitochondrial morphology and dynamics indicate that the potent anticancer properties of LagA might be derived from interference with mitochondrial activity. To further investigate the effect of LagA on mitochondrial function, we monitored cellular oxygen consumption rates (OCR) as measures of mitochondrial respiration using a Seahorse Extracellular Flux analyzer. In detail, the key parameters of mitochondrial function were determined by sequentially exposing cells to mitochondria perturbing reagents in the so called mitochondrial stress test (see section 2.11). After measuring basal respiration rates of HeLa cells pre-treated with subtoxic concentrations of LagA for 24h, oligomycin, FCCP and a combination of rotenone and antimycin A were consecutively added. Real-time measurements of OCR are shown in Figure 30A and respective quantifications are shown in Figures 30B-G. As presented in Figure 30A and B, basal respiration is diminished by treatment with 10 nM LagA, suggesting a decrease in oxidative phosphorylation. Next, the ATP synthase inhibitor oligomycin was added, which was used here to distinguish between ATP-linked respiration and oxygen consumption that is used to overcome the proton leak across the mitochondrial membrane. Subsequently, addition of FCCP uncoupled oxygen consumption from ATP production by disrupting the mitochondrial membrane potential and raised OCR to a maximum value. Maximal respiration was, like basal respiration, reduced upon LagA treatment (Figure 30C). These results are also consistent with decreases in ATP-linked respiration (Figure 30D). By the final injection of Antimycin A (AntA) and rotenone the electron transport chain was targeted, thereby reducing OCR to a minimum value. Spare respiratory capacity represents the reserve capacity of a cell to generate ATP via oxidative phosphorylation in case of an increased demand for energy. Interestingly, this bioenergetics capacity of mitochondria was not altered in LagA treated cells compared to control cells (Figure 30E). Overall, the substantial decrease in OCR upon LagA treatment suggests that the natural product targets a critical pathway for oxidative phosphorylation (OXPHOS). However, since the addition of oligomycin resulted in a further decrease of OCR, it appears that LagA either has an incomplete effect or that a modulatory pathway is targeted.

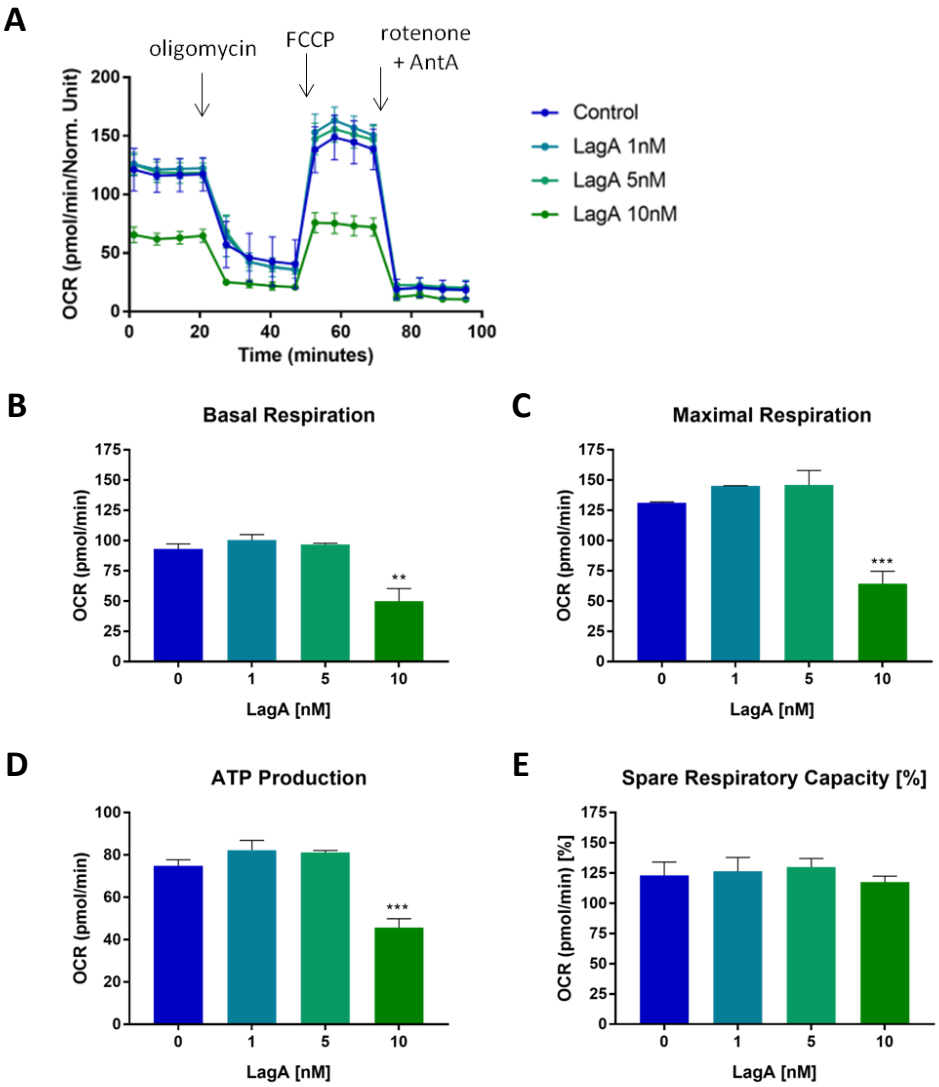

Fig. 30 Decrease in oxygen consumption rate (OCR) in LagA treated cells. Seahorse mito stress test was performed to measure OCR in LagA treated HeLa cells following the sequential addition of inhibitors of mitochondrial function: oligomycin, FCCP, and a combination of rotenone and antimycin A. (**A**) Real-time OCR profile plot, (**B**) basal respiration, (**C**) maximal respiration, (**D**) ATP production and (**E**) Spare respiratory capacity, calculated based on the difference between basal and maximal respiration. (A) Representative plot of three independent experiments is shown. (B-E) Bars represent the mean ± SEM of three independent experiments performed in triplicates, one-way ANOVA, Dunnett's multiple comparisons test, ** P<0.002, *** P<0.001.

4.2.4 Impact on mitochondrial apoptotic cell death

In addition to their role in cellular respiration, mitochondria play a key role in regulating apoptotic cell death. To provide insight into the mechanism of LagA induced cell death as shown in section 4.1.1 Figure 24B, critical markers of mitochondria-mediated apoptosis were investigated in different cell lines. Of note, LagA did not alter expression levels of the pro-apoptotic protein Bak, but markedly downregulated the expression levels of the antiapoptotic Bcl-2 family proteins Bcl-2, Bcl-xl and Mcl-1 in all testes cell types (Figure 31), providing evidence that LagA induces mitochondria mediated apoptosis.

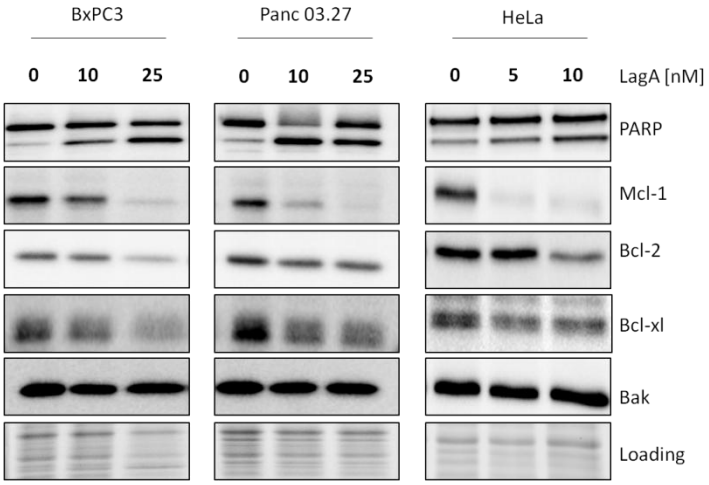

Fig. 31 Induction of apoptosis analyzed by immunoblotting. BxPC3, Panc 03.27 and HeLa cells were treated with LagA as indicated for 48h and protein levels of Mcl-1, Bcl-2, Bcl-xl and Bak, as well as PARP cleavage were determined. Representative blots of three independent experiments are shown.

4.3 Investigations on the molecular mechanism of action of Lagunamide A

4.3.1 Effects on key mitochondrial fission and fusion regulators

In view of the substantially altered mitochondrial dynamics and morphological changes in mitochondria of LagA treated cells, key players of mitochondrial fission and fusion were investigated, subsequently. Mitochondrial fusion is a complex sequential process, involving the integration of the outer mitochondrial membrane and the inner mitochondrial membrane (*49*). The main regulators of this process are the dynamin-related GTPase mitofusin 1 (Mfn-1), implicated in outer membrane fusion and optic atrophy 1 (OPA-1) that is anchored in the inner mitochondrial membrane (*49, 50*). Of note, LagA treatment of HeLa cells for 24h (Figure 32A) led to a significant decrease in endogenous levels of both OPA-1 and Mfn-1, being in line with the fragmented mitochondrial phenotype described in section 4.2.1. A slight decrease in Mfn-1 protein levels can also be observed in the high dose setting after 30 min. (Figure 30A) By contrast, LagA treatment did not alter Mfn-1 expression in the pancreatic cancer cell lines BxPC3 and Panc 03.27. Furthermore, regarding the OPA-1 protein, only long isoforms levels were found down-regulated after LagA treatment. Panc 03.27 cells are KRAS mutated and the oncogenic protein RAS was previously described to induce mitochondrial fission via phosphorylation of dynamin-related protein 1 (DRP1) at Ser616 (*52*). Taken this into consideration, the key mitochondrial fission regulator DRP1 was investigated in pancreatic cell lines by western blot analyses. Remarkably, LagA did neither alter DRP1 total levels nor the Ser616

phosphorylated form, which is implicated in mitochondrial fission. Conversely, phosphorylation of DRP1 at Ser637, which decreases GTPase activity and reduces mitochondrial fission, was found to be enhanced in LagA treated Panc 03.27 cells (Figure 32B). By contrast, DRP1 seems not to be addressed in LagA treated BxPC3 cells (Figure 32B). Overall, these data suggest a cell line dependent cellular response to LagA treatment and underscores the complexity of mitochondrial dynamics in the context of cancer.

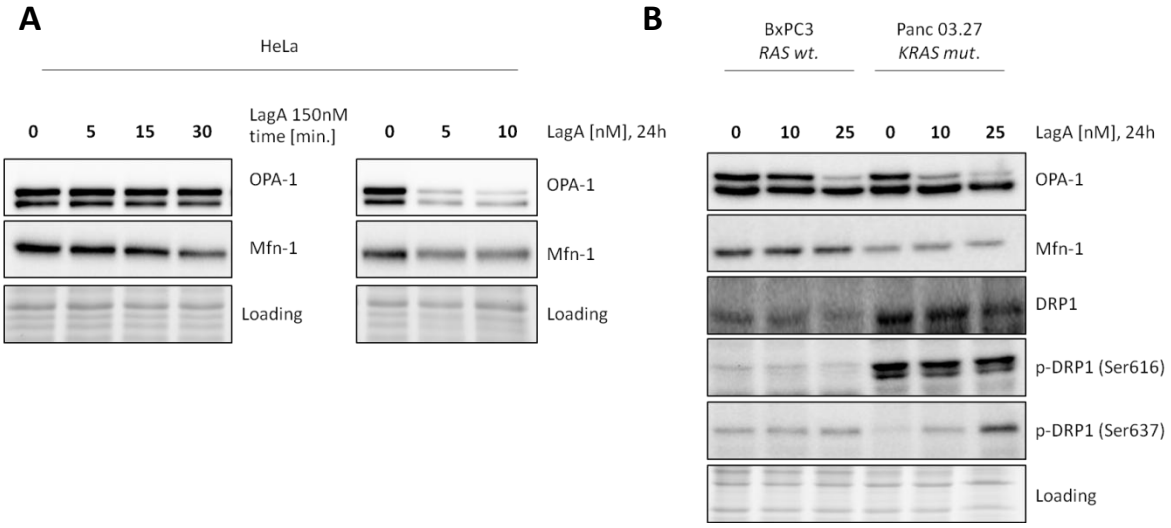

Fig. 32 Differential regulation of key mitochondrial fission and fusion markers in LagA treated cells. (**A**) HeLa cells treated with LagA and subjected to western blot analysis for OPA-1 and Mfn-1. (**B**) BxPC3 and Panc 03.27 cells treated with LagA and probed for OPA-1, Mfn-1, DRP1, p-DRP1 (Ser616) and p-DRP1 (Ser637) expression by western blot analysis. (A, B) Representative blots of three independent experiments are shown.

4.3.2 Lagunamide A and Aurilde do not share protein targets

Based on the fact that LagA and the marine cyclodepsipeptide Aurilide derived from *Dolabella auricularia* are very similar in structure (Figure 33A), we first hypothesized that their protein targets are identical. This was further encouraged by the fact that Aurilde as well as LagA exert potent cytotoxic effects and were shown to induce mitochondrial fragmentation and apoptosis (*74*). Sato *et al.* presented prohibitin 1 (Phb1) as molecular target of Aurilide and showed that binding to Phb1 disrupts the Phb1-spastic paraplegia 7 (SPG7) interactions. Furthermore, they could demonstrate that Aurilide accelerates the proteolytic processing of optic atrophy 1 (OPA1) long isoforms to short isoforms, resulting in mitochondria mediated apoptosis (*70*).

Consequently, to validate Phb1 as potential target of LagA, co-IP experiments of Phb1 were performed to investigate the Phb1-SPG7 interaction. In contrast to Aurilide, LagA

was not able to perturb SPG7 binding to Phb1, suggesting that Aurilide and LagA trigger their biological effects via different target proteins (Figure 33B).

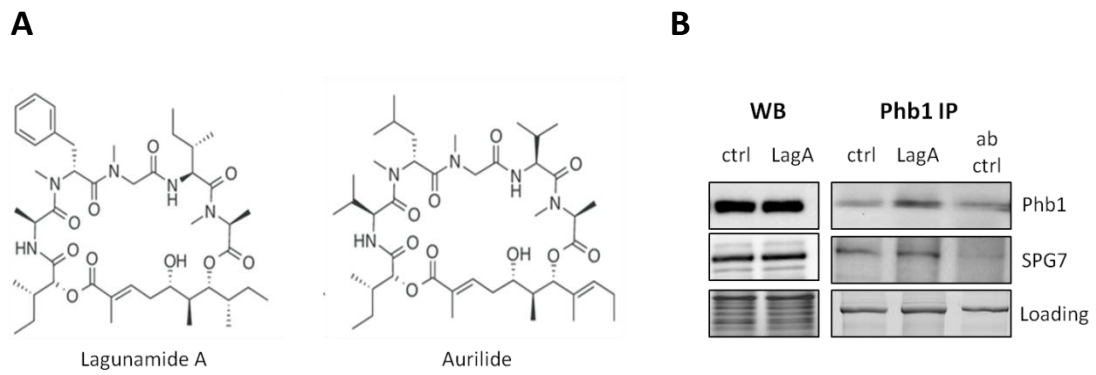

Fig. 33 Lagunamide A and Aurilide do not share Phb1 protein target. (**A**) Chemical structures of LagA and Aurilide. (**B**) Western blot analysis for Phb1 and SPG7 of HeLa cells treated with 10nM LagA for 24h (WB). Co-IP of Phb1 in HeLa cells and detection of Phb1 and interaction partner SPG7 by western blot analysis (Phb1 IP). One representative experiment out of three independent experiments is shown.

4.4 Summary

In summary, LagA, a highly complex marine natural product, showe potent growth inhibitory and antimigratory potential in different cancer cell lines at nanomolar concentrations. Antiproliferative effects were additionally accompanied by mitochondria mediated apoptotic cell death. Subsequent functional characterization revealed changes in mitochondrial morphology, dynamics and oxygen consumption rates within nanomolar concentrations of LagA (Figure 34). These findings indicate a mitochondria-perturbing mode of action of the natural product and emphasize the need to elucidate the molecular target(s) addressed by this interesting molecule. As mitochondria have emerged as a potential target for anticancer therapy in recent years, LagA represents a promising new compound with potentially important applications as both anticancer drug lead structure and molecular probe to explore mitochondrial biology in cancer.

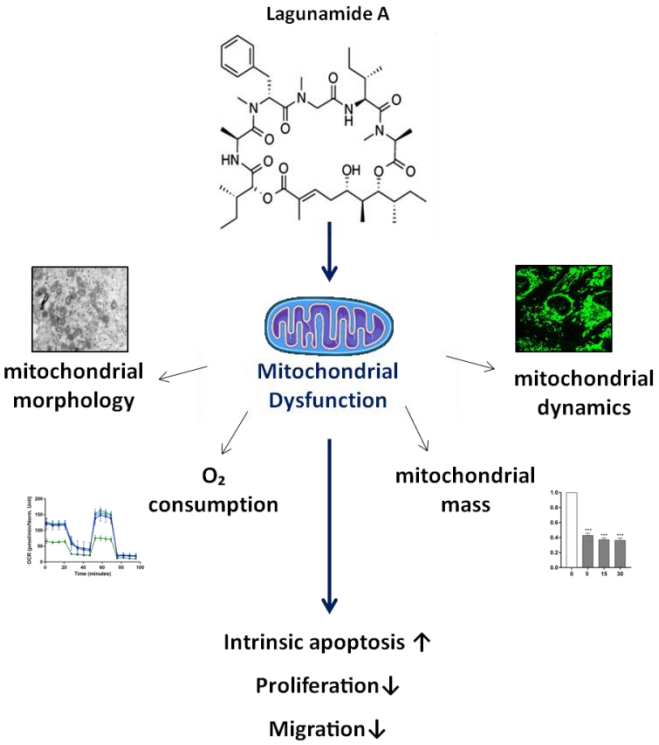

Fig. 34 Lagunamide A project summary.

5. Discussion Part I

5.1 Vioprolides as promising anticancer compounds

Since the Vioprolides were introduced by Schummer *et al.* in 1996, no in-depth functional characterization or detailed studies concerning their molecular mode of action have been reported up to date. Encouraged by the potent anticancer activity of Vioprolides, which was claimed in the initial publication, we performed detailed analyses of their antitumor activities. Interestingly, Vioprolide A (VioA), which only differs in N-heterocycles compared to the other family members, had much greater growth-inhibitory efficacy against the tested cancer cell line Jurkat. These findings suggest that the heterocycles may play a particular role in interaction with the cellular target(s) of interest.

Of note, VioA exhibited potent antiproliferative effects against a multitude of cancer cell types including leukemia, bladder cancer and cervical cancer. Additionally, VioA showed potent antimigratory potential and was effective in inhibiting invasion of T24 bladder carcinoma cells grown in three-dimensional culture. Furthermore, VioA demonstrated potent apoptosis inducing activity in various cancer cell lines with minimal effect in healthy PBMCs. This apoptosis inducing effect was particularly high in ALL cell lines and very importantly ALL patient derived xenograft cells of diverse background, highlighting a potential therapeutic relevance of VioA.

In conclusion, we reinforced the potent structure-dependent antitumor effects of the Vioprolides. Furthermore, we identified VioA as the most promising derivative of this interesting natural compound class for subsequent detailed investigations.

5.2 Targeting ribosome biogenesis as antitumor strategy

Ribosome biogenesis is an essential process in every growing cell. In eukaryotes, this process is highly orchestrated, including the synthesis and processing of pre-ribosomal RNAs, ribosomal protein synthesis and finally assembly and export of the ribosomes. Moreover, these steps require hundreds of assembly factors, most of which are essential (*75*). It is not surprising that ribosome biogenesis is of particular importance for fast proliferating cells, highlighting that its inhibition is a well-founded strategy for anticancer treatment. One major advantage of selective inhibition of ribosomal biogenesis, in contrast to most currently used DNA damaging anticancer drugs, is the non-genotoxic inhibition of rRNA production by selectively interfering with polymerase I (Pol I) mediated rDNA transcription. Very importantly, ribosome biogenesis inhibitors are less efficient in resting

cells due to the long half-life of cytoplasmatic ribosomes (*76*), providing a basis for selective anticancer targeting. While several inhibitors of rRNA transcription have been reported (*38, 39*) and a number of established therapeutic drugs were shown to inhibit ribosome biogenesis at this level (*37*), no compounds are available that directly target the ribosome biogenesis pathway downstream of transcription. Moreover, an expanding body of evidence displays that also ribosome assembly is regulated by oncogenic signalling pathways (*30*), highlighting that there is a large repertoire of potentially new and innovative anticancer drug targets, besides Pol I transcription inhibition.

5.2.1 NOP14 as novel druggable anticancer target

Within the framework of this thesis, we present the nucleolar protein 14 (NOP14) as novel druggable anticancer target. Thermal proteome profiling as target identification approach identified NOP14 as direct target of VioA. Interestingly, siRNA knockdown studies confirmed that NOP14 plays a role in tumor cell growth, substantiating that VioA triggers its potent antiproliferative effects via targeting NOP14. Of note, previous literature data showed that there is an association between NOP14 overexpression in pancreatic cancer and tumor cell invasion (*77, 78*), being additionally in line with the strong antimigratory and antiinvasive effects we observed upon VioA treatment. However, the apoptosis inducing effect of VioA could not be attributed to NOP14 in siRNA knockdown studies. It must be noted that, due to technical reasons, silencing experiments were performed in HeLa cells, which are less sensitive towards VioA induced apoptosis, anyway. Hence, NOP14 silencing experiments in cell types susceptible to VioA apoptosis induction, like the ALL cell lines Jurkat and CEM, will have to be done to provide a reasonable functional link between NOP14 and VioA induced apoptosis induction. In this context, also the high expression of NOP14 in ALL cell lines in contrast to healthy PBMCs is noteworthy. This finding suggests a putative correlation between NOP14 expression and susceptibility towards cell death induction and a clinical significance of NOP14. However, a substantial increase in the number of samples is needed to accurately evaluate whether NOP14 expression is significantly correlated with the development of acute lymphoblastic leukemia in future studies.

NOP14 plays a crucial role in ribosome biogenesis, more precisely the maturation of the 18S rRNA and assembly of the 40S subunit. In the yeast model, NOP14 was shown to interact with numerous proteins, essential for proper functional ribosome assembly machinery (*66, 69*). MS-based co-IP experiments identified a complex compilation of NOP14 interaction partners. Strikingly, we could identify NOC4L and EMG1 as prominent binding partners of NOP14 in human cells. The yeast homologues of both proteins were

shown to be essential NOP14 interacting proteins (*66, 69*). Of note, western blot based co-IP confirmed that VioA selectively impairs the interaction between NOP14 and EMG1, whereas the NOP14-NOC4L complex remained unperturbed. Liu *et al.* showed that the interaction of NOP14 and EMG1 is essential for proper 18S rRNA maturation and 40S ribosome biogenesis in yeast (*66*), further underlining that VioA interferes with ribosome biosynthesis. Noteworthy, a single base mutation in EMG1 causes the highly lethal autosomal recessive disorder Bowen-Conradi syndrome, which is common in the Hutterite population (*79, 80*). Studies of Armistead *et al.* showed that this EMG1 mutation leads to an 18S rRNA processing delay, substantiating that the EMG1 function is conserved in yeast and human cells. More remarkably, they showed that proper levels of EMG1 are more critical in rapidly proliferating cells, such as lymphoblasts, than slower-growing cells like fibroblasts (*81*). These facts underscore the great potential of targeting the NOP14-EMG1 complex, and thereby ribosome assembly as a selective approach in fast growing cells, such as in cancer.

In summary, NOP14 was confirmed as promising therapeutic target for cancer treatment. Moreover, the identification of VioA as potent inhibitor of the NOP14-EMG1 interaction opens the door to explore upstream and downstream processes in depth. This could potentially provide additional therapeutic strategies for cancer patients and stimulate basic research in the topic ribosome assembly and cancer.

5.2.2 Vioprolide A as the first compound targeting the ribosome assembly pathway

The discovery of VioA as an inhibitor of the NOP14 dependent ribosome processing pathway substantiates the assumption that targeting the ribosome biogenesis pathway downstream of rDNA transcription is a promising anticancer strategy. Strikingly, VioA inhibited de novo rRNA synthesis, a crucial step in ribosome biogenesis. But, importantly, this effect was not accompanied by nucleolar disruption, which can be observed in cells treated with agents interfering with Pol I transcription, like ActD or Doxorubicin (*35*). These findings further confirm that VioA targets ribosome biogenesis via a unique mechanism. Production of ribosomes and protein synthesis are crucial processes for every growing cell, being in line with the antiproliferative effect of VioA. Furthermore, a proper functioning ribosome biosynthesis is necessary for cell cycle progression. Hence, the achievement of a sufficient ribosome amount during G1 phase, allows cells to overcome the G1-S restriction point (*82*). In accordance with these facts, VioA treatment led to a significant decrease of cells in S-phase and an increase of cells resting in G1. At higher VioA concentrations, cell cycle arrest was accompanied by induction of apoptotic cell death.

Interestingly, the extent of VioA exhibited apoptosis was cell-type specific, with ALL cells being the most sensitive candidates. Of note, Scala *et al*. also linked the inhibition of ribosome biogenesis to induction of apoptotic cell death. However, it was stated that only cancer cells with a high ribosomal biogenesis rate and thus dependence on this pathway are susceptible for apoptosis induction (*83*). In consequence, further investigations on differential ribosome biogenesis rates in cancer cells are needed to connect these findings with the sensitivity of ALL cells towards VioA.

5.3 Future perspectives: Vioprolide A as chemical tool in human ribosome biogenesis and beyond

The process of ribosome biogenesis has only been extensively studied in unicellular organisms, best described in the model organism *Saccharomyces cerevisiae.* While basic features of this pathway and many ribosomal proteins are conserved among eukaryotes, the human ribosome biogenesis pathway is considerably more complex due to increased size of human ribosomes, and a more complex regulatory network that modulates ribosome assembly and function (*84*). But, the high importance of uncovering the detailed ribosome assembly pathway in humans is emphasized by the fact that there is a growing number of ribosomopathies, caused by mutations in genes encoding ribosomal proteins or ribosome biogenesis factors (*85, 86*). Moreover, it has been shown that syndromes like Diamond-Blackfan anaemia, involving mutant ribosomal or nucleolar proteins are associated with an increased risk of cancer (*87, 88*).

Additionally, ribosome biogenesis is tightly linked with numerous other pathways, like translational regulation. Translation itself has long been considered as housekeeping function. However, recent studies suggest that ribosomes also function as regulatory elements in translation (*89*). Mills and Green proposed that changes in cellular ribosome abundance may be a major driver of changes in translation of mRNA. In detail, ribosomes have different affinities for mRNAs. Hence, low-affinity mRNAs cannot compete with high-affinity mRNAs when ribosomes are limited (*86*). These implications may also play a critical role in cancer, as altered ribosomal activity and selection of specific cancer-associated mRNAs for translation have already been described (*90, 91*).

Therefore, identification of novel factors involved in ribosome biogenesis and the investigation of the exact mechanisms by which such proteins alter tumor susceptibility is crucial. This highlights the need to establish inhibitors of the ribosome assembly pathway

to identify such key players and their regulatory network - not only to provide new strategies against related diseases, like cancer.

With VioA targeting the NOP14-EMG1 complex, we discovered a new druggable step of the highly complex human ribosome assembly pathway. By introducing the molecular mode of action of VioA, a promising starting point is set to study this essential and disease-related pathway in depth by chemical inhibition.

6. Discussion Part II

6.1 Targeting mitochondria as powerful approach in cancer therapy

In recent years, mitochondria have emerged as potential anticancer targets as cancer cell mitochondria are structurally and functionally different from their non-cancerous counterparts (*92*). In this line, it is now recognized that the mitochondrial dynamics not only enable cells to meet metabolic requirements, but emerged as regulators of tumor growth, providing a basis for tumor targeting. In the context of this thesis, the marine natural compound Lagunamide A (LagA) was characterized as mitochondria-perturbing agent with striking effects on mitochondrial dynamics.

6.1.1 Lagunamide A as an anticancer drug targeting mitochondrial dynamics

Mitochondria are extremely dynamic organelles that constantly fuse and divide. Under physiological conditions, the mitochondrial network undergoes moderate fission and fusion, in order to fill the requirements for cellular metabolism (*50*). Mild levels of mitochondrial fission facilitate the autophagic clearance of mitochondria, whereas moderate levels of mitochondrial fusion provides the energy for communication between the mitochondrial networks (*49*). Moreover, previous studies have identified mitochondrial fission as the apoptotic trigger in various disease models (*93, 94*) . Thereby, mitochondrial fission has been acknowledged as a potential target to reduce the proliferation, migration and survival of cancer cells (*95*). Interestingly, mitochondria of LagA treated cells manifested obvious morphological changes from the normal fused to a fragmented shape. In accordance with previous findings, LagA had a striking impact on tumor cell proliferation, migration and induction of apoptotic cell death. The fragmented mitochondrial phenotype was furthermore accompanied by downregulation of the key mitochondrial fusion regulators, optic atrophy 1 (OPA-1) and mitofusin-1 (Mfn1), indicating a disruption of the mitochondrial fusion machinery by LagA. The fusion protein OPA-1 also regulates the formation of mitochondrial cristae, reflecting the enlarged cristae structure observed in mitochondria of LagA treated cells. These results provide evidence that LagA triggers its potent anticancer effects via induction of mitochondrial fission.

Furthermore, mitochondrial dynamics are tightly linked to cellular metabolism. Cells lacking Mfn-1 and exhibiting a fragmented phenotype are associated with reduced mitochondrial respiration (*96*). Furthermore, OPA-1 deficient cells were shown to decrease oxidative phosphorylation (OXPHOS) (*97, 98*). In line with these previous studies, we observed a significant decrease of oxygen consumption rates (OCR) in LagA

treated HeLa cells, being consistent with a mitochondria-perturbing mode of action. Furthermore, the substantial decrease of basal respiration in LagA treated cells suggests that the natural product targets a pathway that is critical for oxidative phosphorylation. However, since the addition of Oligomycin, an ATP synthase inhibitor, generated a further decrease in OCR, it appears that LagA either has an incomplete effect or that a modulatory pathway is targeted. Additionally, FCCP, which uncouples oxygen consumption from ATP production, thereby raising OCR to a maximal value, caused an increase in OCR as well in LagA treated cells. Consistently, the spare respiratory capacity (the difference between basal and maximal respiration) remained constant upon LagA treatment. These findings further suggest that LagA does not directly target a protein that is necessary for the electron transport chain, as known inhibitors like Rotenone and Antimycin A produce a decrease in OCR that cannot be rescued by FCCP addition (*99*). Summarizing, these results indicate that LagA targets a component of a regulatory pathway of cellular metabolism, which could again be linked to mitochondrial dynamics.

Moreover, altered mitochondrial dynamics also represent a key feature of KRAS dependent cellular transformation. Thereby, oncogenic KRAS stimulates mitochondrial fragmentation via ERK1/2 mediated phosphorylation of dynamin-related protein 1 (DRP1). Of note, fission is essential for RAS-driven tumor growth and along this line mitochondrial fission inhibition is discussed as a therapeutic approach for cancer treatment (*52*). These findings display that enhancing mitochondrial fission cannot uniformly be designated as anticancer strategy. For this reason, we additionally probed the effects of LagA on KRAS mutated (Panc 03.27 and Panc 10.05) and RAS-driven (BxPC3) pancreatic cancer cell lines, in order to transfer the LagA effects to another cellular model. Of note, LagA was able to inhibit cell growth and induce apoptosis in pancreatic cell types, with IC_{50} and EC_{50} levels in the nanomolar range, similar to HeLa cells. This provides evidence that the cytotoxic effect of LagA is independent from the state of mitochondrial dynamics in cells. Regarding the molecular machinery of mitochondrial dynamics, LagA treatment did not deregulate the mitochondrial fusion protein Mfn-1, as it was shown in HeLa cells. Given the fact that KRAS- driven tumors rely on DRP1, we additionally investigated this mitochondrial fission regulator. However, LagA did not induce any alterations in the total form, but enhanced the phosphorylation at Ser637 selectively in the KRAS mutated cell line Panc 03.27. As this phosphorylation is linked to inhibition of fission, this most likely represents a feedback mechanism in response to LagA. Furthermore, only the long isoform of OPA-1 (L-OPA-1) decreased in pancreatic cell lines, whereas the protein levels of the short isoform (S-OPA-1) remained stable. Of note, the L-OPA-1 proteolytic cleavage is an important mechanism that regulates mitochondrial fission and fusion. Balanced formation of L- and S-OPA-1 preserves a tubular network of mitochondria.

Different stimuli can induce the cleavage of L-OPA-1, causing the accumulation of S-OPA-1, which accelerates mitochondrial network fragmentation (*100, 101*). The reduction of L-OPA-1 in LagA treated cells can be attributed to the observed fragmented mitochondrial phenotype. However, these data also reveal that none of the investigated fission / fusion regulators is affected directly by LagA, but suggest that a protein that is critical for mitochondrial dynamics is targeted.

In summary, promoting mitochondrial fragmentation can be considered as anticancer strategy, highlighting LagA as a promising drug lead. Moreover, the differential effects of LagA on the molecular machinery of mitochondrial dynamics in different cell types highlight the complexity of this pathway. Importantly, these findings emphasize the need to characterize the exact molecular mode of action of LagA in order to use the natural product as molecular probe to investigate this cancer related pathway.

6.1.2 Potential of Lagunamide A to trigger apoptotic cell death

Mitochondria play a pivotal role in apoptotic cell death signaling. The mitochondrial outer membrane permeabilization (MOMP) of mitochondria during apoptosis results in cytochrome C release and activation of downstream caspases that execute apoptosis (*102*). MOMP is controlled by members of the Bcl-2 family of proteins. In this context, resistance to apoptotic stimuli and overexpression of anti-apoptotic Bcl-2 proteins are commonly seen characteristics in cancer (*48*). Of note, LagA markedly downregulated the anti-apoptotic Bcl-2 family members Bcl-2, Bcl-xl and Mcl-1 in different cancer cell lines and induced apoptotic cell death at nanomolar concentrations in all tested cell lines. Another protein that is crucial for mitochondrial apoptosis regulation is OPA-1. As key regulator of the mitochondrial cristae shape, OPA-1 plays a role in the process of cristae remodeling during apoptosis (*103*). Cristae remodeling is required to mobilize cytochrome c from the cristae space to the intermembrane space, where it is released across the outer mitochondrial membrane upon permeabilization (*47*). Sato *et al*. showed that the natural compound Aurilide induces apoptotic cell death by targeting the OPA-1 dependent cristae remodeling and thereby substantiated the key role of OPA-1 in apoptosis regulation (*70*). Of note, the OPA-1 protein is also deregulated upon LagA treatment and more strikingly, mitochondrial cristae were found to be extremely enlarged in LagA treated cells. Keeping this in mind, it is likely that the OPA-1 dependent cristae remodeling may also contribute to LagA induced mitochondrial apoptosis.

Very importantly, small molecules like LagA that can selectively target mitochondria and activate the apoptotic cascade represent a directed approach in cancer therapy. Commonly used anticancer drugs mostly target signalling events upstream of the mitochondrial cell death machinery, for example by stabilizing p53. Such upstream pathways are often deregulated in human cancer, which in consequence often become resistant to conventional therapeutics (*104, 105*). Hence, compounds like LagA that directly target mitochondria may circumvent such resistance mechanisms and develop into promising treatment options for resistant forms of cancer.

7. References

1. D. J. Newman, G. M. Cragg, Natural Products as Sources of New Drugs from 1981 to 2014. *Journal of natural products* **79**, 629-661 (2016).
2. N. Widmer *et al.*, Review of therapeutic drug monitoring of anticancer drugs part two--targeted therapies. *European journal of cancer (Oxford, England : 1990)* **50**, 2020-2036 (2014).
3. F. E. Koehn, G. T. Carter, The evolving role of natural products in drug discovery. *Nat Rev Drug Discov* **4**, 206-220 (2005).
4. T. Rodrigues, D. Reker, P. Schneider, G. Schneider, Counting on natural products for drug design. *Nat Chem* **8**, 531-541 (2016).
5. J. Herrmann, A. A. Fayad, R. Muller, Natural products from myxobacteria: novel metabolites and bioactivities. *Nat Prod Rep* **34**, 135-160 (2017).
6. W. Dawid, Biology and global distribution of myxobacteria in soils. *FEMS Microbiology Reviews* **24**, 403-427 (2000).
7. J. Muñoz-Dorado, F. J. Marcos-Torres, E. García-Bravo, A. Moraleda-Muñoz, J. Pérez, Myxobacteria: Moving, Killing, Feeding, and Surviving Together. *Frontiers in Microbiology* **7**, (2016).
8. J. Diez *et al.*, Myxobacteria: natural pharmaceutical factories. *Microb Cell Fact* **11**, 52 (2012).
9. S. C. Wenzel, R. Müller, Myxobacteria—'microbial factories' for the production of bioactive secondary metabolites. *Molecular BioSystems* **5**, 567-574 (2009).
10. A. R. Tan, D. L. Toppmeyer, Ixabepilone in metastatic breast cancer: complement or alternative to taxanes? *Clin Cancer Res* **14**, 6725-6729 (2008).
11. T. F. Molinski, D. S. Dalisay, S. L. Lievens, J. P. Saludes, Drug development from marine natural products. *Nat Rev Drug Discov* **8**, 69-85 (2009).
12. P. C. Jimenez, D. V. Wilke, L. V. Costa-Lotufo, Marine drugs for cancer: surfacing biotechnological innovations from the oceans. *Clinics (Sao Paulo, Brazil)* **73**, e482s (2018).
13. P. D. Senter, E. L. Sievers, The discovery and development of brentuximab vedotin for use in relapsed Hodgkin lymphoma and systemic anaplastic large cell lymphoma. *Nat Biotechnol* **30**, 631-637 (2012).
14. I. Sainis *et al.*, Cyanobacterial cyclopeptides as lead compounds to novel targeted cancer drugs. *Marine drugs* **8**, 629-657 (2010).

15. L. A. Salvador-Reyes, H. Luesch, Biological targets and mechanisms of action of natural products from marine cyanobacteria. *Nat Prod Rep* **32**, 478-503 (2015).
16. D. Schummer *et al.*, Antibiotics from gliding bacteria, LXXVI. Vioprolides: new antifungal and cytotoxic peptolides from Cystobacter violaceus. *Liebigs Annalen* **1996**, 971-978 (1996).
17. D. Chauhan *et al.*, BAX/BAK-Induced Apoptosis Results in Caspase-8-Dependent IL-1β Maturation in Macrophages. *Cell Reports* **25**, 2354-2368.e2355 (2018).
18. F. Yan, R. Muller, Class I Methyltransferase VioH Catalyzes Unusual S-Adenosyl-l-methionine Cyclization Leading to 4-Methylazetidinecarboxylic Acid Formation during Vioprolide Biosynthesis. *ACS Chem Biol* **14**, 99-105 (2019).
19. D. Auerbach, F. Yan, Y. Zhang, R. Muller, Characterization of an Unusual Glycerate Esterification Process in Vioprolide Biosynthesis. *ACS Chem Biol* **13**, 3123-3130 (2018).
20. A. Tripathi, J. Puddick, M. R. Prinsep, M. Rottmann, L. T. Tan, Lagunamides A and B: cytotoxic and antimalarial cyclodepsipeptides from the marine cyanobacterium Lyngbya majuscula. *Journal of natural products* **73**, 1810-1814 (2010).
21. A. Tripathi, W. Fang, D. T. Leong, L. T. Tan, Biochemical studies of the lagunamides, potent cytotoxic cyclic depsipeptides from the marine cyanobacterium Lyngbya majuscula. *Marine drugs* **10**, 1126-1137 (2012).
22. X. Huang *et al.*, Structure Determinants of Lagunamide A for Anticancer Activity and Its Molecular Mechanism of Mitochondrial Apoptosis. *Molecular pharmaceutics* **13**, 3756-3763 (2016).
23. R. Wagner, Einige bemerkungen und fragen über das keimbläschen (vesicular germinativa). *Müller's Archiv Anat Physiol Wissenschaft Med* **268**, 373-377 (1835).
24. G. Valentin, *Repertorium für anatomie und physiologie*. (1837).
25. T. Pederson, The nucleolus. *Cold Spring Harb Perspect Biol* **3**, (2011).
26. N. Hein, K. M. Hannan, A. J. George, E. Sanij, R. D. Hannan, The nucleolus: an emerging target for cancer therapy. *Trends Mol Med* **19**, 643-654 (2013).
27. J. Heix *et al.*, Mitotic silencing of human rRNA synthesis: inactivation of the promoter selectivity factor SL1 by cdc2/cyclin B-mediated phosphorylation. *EMBO J* **17**, 7373-7381 (1998).
28. F. M. Boisvert, S. van Koningsbruggen, J. Navascues, A. I. Lamond, The multifunctional nucleolus. *Nat Rev Mol Cell Biol* **8**, 574-585 (2007).

29. E. Thomson, S. Ferreira-Cerca, E. Hurt, Eukaryotic ribosome biogenesis at a glance. *Journal of Cell Science* **126**, 4815-4821 (2013).
30. J. Pelletier, G. Thomas, S. Volarević, Ribosome biogenesis in cancer: new players and therapeutic avenues. *Nature Reviews Cancer* **18**, 51 (2017).
31. D. Hanahan, R. A. Weinberg, Hallmarks of cancer: the next generation. *Cell* **144**, 646-674 (2011).
32. R. J. White, RNA polymerases I and III, growth control and cancer. *Nature Reviews Molecular Cell Biology* **6**, 69-78 (2005).
33. A. Pich, L. Chiusa, E. Margaria, Prognostic relevance of AgNORs in tumor pathology. *Micron* **31**, 133-141 (2000).
34. S. Chedin *et al.*, Is ribosome synthesis controlled by pol I transcription? *Cell cycle (Georgetown, Tex.)* **6**, 11-15 (2007).
35. D. Drygin, W. G. Rice, I. Grummt, The RNA Polymerase I Transcription Machinery: An Emerging Target for the Treatment of Cancer. *Annual Review of Pharmacology and Toxicology* **50**, 131-156 (2010).
36. E. Brighenti, D. Trere, M. Derenzini, Targeted cancer therapy with ribosome biogenesis inhibitors: a real possibility? *Oncotarget* **6**, 38617-38627 (2015).
37. K. Burger *et al.*, Chemotherapeutic drugs inhibit ribosome biogenesis at various levels. *J Biol Chem* **285**, 12416-12425 (2010).
38. D. Drygin *et al.*, Anticancer activity of CX-3543: a direct inhibitor of rRNA biogenesis. *Cancer Res* **69**, 7653-7661 (2009).
39. D. Drygin *et al.*, Targeting RNA polymerase I with an oral small molecule CX-5461 inhibits ribosomal RNA synthesis and solid tumor growth. *Cancer Res* **71**, 1418-1430 (2011).
40. A. Khot *et al.*, First-in-Human RNA Polymerase I Transcription Inhibitor CX-5461 in Patients with Advanced Hematological Cancers: Results of a Phase I Dose Escalation Study. *Cancer Discovery*, CD-18-1455 (2019).
41. N. Lane, W. Martin, The energetics of genome complexity. *Nature* **467**, 929-934 (2010).
42. S. Vyas, E. Zaganjor, M. C. Haigis, Mitochondria and Cancer. *Cell* **166**, 555-566 (2016).
43. O. Warburg, Über den stoffwechsel der carcinomzelle. *Naturwissenschaften* **12**, 1131-1137 (1924).
44. G. Kroemer, J. Pouyssegur, Tumor cell metabolism: cancer's Achilles' heel. *Cancer Cell* **13**, 472-482 (2008).
45. D. Hanahan, R. A. Weinberg, The hallmarks of cancer. *Cell* **100**, 57-70 (2000).

46. M. Wasilewski, L. Scorrano, The changing shape of mitochondrial apoptosis. *Trends Endocrinol Metab* **20**, 287-294 (2009).
47. R. Yamaguchi *et al.*, Opa1-mediated cristae opening is Bax/Bak and BH3 dependent, required for apoptosis, and independent of Bak oligomerization. *Mol Cell* **31**, 557-569 (2008).
48. P. J. Burke, Mitochondria, Bioenergetics and Apoptosis in Cancer. *Trends Cancer* **3**, 857-870 (2017).
49. T. Wai, T. Langer, Mitochondrial Dynamics and Metabolic Regulation. *Trends Endocrinol Metab* **27**, 105-117 (2016).
50. P. Mishra, D. C. Chan, Metabolic regulation of mitochondrial dynamics. *J Cell Biol* **212**, 379-387 (2016).
51. D. Senft, Z. A. Ronai, Adaptive Stress Responses During Tumor Metastasis and Dormancy. *Trends Cancer* **2**, 429-442 (2016).
52. J. A. Kashatus *et al.*, Erk2 phosphorylation of Drp1 promotes mitochondrial fission and MAPK-driven tumor growth. *Mol Cell* **57**, 537-551 (2015).
53. B. von Eyss *et al.*, A MYC-Driven Change in Mitochondrial Dynamics Limits YAP/TAZ Function in Mammary Epithelial Cells and Breast Cancer. *Cancer Cell* **28**, 743-757 (2015).
54. B. Vick *et al.*, An advanced preclinical mouse model for acute myeloid leukemia using patients' cells of various genetic subgroups and in vivo bioluminescence imaging. *PLoS One* **10**, e0120925 (2015).
55. S. Ebinger *et al.*, Characterization of Rare, Dormant, and Therapy-Resistant Cells in Acute Lymphoblastic Leukemia. *Cancer Cell* **30**, 849-862 (2016).
56. F. Koczian *et al.*, Targeting the endoplasmic reticulum-mitochondria interface sensitizes leukemia cells to cytostatics. *Haematologica* **104**, 546-555 (2019).
57. M. Vinci, C. Box, S. A. Eccles, Three-dimensional (3D) tumor spheroid invasion assay. *J Vis Exp*, e52686 (2015).
58. I. Nicoletti, G. Migliorati, M. C. Pagliacci, F. Grignani, C. Riccardi, A rapid and simple method for measuring thymocyte apoptosis by propidium iodide staining and flow cytometry. *J Immunol Methods* **139**, 271-279 (1991).
59. C. Riccardi, I. Nicoletti, Analysis of apoptosis by propidium iodide staining and flow cytometry. *Nat Protoc* **1**, 1458-1461 (2006).
60. H. Franken *et al.*, Thermal proteome profiling for unbiased identification of direct and indirect drug targets using multiplexed quantitative mass spectrometry. *Nat Protoc* **10**, 1567-1593 (2015).
61. O. Kepp, L. Galluzzi, M. Lipinski, J. Yuan, G. Kroemer, Cell death assays for drug discovery. *Nat Rev Drug Discov* **10**, 221-237 (2011).

62. L. Galluzzi *et al.*, Molecular mechanisms of cell death: recommendations of the Nomenclature Committee on Cell Death 2018. *Cell Death & Differentiation* **25**, 486-541 (2018).
63. J. Chang, Y. Kim, H. J. Kwon, Advances in identification and validation of protein targets of natural products without chemical modification. *Nat Prod Rep* **33**, 719-730 (2016).
64. R. Jafari *et al.*, The cellular thermal shift assay for evaluating drug target interactions in cells. *Nat Protoc* **9**, 2100-2122 (2014).
65. M. M. Savitski *et al.*, Tracking cancer drugs in living cells by thermal profiling of the proteome. *Science* **346**, 1255784 (2014).
66. P. C. Liu, D. J. Thiele, Novel stress-responsive genes EMG1 and NOP14 encode conserved, interacting proteins required for 40S ribosome biogenesis. *Mol Biol Cell* **12**, 3644-3657 (2001).
67. J. Barandun *et al.*, The complete structure of the small-subunit processome. *Nature Structural &Amp; Molecular Biology* **24**, 944 (2017).
68. A. Fux, V. S. Korotkov, M. Schneider, I. Antes, S. A. Sieber, Chemical Cross-Linking Enables Drafting ClpXP Proximity Maps and Taking Snapshots of In Situ Interaction Networks. *Cell Chem Biol* **26**, 48-59 e47 (2019).
69. H. Kuhn *et al.*, The Noc-domain containing C-terminus of Noc4p mediates both formation of the Noc4p-Nop14p submodule and its incorporation into the SSU processome. *PLoS One* **4**, e8370 (2009).
70. S. Sato *et al.*, Marine natural product aurilide activates the OPA1-mediated apoptosis by binding to prohibitin. *Chem Biol* **18**, 131-139 (2011).
71. D. Puleston, Detection of Mitochondrial Mass, Damage, and Reactive Oxygen Species by Flow Cytometry. *Cold Spring Harb Protoc* **2015**, pdb prot086298 (2015).
72. H. Liang, W. F. Ward, PGC-1α: a key regulator of energy metabolism. *Advances in Physiology Education* **30**, 145-151 (2006).
73. Z. Tan *et al.*, The Role of PGC1α in Cancer Metabolism and its Therapeutic Implications. *Molecular Cancer Therapeutics* **15**, 774-782 (2016).
74. M. Semenzato, S. Cogliati, L. Scorrano, Prohibitin(g) cancer: aurilide and killing by Opa1-dependent cristae remodeling. *Chem Biol* **18**, 8-9 (2011).
75. J. R. Warner, The economics of ribosome biosynthesis in yeast. *Trends Biochem Sci* **24**, 437-440 (1999).
76. M. Penzo, L. Montanaro, D. Trere, M. Derenzini, The Ribosome Biogenesis-Cancer Connection. *Cells* **8**, (2019).

77. Y. Du *et al.*, Pancreatic Cancer Progression Relies upon Mutant p53-Induced Oncogenic Signaling Mediated by NOP14. *Cancer Res* **77**, 2661-2673 (2017).
78. B. Zhou, Q. Wu, G. Chen, T. P. Zhang, Y. P. Zhao, NOP14 promotes proliferation and metastasis of pancreatic cancer cells. *Cancer Lett* **322**, 195-203 (2012).
79. N. Torbert *et al.*, Bowen-Conradi Syndrome: a trisomy 18-like autosomal recessive disorder common in Hutterites. *S D Med* **68**, 65-67, 69 (2015).
80. R. A. De Souza, Mystery behind Bowen-Conradi syndrome solved: a novel ribosome biogenesis defect. *Clin Genet* **77**, 116-118 (2010).
81. J. Armistead *et al.*, Growth arrest in the ribosomopathy, Bowen-Conradi syndrome, is due to dramatically reduced cell proliferation and a defect in mitotic progression. *Biochim Biophys Acta* **1852**, 1029-1037 (2015).
82. M. Derenzini, G. Pasquinelli, M. F. O'Donohue, D. Ploton, M. Thiry, Structural and functional organization of ribosomal genes within the mammalian cell nucleolus. *J Histochem Cytochem* **54**, 131-145 (2006).
83. F. Scala *et al.*, Direct relationship between the level of p53 stabilization induced by rRNA synthesis-inhibiting drugs and the cell ribosome biogenesis rate. *Oncogene* **35**, 977 (2015).
84. K. E. Bohnsack, M. T. Bohnsack, Uncovering the assembly pathway of human ribosomes and its emerging links to disease. *The EMBO Journal* **38**, e100278 (2019).
85. P. Calamita, G. Gatti, A. Miluzio, A. Scagliola, S. Biffo, Translating the Game: Ribosomes as Active Players. *Frontiers in Genetics* **9**, (2018).
86. E. W. Mills, R. Green, Ribosomopathies: There's strength in numbers. *Science* **358**, eaan2755 (2017).
87. K. M. Goudarzi, M. S. Lindstrom, Role of ribosomal protein mutations in tumor development (Review). *Int J Oncol* **48**, 1313-1324 (2016).
88. A. Vlachos, P. S. Rosenberg, E. Atsidaftos, B. P. Alter, J. M. Lipton, Incidence of neoplasia in Diamond Blackfan anemia: a report from the Diamond Blackfan Anemia Registry. *Blood* **119**, 3815-3819 (2012).
89. E. Emmott, M. Jovanovic, N. Slavov, Ribosome Stoichiometry: From Form to Function. *Trends Biochem Sci* **44**, 95-109 (2019).
90. A. Parsyan *et al.*, mRNA helicases: the tacticians of translational control. *Nat Rev Mol Cell Biol* **12**, 235-245 (2011).
91. M. Bhat *et al.*, Targeting the translation machinery in cancer. *Nat Rev Drug Discov* **14**, 261-278 (2015).

92. G. G. D'Souza, M. A. Wagle, V. Saxena, A. Shah, Approaches for targeting mitochondria in cancer therapy. *Biochim Biophys Acta* **1807**, 689-696 (2011).
93. R. J. Youle, M. Karbowski, Mitochondrial fission in apoptosis. *Nature Reviews Molecular Cell Biology* **6**, 657-663 (2005).
94. P. A. Parone, J.-C. Martinou, Mitochondrial fission and apoptosis: An ongoing trial. *Biochimica et Biophysica Acta (BBA) - Molecular Cell Research* **1763**, 522-530 (2006).
95. L. Pan, L. Zhou, W. Yin, J. Bai, R. Liu, miR-125a induces apoptosis, metabolism disorder and migrationimpairment in pancreatic cancer cells by targeting Mfn2-related mitochondrial fission. *Int J Oncol* **53**, 124-136 (2018).
96. H. Chen, A. Chomyn, D. C. Chan, Disruption of fusion results in mitochondrial heterogeneity and dysfunction. *J Biol Chem* **280**, 26185-26192 (2005).
97. L. Griparic, N. N. van der Wel, I. J. Orozco, P. J. Peters, A. M. van der Bliek, Loss of the intermembrane space protein Mgm1/OPA1 induces swelling and localized constrictions along the lengths of mitochondria. *J Biol Chem* **279**, 18792-18798 (2004).
98. P. Mishra, V. Carelli, G. Manfredi, D. C. Chan, Proteolytic cleavage of Opa1 stimulates mitochondrial inner membrane fusion and couples fusion to oxidative phosphorylation. *Cell Metab* **19**, 630-641 (2014).
99. S. Giordano, J. Lee, V. M. Darley-Usmar, J. Zhang, Distinct effects of rotenone, 1-methyl-4-phenylpyridinium and 6-hydroxydopamine on cellular bioenergetics and cell death. *PLoS One* **7**, e44610 (2012).
100. R. Anand *et al.*, The i-AAA protease YME1L and OMA1 cleave OPA1 to balance mitochondrial fusion and fission. *J Cell Biol* **204**, 919-929 (2014).
101. M. J. Baker *et al.*, Stress-induced OMA1 activation and autocatalytic turnover regulate OPA1-dependent mitochondrial dynamics. *EMBO J* **33**, 578-593 (2014).
102. J. Lopez, S. W. Tait, Mitochondrial apoptosis: killing cancer using the enemy within. *Br J Cancer* **112**, 957-962 (2015).
103. C. Frezza *et al.*, OPA1 controls apoptotic cristae remodeling independently from mitochondrial fusion. *Cell* **126**, 177-189 (2006).
104. J. B. Baell, D. C. Huang, Prospects for targeting the Bcl-2 family of proteins to develop novel cytotoxic drugs. *Biochem Pharmacol* **64**, 851-863 (2002).

105. T. Morisaki, M. Katano, Mitochondria-Targeting Therapeutic Strategies for Overcoming Chemoresistance and Progression of Cancer. *Current Medicinal Chemistry* **10**, 2517-2521 (2003).

8. Appendix

8.1 Supplementary Figure

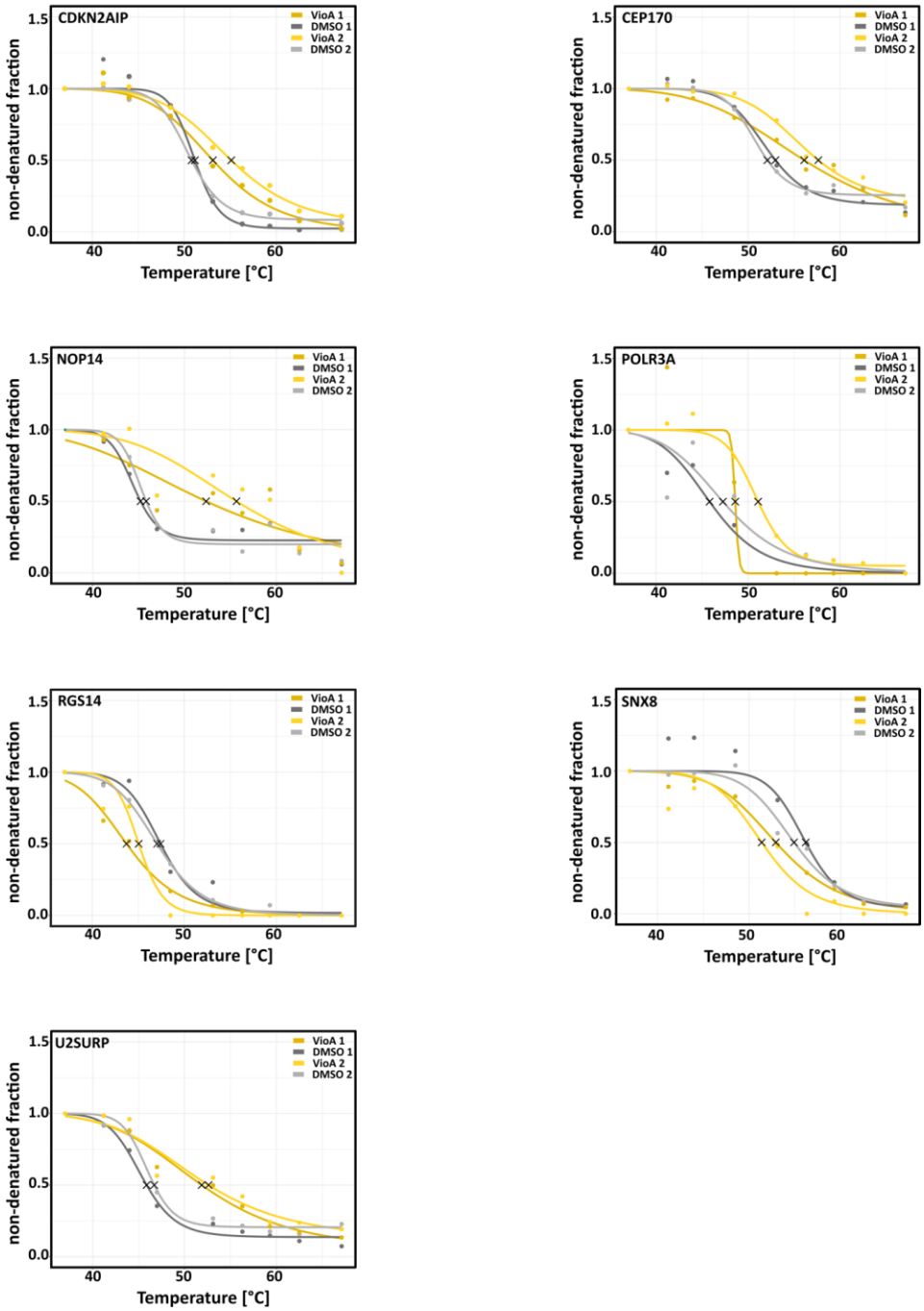

Fig. S1 Thermal response curves of potential hits identified in thermal proteome profiling experiment. Thermal response curves for proteins passing all filtering thresholds when treating cells with 1 µM VioA (orange) compared to DMSO controls (grey). Melting points and melting curve fitting was carried out and data visualized using the TPP R package (*60*) and GraphPad Prism 8. CEP170 met all significance criteria in one replicate but was just outside the threshold for significance in the other. Experiment was performed by Volker Kirsch in the laboratory of Prof. Dr. Stephan Sieber (TU Munich, Germany).

8.2 Supplementary Tables

Table S1: Calculated *p*-value, slope and curve fit for protein targets of vioprolide A in Jurkat cells as elucidated by *in situ* thermal proteome profiling. Proteins listed met all filter criteria.(*60*) CEP170 met all significance criteria in one replicate but was just outside the threshold for significance in the other. Data evaluation was performed by Volker Kirsch (laboratory of Prof. Dr. Stephan Sieber, TU Munich, Germany).

T_m shift repl 1/2 [°C]	p-value adj. repl 1/2	R^2 curve fit (VioA1/DMSO1/ VioA2/DMSO2)	Min. slope VioA vs DMSO repl. 1/2	Gene	Protein
6.61/8.85	6.5E-07/9.32E-14	0.81/0.94/0.84/0.95	-0.10/-0.10	NOP14	Nucleolar protein 14
5.39/4.89	5.18E-03/2.91E-02	0.99/0.99/0.95/0.99	-0.08/--0.09	U2SURP	U2 snRNP-associated SURP motif-containing protein
3.13/5.55	3.13E-01/4.00E-05	0.98/0.99/0.99/0.99	-0.09/-0.11	CEP170	Centrosomal protein of 170 kDa
1.96/4.31	4.93E-02/3.48E-03	0.99/0.98/0.99/1.00	-0.18/-0.13	CDKN2AIP	CDKN2A-interacting protein
2.79/3.82	6.63E-03/1.2E-03	0.82/0.96/0.99/0.84	-1.29/-0.14	POLR3A	DNA-directed RNA polymerase subunit
-3.70/-2.00	3.32E-02/1.55E-01	0.99/0.98/0.96/1.00	-0.13/-0.19	RGS14	Regulator of G-protein signaling 14
-3.27/-3.53	8.03E-02/8.61E-02	0.99/0.93/0.92/0.98	-0.12/-0.09	SNX8	Sorting nexin-8

Table S2: Proteins enriched in MS-based co-IP experiments. Listed proteins were significantly enriched in NOP14 antibody treated Jurkat cells in comparison to isotype control treated cells. Experiment was performed by Volker Kirsch in the laboratory of Prof. Dr. Stephan Sieber (TU Munich, Germany).

log_2 enrichment	$-log_{10}$ (*t*-test *p*-value)	Gene	Protein
8.99	7.06	TFG	Protein TFG; Tyrosine-protein kinase receptor
8.06	5.53	SNAP29	Synaptosomal-associated protein 29
7.12	6.76	NANS	Sialic acid synthase
6.75	5.46	NOP14	Nucleolar protein 14
6.30	5.18	NOC4L	Nucleolar complex protein 4 homolog
5.13	5.32	DECR	2,4-dienoyl-CoA reductase, mitochondrial
4.41	4.82	MTCL1	Microtubule cross-linking factor 1
4.21	3.88	DTWD2	DTW domain-containing protein 2
4.16	4.05	NACC1	Nucleus accumbens-associated protein 1
3.70	4.86	IPO5	Importin-5
3.45	3.82	SEPT6	Septin 6
3.44	5.18	SEPT7	Septin 7
3.32	5.76	TPR	Nucleoprotein TPR

3.27	3.51	CIZ1	Cip1-interacting zinc finger protein
3.27	3.11	GFPT1	Glutamine-fructose-6-phosphate aminotransferase 1
3.12	4.68	PRKCA	Protein kinase C alpha type
3.10	4.72	SEPT2	Septin 2
3.06	1.57	SUB1	Activated RNA polymerase II transcriptional coactivator p15
2.98	3.53	HNRNPA2B1;HNRPA2B1	Heterogeneous nuclear ribonucleoproteins A2/B1
2.75	4.00	NAPA	Alpha-soluble NSF attachment protein
2.69	3.27	IST1	IST1 homolog
2.61	2.03	PPP2R1A	Serine/threonine-protein phosphatase 2A 65 kDa regulatory subunit A alpha isoform
2.48	4.89	EMG1	Ribosomal RNA small subunit methyltransferase NEP1
2.28	3.39	HSD17B10	3-hydroxyacyl-CoA dehydrogenase type-2
2.24	1.95	PPA1	Inorganic pyrophosphatase
2.20	4.17	ATAD3A/B	ATPase family AAA domain-containing protein 3A/B
2.11	2.68	EEF1D	Elongation factor 1-delta
2.01	1.66	PCBP2	Poly(rC)-binding protein 2

8.3 Abbreviations

5-FU 5-Fluorouracil
ActD ..... Actinomycin D
ALL ..... Acute lymphoblastic leukemia
AML ..... Acute myeloid leukemia
ANOVA ..... Analysis of variance
AntA ..... Antimycin A
ATP ..... Adenosine triphosphate
BAK ..... Bcl-2 homologous antagonist
BAX ..... Bcl-2 associated X protein
Bcl-2 ..... B-cell lymphoma 2
Bcl-xL ..... B-cell lymphoma extra large
BSA ..... Bovine serum albumin
CASP3 ..... Caspase-3
CASP8 ..... Caspase-8
CIM ..... Cell invasion/ migration
CTB ..... Cell titer blue
Ctrl ..... Control
DMEM ..... Dulbecco's modified Eagle's Medium
DMSO ..... Dimethylsulfoxide
DNA ..... Desoxyribonucleic acid
Doxo ..... Doxorubicin
DRP1 ..... Dynamin-related protein 1
DSSO ..... Disuccinimidyl sulfoxide
DTT ..... Dithiothreitol
EC_{50} ..... Half-maximal effective concentration
ECL ..... Enhanced chemiluminescence
EDTA ..... Ethylenediaminetetraacetic acid
Em ..... Emission
EMG1 ..... Ribosomal RNA small subunit methyltransferase Nep1
ERK ..... Extracellular-signal regulated kinase
Ex ..... Excitation
FACS ..... Fluorescence activated cell sorting
FCCP ..... Carbonyl cyanide-4-(trifluoromethoxy)phenylhydrazone
FCS ..... Fetal calf serum
FDA ..... US Food and Drug Administration
FSC ..... Forward scatter
GTP ..... Guanosine triphosphate
HILIC ..... Hydrophilic interaction liquid chromatography
HRP ..... Horseradish peroxidase
IC_{50} ..... Half-maximal inhibitory concentration
IMDM ..... Iscove's Modified Dulbecco's Medium
IP ..... Immunoprecipitation
JC-1 ..... Tetraethylbenzimidazolylcarbocyanine iodide
KRAS ..... Kirsten rat sarcoma virus
LagA ..... Lagunamide A
LC-MS ..... Liquid chromatography–mass spectrometry

mAb ..... Monoclonal antibody
Mcl-1 ..... Induced myeloid leukemia cell differentiation protein
MeOH ..... Methanol
MOMP ..... Mitochondrial outer membrane permeabilization
MYC ..... Avian myelocytomatosis viral oncogene homolog
NOC4L ..... Nucleolar complex associated 4 homolog
NOP14 ..... Nucleolar protein 14
NOR ..... Nucleolar organizing region
NP-40 ..... Octoxinol 9
NSG mice ..... NOD scid gamma mice
OCR ..... Oxygen consumption rate
OMA1 ..... Metalloendopeptidase OMA1, mitochondrial
OMM ..... Outer mitochondrial membrane
OPA1 ..... Optic atrophy 1
OXPHOS ..... Oxidative phosphorylation
P/S ..... Penicillin/ streptomycin
PAA ..... Polyacrylamide
PAGE ..... Polyacrylamide gel electrophoresis
PARP ..... Poly ADP ribose polymerase
PBMC ..... Peripheral blood mononuclear cell
PBS ..... Phosphate bufferd saline
PDX ..... Patient derived xenograft
PE ..... Phycoerythrin
PFA ..... Paraformaldehyde
PGC1α ..... Peroxisome proliferator-activated receptor-γ coactivator
Phb1 ..... Prohibitin 1
PI ..... Propidium iodide
Pol I ..... RNA polymerase I
Pol II ..... RNA polymerase II
Pol III ..... RNA polymerase III
PVDF ..... Polyvinylidene difluoride
rDNA ..... ribosomal DNA
RNA ..... Ribonucleic acid
ROS ..... Reactive oxygen species
RPMI ..... Roswell Park Memorial Institute
rRNA ..... Ribosomal RNA
RT ..... Room temperature
SDS ..... Sodium dodecyl sulafate
SEM ..... Standard error of the mean
siRNA ..... Small interfering RNA
SPG7 ..... Spastic paraplegia 7
SSC ..... Side scatter
TBS-T ..... Tris-buffered saline + Tween
TCE ..... Trichloroethanol
TEM ..... Transmission electron microscopy
TPP ..... Thermal proteome profiling
U2SURP ..... U2 snRNP-associated SURP motif-containing protein
ULA ..... Ulta low attachment

VioA ..... Vioprolide A
VioB ..... Vioprolide B
VioC ..... Vioprolide C
VioD ..... Vioprolide D
ΔΨm ..... Mitochondrial membrane potential

8.4 List of publications and conference contributions

8.4.1 Article

The cytotoxic natural product vioprolide A targets nucleolar protein 14 essential for ribosome biogenesis

Volker C. Kirsch*, Christina Orgler*, Simone Braig, Irmela Jeremias, David Auerbach, Rolf Müller, Angelika M. Vollmar* and Stephan A. Sieber*

Submitted

*authors contributed equally to this manuscript

8.4.2 Presentation

Functional characterization and transcriptome analysis of Vioprolide A in leukemia cells

Christina Besl, Fabian Bischoff , Iris Bischoff, Simone Braig, Rolf Müller, Robert Fürst, Angelika M. Vollmar

7th FOR 1406 Meeting

July 2016, Munich, Germany

8.4.3 Poster

Antitumoral potential of the myxobacterial peptolide Vioprolide A

Christina Besl, Fabian Koczian, Robert Fürst, Rolf Müller, Angelika M. Vollmar and Simone Braig

8th Mildred Scheel Cancer Conference (Deutsche Krebshilfe)

May 2017, Bonn, Germany

8.5 Acknowledgements

Mein erster und größter Dank geht an meine Doktormutter, Frau Prof. Vollmar. Vielen Dank, dass Sie mir die Möglichkeit gegeben haben in Ihrem Arbeitskreis zu promovieren und dabei drei interessante Projekte zu bearbeiten. Vielen Dank für Ihre Betreuung und die vielen wertvollen Ratschläge und Diskussionen. Ihre große Begeisterung für die Wissenschaft, sowie Ihre herzliche und motivierende Art, haben mich immer sehr beeindruckt.

Ein besonderer Dank gilt meinen weiteren Prüfern. Vielen Dank, Frau Prof. Merkel, dass Sie meine Arbeit als zweite Gutachterin beurteilt haben. Ich danke außerdem Frau Prof. Pachmayr, Herrn Prof. Wagner, Herrn Prof. Zahler und Herrn Dr. Thorn-Seshold. Herzlichen Dank, dass Sie sich Zeit genommen haben meine Arbeit zu bewerten.

Ganz herzlich möchte ich mich auch bei Simone bedanken. Liebe Simone, vielen Dank, für deine hervorragende Betreuung und die vielen konstruktiven Diskussionen während und außerhalb unserer Teammeetings. Danke, dass deine Tür jederzeit offen stand und du auch in schwierigen Phasen immer Optimismus verbreitet hast.

Außerdem möchte ich mich bei meinen zahlreichen Kooperationspartnern bedanken. Allen voran bei Volker Kirsch und Herrn Prof. Sieber für die großartige Zusammenarbeit während unseres Vioprolid-Projekts. Lieber Volker, ich fand es toll, wie wir die verschiedenen Herausforderungen dieses Projekts zusammen gemeistert haben und es freut mich sehr, dass wir unser gemeinsames Paper fertigstellen konnten. Zudem möchte ich mich bei Dr. Binje Vick und Frau Prof. Jeremias für die Bereitstellung der PDX Zellen bedanken. Ein weiterer Dank geht an Dr. Sabine Schmitt und Herrn Prof. Zischka für die tolle Zeit, die ich im Zischka-Labor im Rahmen des Lagunamid-Projekts verbringen durfte. Ihr habt zu wertvollen Ergebnissen dieser Arbeit beigetragen.

Ein großer Dank geht an den gesamten AK Vollmar. Ich hätte mir keine besseren Kollegen wünschen können und ich bin jeden Tag gerne in die Arbeit gekommen. Vielen Dank für die zahlreichen lustigen Mittags- und Kaffeepausen während der Arbeit, sowie die Beer-Tastings, Grillfeiern und Wiesn-Besuche nach der Arbeit. Die Zeit mit euch war einfach großartig. Ein ganz besonderer Dank geht dabei an Martin und meine beiden Team-Kolleginnen Caro und Olga. Vielen Dank, dass wir uns sowohl auf fachlicher, als auch privater Ebene immer so gut austauschen und gegenseitig helfen konnten. Danke auch an Carina für die schöne Zeit in unserer Box im Labor. Bei Kerstin möchte ich mich außerdem für die tolle und geduldige Einarbeitung am Anfang bedanken. Vielen Dank auch an Jana, Julia und Frau Schnegg für die Unterstützung bei meinen Projekten. Ein

großer Dank geht an meine Masterstudentin Michaela Koburg und meine Bachelorstudenten Jonathan Kusch und Ida Folda. Es hat mir großen Spaß gemacht mit euch zusammenzuarbeiten.

Zu guter Letzt möchte ich mich noch bei meinen Freunden und meiner Familie bedanken.

Ein großes Dankeschön möchte ich an Sarah und Frizi richten. Wir haben zusammen das Pharmaziestudium gemeistert und es war, vor allem dank euch, eine unvergessliche Zeit für mich.

Lieber Flo, vielen Dank für deine Unterstützung, deine unendliche Geduld und für deine tolle Fähigkeit mich im richtigen Moment aufzumuntern. Ein besonders großer Dank geht an Kathi- du bist nicht nur meine kleine Schwester, sondern auch meine beste Freundin. Ich kann mich immer auf dich verlassen. Diese Sicherheit war gerade in den letzten Jahren, in denen es für uns beide viele Höhen und Tiefen zu meistern gab, wahnsinnig wertvoll.

Mein wichtigster Dank gilt schließlich meinen Eltern, Gerlinde und Karl. Vielen Dank für eure grenzenlose Unterstützung während meines gesamten Lebensweges und dass ihr mir immer die Freiheit gegeben habt meinen eigenen Weg zu gehen. Danke, dass ihr immer hinter mir steht und an mich glaubt. Euch ist diese Arbeit gewidmet.